Manipulation of magnetic and chemical properties of cobalt nanoparticles studied by means of x-ray photo-emission electron microscopy

Inauguraldissertation

zur

Erlangung der Würde eines Doktors der Philosophie

vorgelegt der

Philosophisch-Naturwissenschaftlichen Fakultät

der Universität Basel

von

Tatiana Savchenko

aus Russland

2020

Genehmigt von der Philosophisch-Naturwissenschaftlichen Fakultät

auf Antrag von

Fakultätsverantwortlicher: Prof. Dr. Frithjof Nolting

Korreferent: Prof. Dr. Andrei Kirilyuk

Basel, 19.11.2019

Dekan: Prof. Dr. Martin Spiess

To my beloved husband Ilya who knows my text by heart and supported me every single day of my PhD, and to my family who stayed 2500 km away and always believed that I would achieve my goals.

Abstract

Investigation of structure and magnetic properties of nanoparticles is important for application in catalysis, data storage, chemical sensing, energy conversion and drug delivery. Laser manipulation of magnetization of the nanoparticles can be promising for next generation data recording technology.

Large scattering of magnetic properties of cobalt nanoparticles makes it difficult to apply simple scaling laws. Most probably this is due to the measurement techniques averaging over a large number of the nanoparticles with different crystal structures, internal defects and morphology. In our approach we use an outstanding combination of characterization techniques that allow us to directly correlate magnetic properties in individual cobalt nanoparticles with their crystal structure and morphology. We use x-ray photo-emission electron microscopy (XPEEM) for magnetic characterization of the nanoparticles and high-angle annular dark field scanning transmission electron microscopy (HAADF-STEM) for atomic resolution structural characterization. Our results show that magnetic blocking in cobalt nanoparticles occurs independently of the particles size and the orientation of the magnetization does not correlate with crystallographic axes. Our structural investigations suggest also that many of the particles have defects which modify the magnetic anisotropy. We have developed atomistic models for STEM simulations and compare them to the STEM data to prove the nature of the defects and their positions in the nanoparticle. Still ongoing is the development of a theoretical approach for calculating the magnetic properties of nanoparticles with defects.

We combine XPEEM and HAADF-STEM approach to correlate magnetic properties and chemical composition of cobalt nanoparticles with the actual morphology upon *in situ* oxidation. Understanding the role of the surface is important for revealing the origin of magnetically blocked states of cobalt nanoparticles smaller than 15 nm, oxidation kinetics and the products of the reaction is important for catalysis. Most of the studies rely on x-ray absorption spectroscopy and modelling of the spectra. However, early oxidation kinetics of cobalt nanoparticle remained unclear. We show that reduction of magnetic volume upon oxidation lowers the magnetic energy barrier. Our STEM data show a surprisingly complicated oxidation kinetics, which is not properly reflected in simulated x-ray absorption spectra. The early stage of oxidation leads to formation of inhomogeneous shell on the nanoparticles, dosing more oxygen improves the shell morphology, even further oxidation leads to thickening of the shell.

Purely optical magnetization orientation reversal with femtosecond laser pulses (all-

optical switching) was shown in thin films and granular media of various materials. So far no such results were presented for single nanoparticles with diameter smaller than 15 nm. We combine XPEEM with femtosecond laser pulse exposure to investigate the effect of ultrashort laser pulses on cobalt nanoparticles. No deterministic switching is found independently on laser fluence and polarization. Also, no thermal switching of nanoparticles magnetization is observed. Instead, we find that laser triggers a chemical reaction with the substrate which alters magnetic energy barrier in the nanoparticles. Our results suggest that for a successful laser-induced switching of the magnetic nanoparticles, nanoparticles with lower T_C either defined by size effects or by choosing different materials are required.

Summarizing, our investigations show that structural defects are important for magnetic properties of cobalt nanoparticles, especially for stability of their magnetization and orientation of the magnetic moment. We found complex oxidation kinetics, which is important for better understanding of catalysis and magnetic behavior. Femtosecond laser excitation of magnetic nanoparticles seems promising but for materials with lower T_C. Higher resolution x-ray imaging is needed to reveal spin configuration of the individual nanoparticles time and better investigate the chemical composition and magnetic properties of oxidized cobalt nanoparticles.

Acknowledgements

"If I have seen further it is by standing
on the shoulders of Giants."
Isaac Newton.

I would first like to thank my thesis advisor Prof. Dr. Frithjof Nolting at Basel Universität. He has provided me with the topic I dreamed of, let me taking part in several outstanding projects, worked to improve my writing skills and helped to go in the right direction, follow the deadlines and finish in time.

I would like to also acknowledge my supervisor at PSI Dr. Armin Kleibert. Dr. Kleibert spent many hours teaching me the experimental techniques at the Swiss Light Source, helped with data analysis and understanding of magnetic anisotropy, improved my presentation skills, helped me to manage my projects and took me on board of many great projects at SIM beamline.

I would like to thank Dr. Carlos A. F. Vaz for instantaneous help in the tough moments when no one else was around. Thanks to Dr. Simone Finizio for explaining me that scientific English is a different language, that really helped. Thanks to David Bracher that he was always around when I was performing the experiments at SIM beamline, for taking over half of the night shifts and for entertaining the students. Thanks to Dr. Jaianth Vijayakumar for sharing the pain of data analysis on single nanoparticles and beam times. Thanks to Pascal Schifferle for technical support at SIM beamline.

Special thanks to Dr. Armand Béché, Dr. Elisabeth Mueller, Anja Weber and Dr. Peter M. Derlet. Without their input and valuable comments part of this work would not have been possible. Thanks to ETH ScopeM team for teaching me transmission electron microscopy techniques.

Thanks to the collaborators I had an opportunity to work with: Zhaochu Luo, Andrea Navarro-Quezada, Dr. Lorenzo Baldrati, Mariia Filianina, Kshiti Mishra, Dr. Benedikt Roessner, Prof. Dr. Jan Luning, Dr. Flavio Capotondi, Dr. Emmanuelle Jal, Dr. Sonia Castellanos Ortega, Dr. Ivan Bespalov and all others.

Thanks to all the members of Microscopy and Magnetism group for showing an example of friendly and healthy work atmosphere: Dr. Urs Staub, Dr. Cinthia Piamonteze, Dr. Jan Dreiser, Stefan Zeugin, Dr. Sergii Parchenko, Dr. José Linares Mardegan, Dr. Mihal Studniarek, Dr. Martin Schoen, Dr. Aram Kostanyan, Dr. Ludovic Howald, Martin Decker, Dr. Michele Buzzi, Dr. Sridhar Reddy Avula Venkata, Dr. Niéli Daffé, Marta

Mirolo, Silvie Voegel and all others. Special thanks to Pelin Ueresin, Vlad Romankov, Anna Zakharova, and Nazareth Ortiz Hernandez for letting me find new friends in the work process, everyday motivation and not letting me giving up. Thanks to our wonderful secretaries Martina Fueglister and Charlotte Heer for making paper work at PSI simple and fast.

Thanks to other friends from PSI who made these four years unforgettable: Dr. Nicolas Bachellier and Dr. Katharina Witte for motivating me to put higher goals in sports and kind support during my stay at PSI. Thanks to Alex Turrini for nice and motivating discussions about physics and life, thanks to Dr. Ben Watts, Dr. Joerg Raabe, Dr. Manuel Langer, Dr. Valerio Scagnoli, Dr. Olga Safonova, Dr. Matthias Muntwiler, Patrick Ascher and all members of PhD and PostDoc association, Basketball team PSI, climbing team and PSI Human Resources for support of my social activities and PSI Education Center for providing useful courses during my studies.

Finally, I must express my very profound gratitude to my parents, family and to my spouse Ilya for providing me with unfailing support and continuous encouragement throughout my years of study and through the process of researching and writing this thesis. This accomplishment would not have been possible without them. Thank you.

Tatiana Savchenko

Contents

Chapter 1

Introduction

The size dependence of magnetic properties in nanoparticles have attracted a great interest for applications as well as for theory. For instance, applications such as biomedicine, medical imaging, drug delivery, energy conversion, chemical sensors, magnetic data storage and spintronics are in demand for nanometer sized nanoparticles with tunable properties [1]. In this regime single magnetic domain states and superparamagnetism [2] (thermally induced fluctuations of the magnetization) can be observed. Usually it is believed that size and magnetic properties of nanoparticles have a clear relation given by scaling laws. The size is expected to be the variable for tuning magnetic structure, magnetic anisotropy, coercivity and blocking temperatures [3]. However, for instance for magnetic anisotropy (which governs magnetization relaxation process and the magnetization orientation) theory and experiments diverge in orders of magnitude even for canonical cases of *3d* transition metal nanoparticles with narrow size distribution [4, 5, 6, 7, 8, 9].

One possible reason of this controversy might be the averaging of a large ensemble of nanoparticles during measurements which may mask the structural defects, different crystal structures and morphology of individual particles. In spectroscopic methods like superconductive quantum interference device magnetometry, Mössbauer spectroscopy, Raman spectroscopy, magneto-optic Kerr effect magnetometry and x-ray magnetic circular dichroism spectroscopy, the properties of a huge number of nanoparticles are averaged during the measurement which therefore introduces severe uncertainties. Besides, complex interactions between neighboring nanoparticles can affect the macroscopic magnetic properties of an ensemble of nanoparticles [1, 10]. In addition, synthesis methods and thermal history of the nanoparticles can play a role for the magnetic properties. Complex interactions between nanoparticles in ensembles and the scattering of the properties of individual nanoparticles makes it difficult to disentangle size-dependent properties from effects caused by the defects.

Since even the classical example of *3d* transition metal nanoparticles is not yet well understood, it is important to investigate simple model systems, consisting of pure metallic and non-interacting nanoparticles. It was recently demonstrated experimentally that apart from the expected superparamagnetic state, iron and cobalt nanoparticles smaller than 25 nm can also exist in a magnetically blocked state associated with a strongly enhanced magnetic anisotropy [11]. In addition, iron nanoparticles possess magnetic metastastability, which results in spontaneous transitions or transitions promoted by heating from magnetically blocked to a superparamagnetic state [12, 11]. Such magnetic transition may point to an underlying structural transition from an energetically excited state to a lower-energy state [11]. Unlike iron, moderate heating of cobalt nanoparticles promotes states with higher magnetic energy barriers [11]. It has been shown in the literature that structural defects cannot only modify the magnetic anisotropy but also the magnetic spin structure [13]. However, a direct correlation of magnetism and structural properties was not achieved in former works.

In fact, a direct correlation of magnetism and structure is challenging and rarely can deliver a single nanoparticle information. In case of MFM, the spatial resolution is limited at around hundreds of nanometers. Nano-SQUID is capable to investigate the magnetism of a single nanoparticle but the nanoparticles growth process creates a magnetically dead layer in the interface between the nanoparticle and the substrate which makes the precise determination of the real magnetic volume by means of SEM impossible [14, 15]. Lorentz STEM with magnetic sensitivity and spatial resolution of 5 nm [16, 17], and magnetic holography with sub-10 nm resolution [18, 19, 20] and the promising tools for magnetic high resolution imaging, however are capable to work with nanoparticles with mean diameters close to 100 nm. But not only magnetic characterization of individual nanoparticles is challenging. Structural atomic level information of *3d* transition metals is difficult to derive because of their small lattice constants compared to Au and Pt. All these facts together with the difficulty to allocate complementary data of the very same nanoparticle on the sample, makes correlative magneto-structural studies complicated. In this work, we combine x-ray photo-emission electron microscopy (XPEEM), with high-angle annular dark field scanning transmission electron microscopy (HAADF-STEM) to correlate magnetism and structure of the very same nanoparticles. We use gold marker structures to navigate on the sample and unambiguously identify the very same nanoparticles in every experiment.

Surface atoms may play a crucial role in the magnetism of nanoparticles. For example, it has been reported that different capping layers can result in different magnetic

anisotropy energies [21, 22]. A recent work on surface oxidation of iron nanoparticles has shown that the enhanced magnetic anisotropy does not arise from a surface anisotropy contribution [23]. However, that work lacked structural data for individual nanoparticles in order to correlate structure with magnetic properties of the respective nanoparticles. The early stages of oxidation of metallic nanoparticles is frequently associated with the formation of a core/shell structures. Moreover, atomic diffusion is possible within and between the core and the shell and can significantly impact the overall stability, reactivity, stoichiometry and also the magnetic properties of the particles [24, 25]. Previous studies of the evolution of Co-oxide nanoparticles report on different compositions of the shell such as CoO, Co_3O_4 and wurtzite-CoO [26, 27]. The strength of our approach here is that by combining XPEEM with STEM, we can directly address chemical, magnetic properties and morphology of individual nanoparticles, which was not possible before.

Manipulation of magnetic properties by means of external excitation is important for applications in spintronics. Fast deterministic switching of the magnetization is important for data storage technology. Ultrafast nonthermal photo-magnetic effect has been demonstrated for example on ferromagnetic garnets and orthoferrites [28, 29, 30]. The discovery of all-optical switching (AOS) using femtosecond laser pulses has received particular attention, since AOS may facilitate ultrafast data writing processes in magnetic matter without using external magnetic field [31]. AOS has been initially demonstrated in rare-earth transition-metals alloys such as FeGdCo, but was later found also in rare-earth free systems such as Pt/Co/Pt trilayers as well as in granular recording media composed of FePt nanoparticles upon excitation with multiple laser pulses [32, 33]. So far, most investigations have been carried out on thin films or micron-sized structures, but the effect of femtosecond laser pulses on truly nano-sized magnetic systems has not been addressed. Here, we use XPEEM together with single laser pulse excitation to determine the magnetic and chemical properties of individual cobalt nanoparticles before and after a laser pulse excitation.

This Thesis consists of **7** Chapters. Chapters **1-3** discuss fundamental aspects of cobalt nanoparticles, magnetism of cobalt nanoparticles, samples and techniques used in this work. Chapters **4-7** describe experimental results and outlook.

In **Chapter 2**, we discuss fundamental aspects of nanoparticles magnetism, magnetic stability, magnetic anisotropy and aspects reported in the literature regarding structure, magnetic properties of cobalt nanoparticles, and their interaction with femtosecond laser pulses.

In **Chapter 3**, we explain sample preparation, XPEEM and laser experiment setup,

x-ray methods involved in the experiments, single nanoparticle identification, individual nanoparticle data analysis and the HAADF-STEM experiments.

Chapter 4 describes how we correlate magnetic properties with microstructure of cobalt nanoparticles. We employ XPEEM and HAADF-STEM to characterize magnetism and atomic structure of the same nanoparticles. As the result, we are able to reconstruct the orientation of the magnetic moments of individual magnetically blocked nanoparticles in comparison to the crystallographic axes. Structural defects were discovered in many nanoparticles. To clarify the nature of these defects, a series of STEM image simulations were performed and compared to the experimental data. These data showed that stacking faults might explain anomalous magnetic properties of the nanoparticles. The models can be used for future simulations of the magnetism of nanoparticles, which includes the role of structural defects.

In **Chapter 5** we combine XPEEM with HAADF-STEM to reveal surprisingly complex growth kinetics of the oxide shell, formed upon *in situ* oxidation. We find that magnetic contrast is present in individual nanoparticles from the unoxidized state up to an oxide layer of 4 nm in thickness, where only CoO is observed in the oxide shell. With further oxygen dosage, the x-ray magnetic circular dichroism (XMCD) contrast of a large number of the particles disappeares; at this stage we start to observe the formation of Co_3O_4 on CoO shell. The disappearance of magnetic contrast is attributed to the formation of a superparamagnetic core. From HAAD-STEM, we find the presence of voids at the early stage of oxidation resulting in a discontinuity in the oxide shell which could explain the misfit of simulated x-ray absorption spectroscopy (XAS) spectra with experimental data. At the later stage of oxidation the oxide shell becomes more compact which suggests a complicated oxidation kinetics.

In **Chapter 6** we focus on the effect of single ultrashort infrared laser pulses onto individual cobalt nanoparticles deposited on silicon substrates. Particularly, we are interested in the nanoparticles with stable magnetization since they can not be simply switched by thermal fluctuations and require additional energy from the laser to reverse the magnetization direction. In this work, we investigate the effect of ultrafast laser pulse on chemical and magnetic properties of cobalt nanoparticles. The response of the nanoparticles to the laser pulses is studied by combining XPEEM with XMCD and XAS. This approach allows us to determine magnetic and chemical state of individual nanoparticles before and after laser pulse excitation. We find that laser pulses with a fluence of up to 21 mJ/cm^2 do not result in deterministic switching of the magnetization of the nanoparticles, irrespective of the laser polarization. Increasing the intensity further

leads eventually to a loss of magnetic contrast, which is accompanied by an irreversible chemical reaction of the nanoparticles with the substrate.

Finally, in **Chapter 7** we give the summary of the Thesis and present an outlook for future investigations.

Chapter 2

Magnetic properties, structure and their manipulation in Co particles

In magnetic materials, magnetic properties are highly dependent on the internal atomic arrangement, the surface atoms and the crystal structure [6, 4, 7]. Finite size of the nanoparticles can give rise to strong surface anisotropy, superparamagnetism and single domain states. Magnetic anisotropy values of transition metal nanoparticles scatter over a broad range of values even for samples with narrow size distribution [5]. For example, it was recently experimentally demonstrated for cobalt nanoparticles, that apart from expected superparamagnetic state, they can also exist in magnetically blocked states associated with a strongly enhanced magnetic anisotropy, which has been attributed to the presence of lattice defects in the core of the nanoparticles [12, 34, 11]. Therefore, a closer look to individual properties of isolated particles is required. Since every individual nanoparticle could have different magnetic properties, conventional experiments average them out over a large number of particles, potentially hiding the relevant parameters. Thus, applying simple size-dependent scaling laws for magnetic properties of the nanoparticles remains complicated [35, 36, 37]. In this work we will try to shed light on single nanoparticle's magnetism. We will start from correlation of crystalline structure, size, internal defects on the magnetically blocked states and magnetization direction of the nanoparticles. Then, we will continue with the role of surface for magnetization stabilization which we address through controlled oxidation of nanoparticles. Lastly, effect of magnetic stability and interactions with single ultra-fast laser pulses is addressed. This will be the basis for the following Chapters.

2.1 Cobalt nanoparticles

Bulk cobalt is a ferromagnetic material [2] with average magnetic moment of 1.72 μ_B per atom. Cobalt nanoparticles can exhibit strong deviations of magnetic properties compared to the bulk values since these properties can be affected by several factors such as size, crystalline structure, magnetic anisotropy, ligands (residuals from synthesis and oxidation due to high reactivity of cobalt), and interactions with neighboring nanoparticles or with the substrate [5, 11, 38, 39, 40]. Cobalt nanoparticles have been reported to exist in three crystal structures: hcp, fcc and ε-cobalt [41, 42, 43, 44]. The structure itself depends on the synthesis conditions such as temperature during synthesis or subsequent annealing. At room temperature bulk cobalt only exists in the hcp crystal lattice, whereas cobalt nanoparticles can be found in fcc structure as well as hcp or multiple-twinned fcc [41]. Each crystal structure has different lattice constants, cohesion energy and anisotropy.

2.1.1 Structural lattice defects

Defects play an important role in material properties, since they induce strain and change magnetic properties [45, 46, 47]. There is a number of crystal defects that metals could have, such as point defects, linear (screw and edge dislocations), planar (twins, stacking faults), surface or volume defects [48]. There are two particular defects that will be relevant in this Thesis: twin boundaries and stacking faults. Twinning is the formation of original crystal stack with a new orientation in some region of the crystal. In a simple case twin boundary is a mirror symmetry plane with respect to the initial crystal [cf. Fig. 2.1"A"]. Stacking faults are another type of defects where planar mismatch causes interruption of regular stacking sequence. There are two types of stacking faults in fcc crystalls: (i) extrinsic and (ii) intrinsic. Both types are depicted in Fig. 2.1. Extrinsic stacking fault forms as an additional layer in the crystal structure: ABCABCABC alternation changes locally to ABC-ABAC-ABC [cf. Fig. 2.1"B"]. In the case of internal stacking fault, the regular alternation ABCABCABC changes to ABC-AB-ABC [cf. Fig. 2.1"C"].

2.1.2 Magnetic anisotropy

The presence and coupling of spin and orbital moments in magnetic materials leads to complex and anisotropic interactions between them. Spontaneous net magnetization of ferromagnets stabilize along so-called easy directions below Curie temperature without

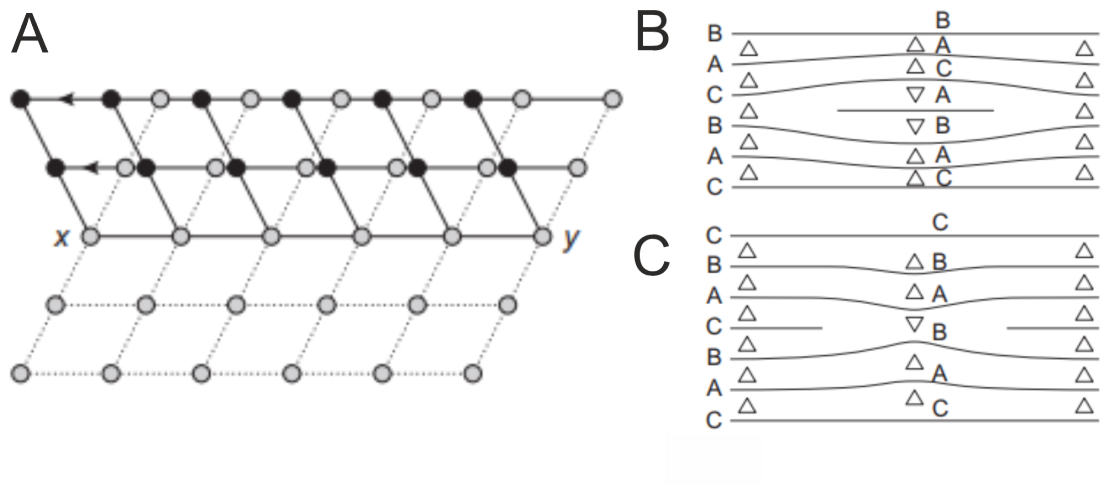

Figure 2.1: Examples of lattice defects: panel A shows twinning boundary, panels B and C show extrinsic and intrinsic stacking faults in fcc structure, respectively [48].

presence of external magnetic field. The energy that is needed to rotate the magnetization from a magnetic easy to a hard direction is called magnetic anisotropy [49]. There are several types of magnetic anisotropy contributions: shape, magnetocrystalline, surface anisotropy and defect-induced magneto-elastic contributions. In a cubic crystal magnetic anisotropy can be written as $E_0^{cubic}(\vec{m})/\upsilon = K_1 m_{z'}^2 + K_2 m_{y'}^2 + K_4^{MC}(m_{x'}^2 m_{y'}^2 + m_{x'}^2 m_{z'}^2 + m_{y'}^2 m_{z'}^2) + K_6^{MC} m_{x'}^2 m_{y'}^2 m_{z'}^2 + ...$, where υ is magnetic volume, x', y' and z' are [100], [010] and [001] crystal axes, respectively, K_i are the respective anisotropy constants (due to cubic symmetry $x', -x', y', -y', z', -z'$ directions are identical and only even terms are present), $m_{i'}$ are the unit vector projections along respective crystal directions [38]. In more general terms, $K_{eff} = E_0/\upsilon$. The reported anisotropy constant values of cobalt vary over orders of magnitude due to complexity of experiments and theoretical approaches involved for the constant determination. In Tab. 2.1 few examples from the literature are listed. There, a variety in size, morphology, magnetization, and measurement conditions can be found.

Magnetocrystalline anisotropy is determined from the crystal symmetry and is usually small for transition metals with the exception of hcp cobalt, which has a strong uniaxial anisotropy. For fcc cobalt there are four easy directions along $\langle 111 \rangle$ directions and three hard axes along $\langle 100 \rangle$ respective directions. Due to the finite size of the nanoparticle, surface atoms with broken symmetry occupy a large fraction of the volume of the nanoparticle, which gives rise to *surface* magnetocrystalline anisotropy. Its value depends on the atomic coordination at each site of the nanoparticle and can be calculated as a magnetic pair interaction energy between atoms. According to the Néel's anisotropy model

D (nm)	Struc-re	M. moment	Anisotr. const.
4.3[a]	fcc	1.72 μ_B/at.	K_1=-0.22 $\frac{MJ}{m^3}$ K_2=0.09$\frac{MJ}{m^3}$ K_4=0.01$\frac{MJ}{m^3}$
4.5[b]	MT fcc	1400 kA/m	K_{eff}=0.01-0.423$\frac{MJ}{m^3}$
1.8-4.4[c]	fcc	0.5-5·10$^3\mu_B$	K_{eff}=5-30·10^6 $\frac{erg}{cm^3}$
1.9-5.5[d]	fcc	-	K_{eff}=110-218kJ/m^3 K_2=0-1.2K_{eff}
4.4[e]	fcc	-	K_{eff}=1.5·10$^6 erg/cm^3$
12[f]	fcc	1428.6 emu/cm^3	$K_1 = -3.8\frac{meV}{atom}$ $K_2 = -0.77\frac{meV}{atom}$
2.5[g]	-	2.2 μ_B/at.	$K_{eff} = 0.8\frac{meV}{atom}$
5-30[h]	fcc	-	K_{eff}=$10^4 \cdot Jm^3$
5-30[i]	fcc	2.2-4.6 μ_B/at.	K_{eff}=72 meV
1.5-2.5[j]	fcc/hcp	1.94-2.1 μ_B/at.	K_{eff}^{fcc}=0.45$\frac{MJ}{m^3}$ K_{eff}^{hcp}=0.25$\frac{MJ}{m^3}$

a Ref. [38]; 35 mK; 1072 at., b Ref. [8]; exp. and theor., c Ref. [6], d Ref. [5], e Ref. [50], f Ref. [11], g Ref. [51]; nanoislands, h Ref. [52]; T=35 mK, i Ref. [4]; nanoislands, j Ref. [9]; T=35 mK.

Table 2.1: Variety of magnetic anisotropy constants of cobalt nanoparticles. Here D is average diameter of the nanoparticles, magnetic moments are listed sometimes for the whole particle and sometimes per atom while it is impossible to bring all the values to homogeneous units, similarly for anisotropy constants K values are taken directly from the articles, in footnote experimental conditions, form-factors (if not a sphere) are mentioned.

[53], atomic magnetic moments on the surface of the nanoparticle are oriented parallel to each other. In this case, symmetrical nanoparticles will have a zero contribution to the surface anisotropy since $E^{surface} = L(\vec{m} \cdot \vec{e})$ [38] terms cancel each other for symmetrical atoms, (here $\vec{m}$ is magnetization unit vector and $\vec{e}$ is interatomic vector, L is Néel constant). Later, another surface anisotropy model was demonstrated by Garanin *et al.* [39]. There, surface atoms can be canted away from a common axis which results in a non-trivial surface anisortopy term. It has been shown that sizeable enhancement of magnetic anisotropy can be found for 8-12 nm nanoparticles with strong surface anisotropy contribution ($|K_s/K_4| > 500$, where K_s is a surface anisotropy constant and K_4 is called K_1 in the article) [11].

Shape of the nanoparticle gives rise to another type of magnetic anisotropy which arises from the demagnetizing field that tends to minimize long-range dipolar interactions between atoms in the nanoparticle. Shape anisotropy can be written as $E_{shape}(\vec{m}) = -\frac{3\mu_{at}^2}{2}\sum_{i\neq j}\frac{(\vec{m}\cdot\vec{r_{ij}})^2}{\|\vec{r_{ij}}\|^5}$.

Ferromagnetic nanoparticles are expected to exist in single domain regime below cer-

tain radius R_{sd} that is called single domain radius, which can be calculated as $R_{sd} = \frac{9(AK_u)^{1/2}}{\mu_0 M_s^2}$ where A is the exchange constant, K_u is the uniaxial anisotropy constant, μ_0 is magnetic permeability of vacuum, M_s is the saturation magnetization. At this regime domain walls start to be energetically inefficient and the particle forms a uniform domain and can be characterized by so-called macro-spin, proportional to the number of atoms in the particle. Jamet *et al.* determines R_{sd} equal to 34 nm [38] but there is a large dispersion of R_{sd} in literature. Tab. 2.2 shows few of them, however, it is safe to consider nanoparticles with $R < 13$ nm as macro-spins.

R_{sd} (nm)	Structure	Ref.
13-135	fcc	[54]
34	hcp	[38]

Table 2.2: Single domain sizes estimations for cobalt nanoparticles.

Although shape and surface anisotropy can cause sizeable enhancement of magnetic anisotropy, they do not explain an existence of ferromagnetic states even for 12 nm cobalt nanoparticles [11]. Such magnetically blocked states are rather attributed to the presence of lattice defects such as dislocations, stacking faults and twinning boundaries in the particles. Cobalt nanoparticles were reported to have twinning boundaries with strain propagating throughout the particle [8, 11]. Structural defects can contribute in magnetic properties of cobalt in many experimental works although their effects are rarely discussed [11, 23, 52, 55].

2.1.3 Magnetization reversal

In a single domain nanoparticle with uniaxial anisotropy magnetization direction can switch between two distinct states separated by an energy barrier. Néel has proposed a model explaining stability and magnetic properties of nanoparticles in a size range between 1 and 5 nm. According to Néel-Arrhenius law, relaxation time of a single domain nanoparticle with uniaxial anisotropy decreases exponentially with temperature growth: $\tau_m = \frac{1}{\nu_0} e^{\frac{E_m}{kT}}$, where E_m is magnetic energy barrier of the particle, k is Bolzman's constant, T is a temperature, ν_0 is switching probability which depends on crystal symmetry and material and equals 1.9 $10^9 s^{-1}$ for fcc cobalt at room temperature [56, 34]. Magnetic blocking concept is widely used to explain stability of the nanoparticles during the experiment. Nanoparticle is called magnetically blocked if its relaxation time τ_m is larger then the measurement time τ_x. Those nanoparticles which fluctuate with $\tau_m < \tau_x$ are called

superparamagnetic. Recently cobalt nanoparticles have been reported to have magnetic blocking states at sizes as low as 10 nm with magnetic anisotropy barriers higher then 0.63 eV, although normally 10 nm nanoparticles are associated with superparamagnetism [11]. These blocked states have been attributed to internal defects in the crystalline structure of the nanoparticles.

2.2 Correlation of structure and magnetism of magnetic nanoparticles

Nowadays, there are only few methods that can address magnetism and structural properties simultaneously [16, 14, 20]. There are a number of publications cited in Tab. 2.1 with respective structures and magnetic anisotropy values. The broad distribution of magnetic anisotropy values and magnetization of the nanoparticles are reported even for narrow size distributions of nanoparticles, which could be explained by a rich structural variation of the nanoparticles. In Chapter 4 of this Thesis we address this issue by a combination of x-ray magnetic investigations of individual nanoparticles by means of XPEEM and structural characterization with HAADF-STEM.

2.3 Oxidation of metallic cobalt

Pure metallic cobalt nanoparticles are highly reactive to ambient conditions, and are therefore partially or fully oxidized after exposing them to ambient air. Since surface atoms of the nanoparticles constitute a large fraction of the total number of the atoms in the nanoparticle, surface functionalization and hence modification of atomic arrangement on the surface of nanoparticles can lead to significant changes of magnetic properties of the particles. The *in situ* oxidation of cobalt nanoparticles has been studied for instance by S. Barthling *et al.* [27], and Vasiliki Papaefthimiou *et al.* [57]. Barthling *et al.* have shown that controlled oxidation can lead to a fully oxidized, polycrystalline state with small Co_3O_4 crystallites. In contrast, a stable metallic cobalt core fcc CoO shell structure in oxidized cobalt nanoparticles was found by Wiedwald *et al.* [58]. Cobalt forms two stable antiferromagnetic oxides, CoO and Co_3O_4 oxide, where CoO crystalizes in a rock salt structure [59] and Co_3O_4 in a spinel structure [60] with Néel temperature of 293 K and $29-33$K [61], respectively. Up to now it stays unclear how the oxidation of the surface starts, whether certain sites of the nanoparticle react faster then another as it is proposed for Ag oxidation [62] and at which stage oxidation reaction stabilizes. Papaefthimiou *et al.*

[57] proposed that in the *in situ* oxidized cobalt nanoparticles a tetrahedral wurtzite structure can form, which acts as a reaction barrier and may stabilize the oxide shell formation, but the structure of the particles and the role of carbon from their substrate remained unclear. Previous studies on the evolution of Co-oxide nanoparticles include the oxidation of nanoparticles ensembles rather than of single isolated nanoparticles [63]. In Chapter 5 of this thesis we present the structure and magnetic properties of *in situ* oxidized single cobalt nanoparticles at early stages of oxidation.

2.4 Interactions with laser pulses

Laser excitation of nanostructures can be an effective and fast tool to manipulate magnetic properties and stability of the nanoparticles. Namely, absorption of a laser photon increases overall energy of the particle which results in possible overcome of energy barrier stabilizing magnetization. So far, it has been shown in ferrimagnetic thin films, that a single laser pulse with circular polarization can locally switch magnetization of the film. In the pioneering work, Stanciu *et al.*[31] has shown that perpendicular magnetic domains in GdFeCo thin film can be switched locally by sweeping laser light over the sample with all-optical switching effect. This changes could be reversed by switching laser polarization from σ^+ to σ^-. Later it was shown that for ferromagnetic thin films the switching process happens upon multiple shots with step-wise formation of multiple-domain structure with further helicity-dependent switching [64]. Recent demonstration of all-optical switching in a single Co film and in a Co/Ni multilayer [33] is particularly striking, since it potentially opens up the intriguing possibility to achieve switching also in isolated *3d* transition metal nanoparticles. They also provide an intrinsic single domain ground state, which will allow us to evaluate the unknown role of multi-domain states for all-optical switching in previously studied thin film or micron-sized systems. As such, cobalt nanoparticles present an ideal model system to study the interaction of an ultrashort laser pulse with magnetic matter.

It has been reported that cobalt nanoparticles have significantly low energy barriers around 0.63 eV at room temperature [11]. This value is comparable to an optical photon energy and thus in general it can be possible to manipulate the magnetization of the nanoparticles by means of single photons. Moreover, Kleibert *et al.* have shown that static heating to 470 K increases stability of cobalt nanoparticles at room temperature [11]. There are several effects that come to play upon laser interaction to the magnetic media. As discussed before, switching rate of the nanoparticles increases exponentially

with the temperature growth. Thus, heating the nanoparticle even by few Kelvin can significantly increase its switching rate and transfer a magnetically blocked nanoparticle to a superparamagnetic for some time. The second effect is associated to the full demagnetization of the nanoparticles due to heating to the Curie temperature (T_c). Curie temperature of nanoparticles are expected to be lower then for the bulk. According to Wang *et al.* [3] T_c can be approximated as $T_c(d) = T_c(\infty)[1 - \frac{d_0}{D}^{\frac{1}{\nu}}]$ where $\nu = 0.82 \pm 0.02$ is a scaling exponent and $d_0 = 0.51 \pm 0.02$ nm is a microscopic length scale close to the lattice constant. $T_c(\infty)$=1390 K is Curie temperature for bulk cobalt [65]. Heating of blocked cobalt nanoparticles with single leaser shots is discussed in Chapter 6.

Chapter 3

Experimental details

In this Chapter, we explain the sample preparation and the production technique of cobalt nanoparticles. Further, the characterization technique for magnetic microscopy and spectroscopy using polarized x-rays on individual nanoparticles, the laser setup and scanning transmission electron microscopy measurements for structural investigations are described. Our experimental results for x-ray magnetic circular dichroism imaging were acquired using the x-ray photo-emission electron microscope (XPEEM) at the Surface/Interface: Microscopy (SIM) beamline at the Swiss Light Source, at Paul Scherrer Institut. Morphology and structure of the nanoparticles were measured using high-angle annular dark field scanning transmission electron microscope at the EMAT center for Microscopy, at the University of Antwerp. In this work we concentrate purely on cobalt nanoparticles produced with arc cluster ion source at SIM beamline.

3.1 Sample preparation

The samples were prepared in three steps. First, marker structures were deposited on the substrates. Second, samples were heated to desorb adsorbates from ambient air to avoid oxidation of the nanoparticles when landing on the substrate. Third, cobalt nanoparticles were deposited. The sample preparation procedure is sketched in Fig. 3.1. We used two different substrates in our experiments: (a) transmission electron microscopy (TEM)-compatible silicon wafers with holes covered with silicon nitride membrane from SiMPore Inc. © [66] and (b) square silicon wafers with a native oxide layer [cf. Fig. 3.1(a-b)]. The preparation steps are denoted with numbers below the Figure.

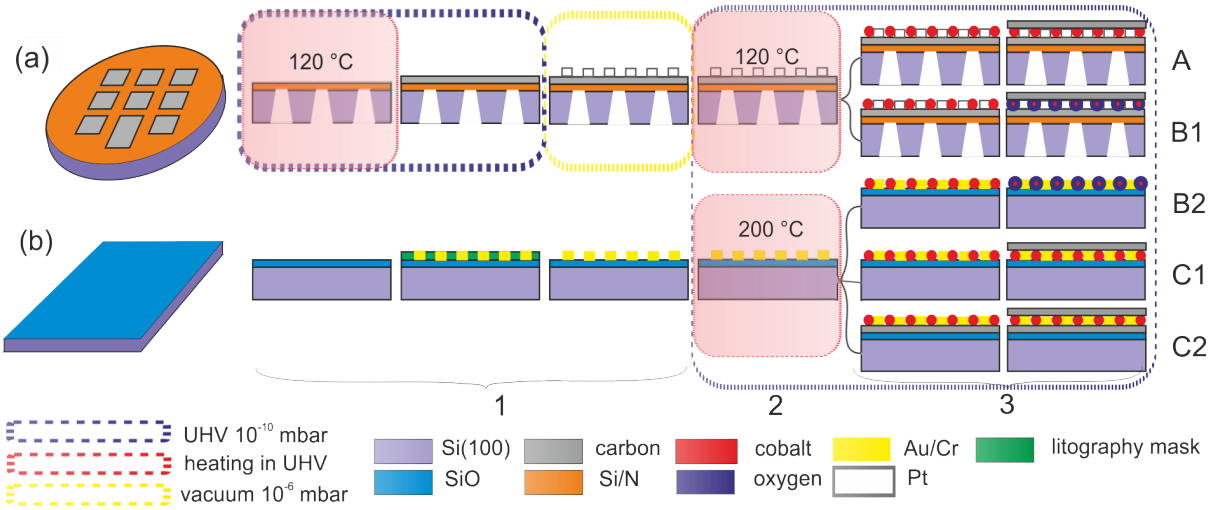

Figure 3.1: The sample preparation procedure for two types of substrates : (a) TEM-compatible silicon substrate with 10 nm thin SiN membranes free standing on top of the holes and (b) silicon (100) square wafer with a native oxide layer on top. The samples were used for the experiments in Chapter 4 ("A"), Chapter 5 ("B1" and "B2") and Chapter 6 ("C1", "C2"). The details of the sample preparation are discussed in Section 3.1.

3.1.1 Marker structure deposition

The marker structures, deposited at the step 1, were used for unambiguous identification of the same nanoparticles in x-ray XPEEM, high-angle annular dark field scanning transmission electron microscopy (HAADF-STEM) and scanning electron microscopy (SEM). For samples on **TEM-compatible substrates**, Pt markers were used. Before Pt markers deposition, the substrates were heated to desorb the adsorbates and covered with 1-2 nm of amorphous carbon. Then the membranes were transferred to a SEM device with focused ion beam (FIB) functionality. There a number of marker structures were deposited by thermal decomposition of Pt precursor molecules with help of electron beam on the membranes (cf. Appendix A). For samples on **silicon wafers**, the Au/Cr markers were deposited using the lithography process.[1]

3.1.2 Substrate annealing

After the markers deposition, all samples were transferred to the ultrahigh vacuum (UHV) preparation system [cf. Fig. 3.2(b)]. Before the nanoparticles deposition, the substrates

[1] Au/Cr marker deposition on the samples was done by Anja Weber from Mesoscopic Systems group at PSI, Pt deposition training was done by Elizabeth Müller from Electron Microscopy Facility at PSI, Pt marker structures deposition was done by Elizabeth Müller and me.

were annealed in the PS (TEM-membranes were heated up to 120°C, the silicon wafers were heated to 200°C) with a base pressure of the order of 10^{-10} mbar at 1.2 A heating current for membranes and 2 A for silicon wafers, respectively, and let cool down to room temperature. Then cobalt nanoparticles were deposited.

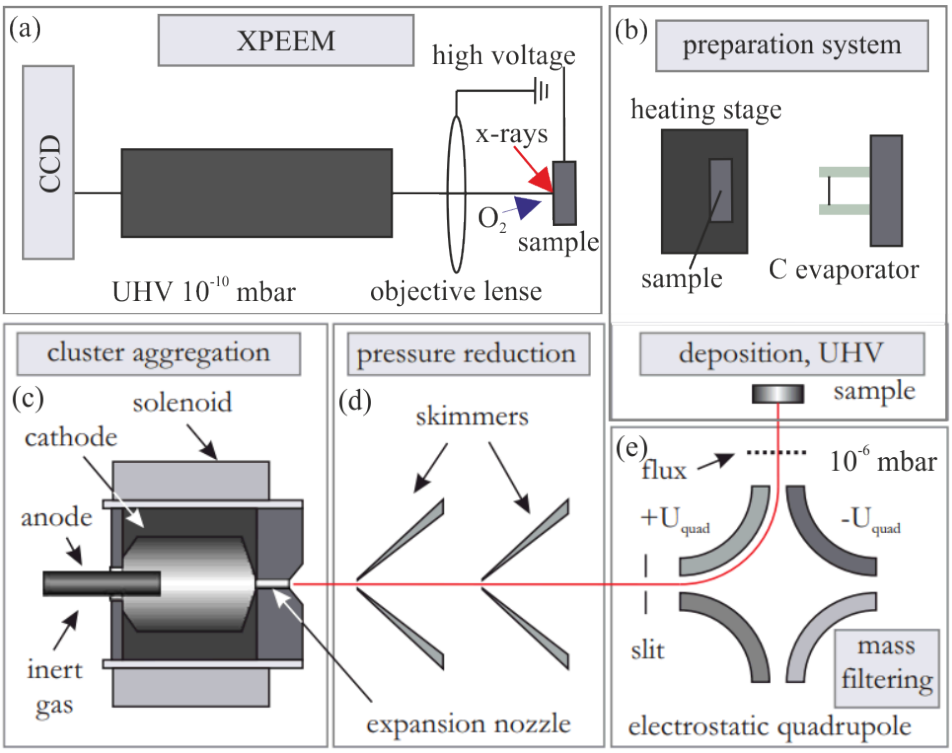

Figure 3.2: Schematic drawing of the chambers at SIM beam line. (a) X-ray photo-emission electron microscope (XPEEM). X-rays impinging the sample at grazing incidence angle. The secondary photo-electrons are accelerated towards the objective lens with high voltage. The imaging system is schematically depicted with grey rectangle. The image is acquired with CCD camera. (b) Preparation system contains the manipulator with heating stage and contacts for temperature sensing from the sample. The carbon evaporator is placed next to the manipulator. (c-e) Arc cluster ion source (ACIS) schematics from [67]: (c) cluster creation system, (d) pressure reduction collimator, (e) mass filter and sample substrate.

3.1.3 Cobalt nanoparticles preparation

Cobalt nanoparticles were prepared using an UHV compatible arc cluster ion source (ACIS) [cf. Fig. 3.2(c-e)] [68]. This system is directly attached to the preparation system [cf. Fig. 3.2(b)] and the sample can be transferred to the XPEEM [cf. Fig. 3.2(a)] without

breaking the ultra-high vacuum conditions. An electric arc at 2 kV is produced in the cluster creation system [cf. Fig. 3.2(c)]. similar to the Ref. [11], an electrostatic quadrupole mass-filter [cf. Fig. 3.2(e)] is used to deposit nanoparticles with diameters varying from 8 to 25 nm on the substrates. The nanoparticles are deposited on the substrates under so-called soft landing conditions, with the kinetic energy of the nanoparticles being lower than 0.1 eV/atom [68], so that the particles do not fragment or damage the substrate upon landing [69, 70]. Previous work has shown that the substrate and the deposited cobalt nanoparticles are thermally stable up to 800 K [68].

The number of nanoparticles on the sample was controlled by integrating the charge collected on a gold mesh (not shown) placed in the particle beam. Resulting nanoparticles have size distribution of 12.0±1.4 nm and presumably fcc structure [11]. The coverage is set to about one nanoparticle per μm^2 in order to avoid inter-particle interactions and to be able to resolve individual nanoparticles in XPEEM, which has a spatial resolution of about 50 nm. After nanoparticle and carbon deposition, the samples are transferred *in situ* to the XPEEM instrument at the SIM Beamline [71].

The very last step of the sample preparation differs depending on the experiment. For the combined XPEEM and STEM characterization of cobalt nanoparticles (cf. **Chapter 4**), the sample was covered with another layer of amorphous carbon (cf. Fig. 3.1 "A"). This procedure allows producing of long lasting sample to prevent chemical reactions of the nanoparticles with residual gas molecules during the XPEEM experiments (base pressure $< 5 \cdot 10^{-10}$ mbar) which may involve hours of intense x-ray illumination [30] and avoid oxidation while transferring to the (HAADF-STEM) device.

For the structural characterization of *in situ* oxidized cobalt nanoparticles, described in **Chapter 5**, TEM-compatible membranes were used (cf. Fig. 3.1 "B1"). To oxidize the nanoparticles we introduce molecular oxygen into the XPEEM chamber [cf. Fig. 3.2(a)] through a leak valve (not shown); dosages of 0.5, 1, 2, 5, 10, 20, 40 L (1 L = 10^{-6} Torr s = 1.3×10^{-6} mbar s) are employed in our experiments. For XPEEM investigations of *in situ* oxidized cobalt nanoparticles, another type of substrate, namely square shaped silicon wafers [cf. Fig. 3.1(b)] were used. After the nanoparticles deposition [cf. Fig. 3.1"B2"], the sample was exposed to the molecular oxygen similarly to the TEM-compatible membranes case. Lastly, for the laser induced manipulation of cobalt nanoparticles (**Chapter 6**), the nanoparticles were deposited on the silicon wafer in one case [cf. Fig. 3.1"C1"] and on the silicon wafer covered with amorphous carbon prior to the particles deposition [cf. Fig. 3.1"C2"] to avoid a direct contact of the nanoparticles with the native oxide layer as discussed later in Chapter 6.

3.2 Resonant x-ray imaging. X-ray photo-emission electron microscopy

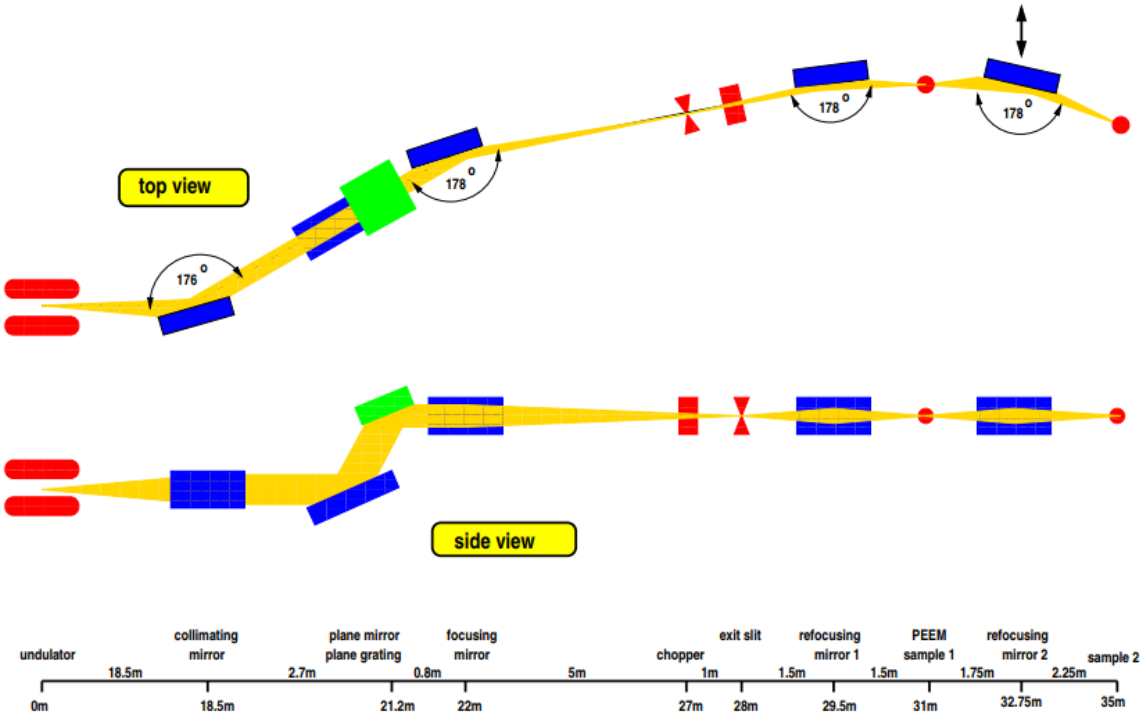

Figure 3.3: Schematics of SIM beamline [72].

X-ray characterization of magnetic materials is a powerful tool to investigate element-specific phenomena at high spatial and temporal resolution [73, 74]. Synchrotrons operate high current beams of relativistic electrons with GeV kinetic energies orbiting under magnetic field. The beam cycles in the storage ring and passes through so-called insertion devices (IDs), resulting in a strongly forward-focused x-ray beam. Employing the XMCD effect, XPEEM helps to visualize magnetic moment projection with high spatial resolution.

3.2.1 X-ray radiation

High-end spectroscopic and imaging techniques are possible because of high brilliance and monochromatic light from modern light sources. Modern light sources, such as Swiss Light source with 2.4 GeV electron energy [75], use undulators to produce x-ray radiation. Undulator is a structure consisting of an array of permanent magnets with controlled gap and phase between the arrays. Electrons wiggle while passing through the undulator

and emit x-ray radiation with intensity I $\sim N^2$, where N is a number of dipoles in the undulator. SIM beamline has two insertion devices which reduces the switching time between two different polarizations/energies. It is also possible to change polarization of x-rays by reconfiguring the incertion device. Further x-rays are passing through the monochromating gratings and exit slit before they reach the sample (cf. Fig. 3.3).

3.2.2 X-ray photo-emission electron microscopy

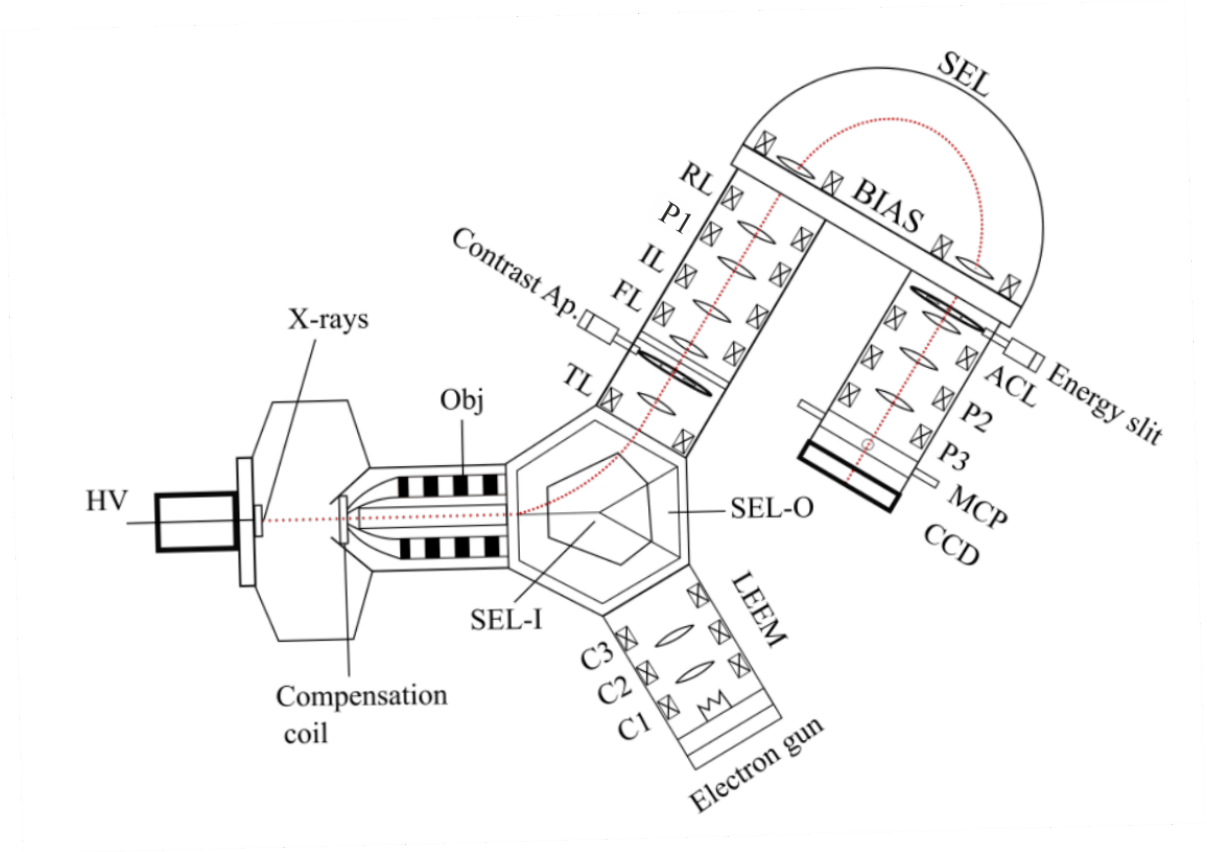

Figure 3.4: XPEEM schematics from [76].

X-ray photo-emission electron microscopy is a micro-spectroscopy tool for structural, chemical and magnetic characterization of materials with 50 nm spatial resolution and element sensitivity. The samples are illuminated using polarized monochromatic x-ray radiation with the photon energy tuned to a resonant absorption edge, like for example the Co L_3 edge at 781 eV and impinging on the sample at a grazing angle of incidence of 16° (cf. Fig. 3.4). The XPEEM technique is based on probing electrons emitted from the sample upon x-ray excitation. Photon absorption by the material is followed by emission of primary photoelectrons and Auger electrons which generate a cascade of

secondary photo-electrons through inelastic and quasi-elastic interactions between electrons, plasmons and phonons [77]. For each element there are specific resonant energies corresponding to certain electron transitions. For cobalt we employ so-called L_3 edge where 2p to 3d electron transition occurs. At this photon energy the cobalt nanoparticles appear as bright spots in the microscope [cf. Fig.3.5(a)]. Ideally, each of the spots corresponds to a single nanoparticle. The 20 μm field of view of XPEEM allows simultaneous measurement of about 400 nanoparticles.

The schematics of XPEEM microscope is presented in Fig. 3.4. There, on the very left the sample is marked by a rectangle. The sample is set to the high voltage of 10-20 kV in order to accelerate secondary electrons from the surface towards the XPEEM. After the photoelectrons are extracted from the sample, they pass through the electron optics with energy analyzer correcting the chromatic aberrations. Eventually, electrons run into a multi channel plate (MCP) which multiplies the signal before the phosphorous screen which is observed with a CCD camera. We can adjust electron optics and change field of view of the microscope between 10 and 100 μm.

3.2.3 X-ray magnetic circular dichroism effect

For magnetic characterization of individual nanoparticles in XPEEM the x-ray magnetic circular dichroism (XMCD) effect is employed. This effect originates in spin-dependent photon absorption [77]. Namely, C_+ photon absorption would be higher than for C_- at Co L_3 absorption edge where $2p_{3/2} \rightarrow 3d$ transition happens and reverses the sign at L_2 energy. Such difference for circularly polarized light is purely attributed to magnetism and is the strongest at resonance energies (cf. Fig. 3.6).

The magnetic signal depends on the relative orientation of the magnetic moment $\vec{m}$ and the x-ray propagation vector $\vec{k}$: $A \sim \vec{m} \cdot \vec{k}$. The value reaches its maximum when two vectors are parallel, and minimum for the anti parallel orientation of $\vec{m}$ and $\vec{k}$.

3.2.4 Single particle identification

To obtain magnetic contrast maps, two XPEEM images are recorded subsequently with circularly left and right (C_+ and C_-, respectively) polarized x-rays at the Co L_3 x-ray absorption edge (781 eV) see Fig. 3.5. All image sequences are normalized by pixel-wise division by a flat field image in order to correct for non-uniformity in the XPEEM multichannel plate phosphor screen detector unit. Flat field images are obtained by defocusing the microscope such that a homogeneous illumination of the XPEEM detector

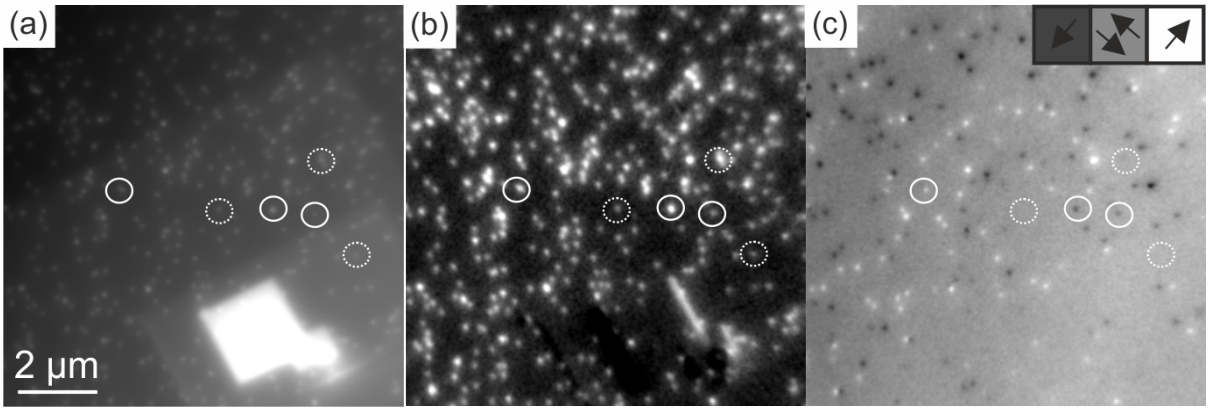

Figure 3.5: (a) XPEEM image taken at Co L_3 edge with C_+ polarized light, marker structure that helps identifying individual nanoparticles in the field of view is visible as a bright rectangle. (b) Elemental contrast map where white dots correspond to individual nanoparticle. (c) Magnetic contrast image where dots with different grey level contrast correspond to a projection $\vec{k} \cdot \vec{m}$ where $\vec{k}$ is x-ray propagation direction, $\vec{m}$ is nanoparticle's magnetization direction. White circles highlight magnetically blocked nanoparticles, dashed circles highlight nanoparticles without magnetic contrast (cf. Section 3.2.4). The inset with arrows in the upper right corner depicts magnetic contrast variation depending on the in-plane magnetization orientation.

is achieved. The normalized images are then drift-corrected. Magnetic contrast maps are obtained by pixel-wise division of the two normalized and drift-corrected images with C± polarization. The resulting magnetic contrast of individual nanoparticles ranges from black to white depending on the projection of their magnetic moment m onto the x-ray propagation direction k according to $A \sim \vec{m} \cdot \vec{k}$, cf. Fig.3.5. The best time resolution of magnetic characterization in the present experiments is 20 s which is determined by the total time to acquire two images with C± polarization. For the data shown in Fig. 3.5, sequences of 20 consecutive magnetic contrast maps are averaged (resulting in a total τ_x=400 s). Chemical characterization of the nanoparticles is achieved through x-ray absorption (XA) spectroscopy by recording image sequences with linearly polarized x-rays in the photon energy range between 775 eV and 785 eV around the Co L_3 edge with energy steps ranging from 0.1 eV to 1.0 eV, cf. Fig. 3.6. Each sequence is flat field normalized and drift-corrected. Then spectra of individual nanoparticles are obtained by extracting the image intensities from small areas (e.g. 5 × 5 pixels) centered on the position of the corresponding bright spots in the XPEEM images. In order to normalize for variations in the incoming x-ray flux the nanoparticle intensities are divided by the signal extracted in an area of same size next to the nanoparticle. For the present work

we average the spectra of about 30 nanoparticles to achieve spectra such as shown in Fig. 3.6. In our work we do not correct for the absolute position of the XAS after the measurement, therefore in Chapter 6 the spectra appear shifted to the higher absorption energies.

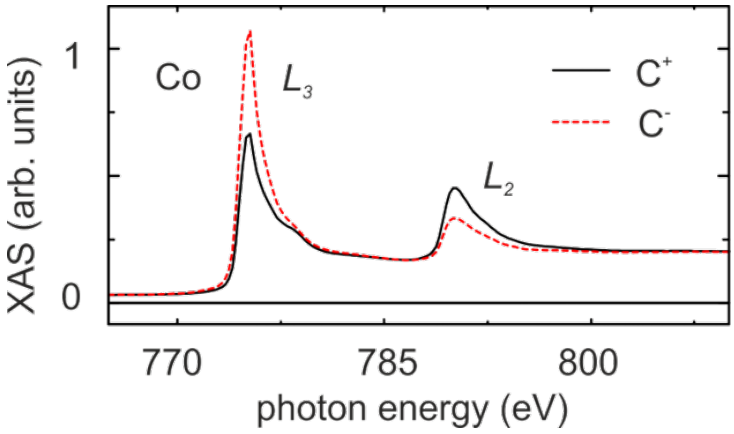

Figure 3.6: XAS spectrum of metallic cobalt [67].

Similar to work by Kleibert *et.al.* [11], a large portion of nanoparticles (approximately one half of the sample) exhibit stable magnetic contrast at room temperature with contrast levels ranging from white to black, which reflects the random orientation of the magnetization of the nanoparticles upon the deposition process. Such nanoparticles are magnetically blocked within the measurement time with a relaxation time $\tau_m > \tau_x$. Using an Arrhenius-type law for the thermally induced magnetic switching rate $\nu = \nu_0 \cdot e^{-E/k_B T}$ with T being the temperature, k_B the Boltzmann constant, and the attempt frequency ν_0 = 1.9 $\cdot 10^9 s^{-1}$ for fcc cobalt nanoparticles at room temperature together with $\nu = 1/\tau_m$, a lower limit of the magnetic energy barrier of these nanoparticles can be estimated to $E_m \geq 0.63$ eV [11]. This value is strongly enhanced when compared to the anticipated magnetic energy barriers of spherical fcc cobalt nanoparticles in the present size range and is assigned to structural defects in the nanoparticles [11]. Several magnetically blocked nanoparticles are highlighted with solid circles in Fig. 3.5.

Also, similar to the earlier experiments, we find that a larger number of particles exhibit no magnetic contrast, for instance those that are highlighted with dashed circles in Fig. 3.5. A smaller fraction of these particles (about 20%) might also be magnetically blocked, but with magnetization orthogonal to the x-rays propagation direction ($\vec{m} \perp \vec{k}$), assuming a random orientation of the magnetic moments and that the signal to noise ratio in the present data is similar to that of in [12]. However, the remaining nanoparticles do not have magnetic contrast, due to either thermally induced fluctuations with $\tau_m \leq \tau_x$ and

thus, they are either in a superparamagnetic state, or they have more complex magnetic structure not resolvable with XPEEM. The two abovementioned magnetic states were found to occur irrespective of the size of the (near spherical) nanoparticles in similar samples [11]. The similarity of the present findings in the pristine state and the data in Ref. [11], suggests that the carbon capping has no noticeable impact on the magnetic behavior of the cobalt nanoparticles.

The third variation of magnetic contrast of cobalt particles, which can be selected out of the second group, is so-called fluctuating nanoparticles. For such particles, $\tau_m \sim \tau_x$ and magnetic contrast fluctuates between single 20 s magnetic contrast maps. Summing up, we divide the nanoparticles into three groups depending on their magnetic contrast variation visible with XPEEM magnetic contrast imaging: (i) magnetically blocked with $\tau_m > \tau_x$, (ii) superparamagnetic with $\tau_m < \tau_x$ and (iii) fluctuating with $\tau_m \sim \tau_x$. We will refer to these groups later.

3.3 Quantitative XPEEM data analysis

The method of contrast analysis has been developed earlier and is described in details in Ref. [34]. A signal from a single particle appears broader in XPEEM images than the actual size of the nanoparticle due to a Gaussian broadening. Therefore, the elemental contrast of the nanoparticle is approximated with a 2D Gaussian of 13×13 pixel^2 on a planar background. After subtracting the planar background, two intensities of respective C_+ and C_- signals are calculated as the heights of the respective Gaussians. The XMCD asymmetryis calculated as $A = (I_{C_+} - I_{C_-})/(I_{C_+} + I_{C_-})$. The magnetic contrast is proportional to the projection of the magnetic moment of the nanoparticle on the x-ray propagation direction and gives a qualitative information about the magnetization of magnetically blocked nanoparticles.

3.4 Laser setup

For the laser-based experiments, an XL-500 oscillator (FEMTOLASER GmbH) with 50 fs laser pulses of 800 nm wavelength at 5.2 MHz repetition rate is used. The laser beam is aligned in the XPEEM instrument using a Cs covered sample, which permits direct imaging of the laser spot. A schematics of the laser setup is given in Fig. 3.8. The laser beam impinges at a grazing angle of 16° with respect to the sample surface. The laser pulse energy at the sample is set using a half wave plate and a polarizing beam splitter. A

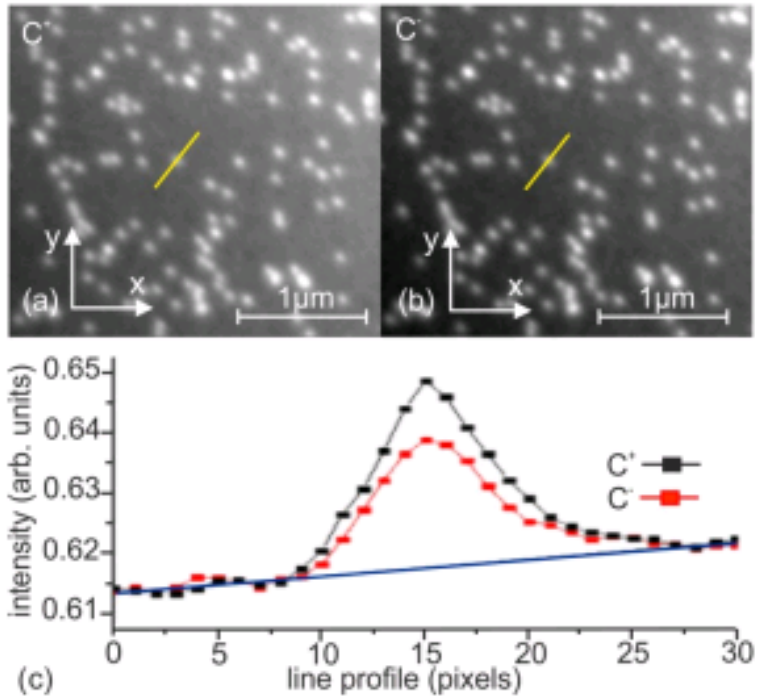

Figure 3.7: Data analysis illustration from [34]. (a) Elemental contrast map at Co L_3 absorption edge with σ_+ polarized light. Bright dots correspond to cobalt nanoparticles. One of the particles is highlighted with yellow line in order to acquire a linear intensity profile. (b) Elemental contrast map of the very same region of the sample at Co L_3 absorption edge acquired with σ_- polarized light. (c) Linear profile of the nanoparticle highlighted in (a) and (b). Black curve corresponds to σ_+, red curve - to σ_-, respectively. Blue line shows a linear background in the image.

fast photodiode is used to monitor the intensity of each laser pulse in a reference beam. The intensity at the sample is initially calibrated using a photo diode mounted on a sample holder and measuring the laser intensity directly at the sample position in the XPEEM instrument. All pulse energies are measured relative to this measurement and the measured laser power and repetition rate. The grazing incidence gives rise to an elliptical laser spot profile with dimensions of $\mathrm{FWHM}_x = (20\pm5)\mu\mathrm{m}^2$ and $\mathrm{FWHM}_y = (73\pm18)\mu\mathrm{m}^2$, respectively. Assuming an elliptical Gaussian intensity distribution the peak fluence can be calculated by $F_0 = 4ln2 \cdot E/(p \cdot FWHM_x \cdot FWHM_y)$ with E being the energy of the laser pulse. Tab. 3.1 shows the investigated laser pulse energies, the resulting peak fluences together with the corresponding photon densities at the sample. Further, a CCD camera is placed in the focus of the reference beam to monitor possible pointing variations. A quarter wave plate is used to switch the polarization of the laser pulses

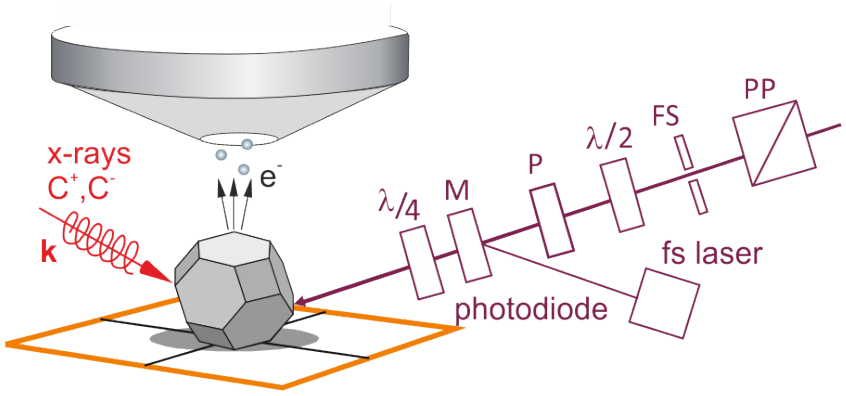

Figure 3.8: Schematics of the experimental setup: polarized x-rays and the femtosecond laser beam impinge at a grazing of 16°. The laser setup uses a combination of a pulse picker (PP) and a fast shutter (FS) to select individual laser pulses (50 fs), the laser intensity is tuned by a $\lambda/2$ wave plate and a polarizer (P), a fast photodiode is used for intensity and pulse monitoring from a leaking mirror (M), and a $\lambda/4$ wave plate is used to set the laser polarization.

between linear, C_+ and C_-. A strain free UHV viewport is used to couple the laser pulse into the PEEM instrument with minimal impact on the polarization. Single laser pulses are selected using a pulse-picker (PP) and a fast mechanical shutter (FS) [71].

Laser pulse energy E(nJ)	14 ±1	65±3	150±8	270±14	352±18
Peak fluence F_0 (mJ/cm^2)	1±1	4±1	9±3	16±6	21±8
Photon density n_{Ph} (ph./nm^2)	35±10	160±60	370±130	660±240	860±310

Table 3.1: Investigated laser pulse energies, peak fluences, and respective photon densities with estimated errors.

The response of the nanoparticles to the laser pulses is measured by recording a number of magnetic contrast maps before and after controlled laser pulse exposures. In detail, ten subsequent XMCD images are taken without laser excitation as a control experiment to determine the initial magnetic state of the nanoparticles and to distinguish possible laser induced magnetic switching events from thermally induced spontaneous flipping of some of the nanoparticles at the given conditions [11]. Then the sample is excited by ten laser pulses with identical laser polarization and similar intensity. After each laser pulse, an XMCD contrast map is recorded (cf. Fig. 3.8). To check chemical integrity of the sample during the experiments XA spectra are acquired as described above for each investigated laser intensity at the beginning of the experiment and in the

end.

3.5 High-angle annular dark field scanning transmission electron microscopy

For structural characterization of the samples on the TEM-compatible membranes, a FEI "Titan^3" microscope equipped with Cs probe corrector with high-angle annular dark-field detector (HAADF) was used.[2] The microscope is operating at 300 keV accelerating voltage. The sample contrast comes from the electrons, inelastically scattered from the atomic columns of the particle and detected with the dark-field annular detector [78]. Such method allows an extremely high resolution characterization (0.09 nm) and a possibility to identify crystal structure of subcrystallites within a single nanoparticle, lattice defects and core-shell structures.

Before the microscopy and later every two hours, the sample undergoes an "electron shower" for 30 minutes to eliminate carbon deposition during the measurement. The marker structures can be identified in the microscope allowing unambiguous nanoparticles determination. The orientation of the sample with respect to the marker structures is recorded by acquiring an overview image containing marker structures and nanoparticles.

[2]HAADF-STEM investigations have been produced by Dr. Armand Béché and Prof. Dr. Jo Verbeeck from EMAT, University of Antwerp.

Chapter 4

Direct correlation of microscopic structure and magnetic properties of individual cobalt nanoparticles

In this Chapter, we combine photo-emission electron microscopy (XPEEM) with high-angle annular dark field scanning transmission electron microscopy (HAADF-STEM) to reconstruct the spontaneous magnetization axes of individual cobalt nanoparticles with respect to their atomic structure and structural defects, if present.[1] Anomalous magnetic properties of cobalt nanoparticles have been observed for decades. Such values as magnetic anisotropy, blocking temperature, saturation magnetization and magnetic moment of the particles were reported to be enhanced compared to the bulk values [5, 6, 7, 8, 9]. In particular, the magnetic anisotropy of cobalt nanoparticles has been shown to vary over five orders of magnitude (cf. Table 2.1). Such variation on magnetic properties is often assigned to size, surface effects or internal defects in the nanoparticles. However, there is still is a controversy in explaining the magnetic stability of cobalt clusters with an average diameter of about 10 nm. Typically, the magnetization is determined as an average over a great number of nanoparticles by measuring an overall response of the sys-

[1] Pt markers were deposited by Dr. Elizabeth Müller from the Electron Microscopy Facility at PSI, sample preparation and XPEEM experiments have been done by Dr. Armin Kleibert, Martin Timm and me at the Surface/Interface: Microscopy (SIM) beamline at the SLS of PSI. Data analysis has been done by me. HAADF-STEM investigations have been carried out by Dr. Armand Béché and Prof. Dr. Jo Verbeeck at the EMAT, University of Antwerp. Atomic simulations of the structures have been performed by Dr. Peter M. Derlet from Laboratory for Scientific Computing and Modelling at PSI and myself. Simulations of HAADF-STEM images were performed by Dr. Ivan Lobato from EMAT, University of Antwerp.

tem, for example, in superconducting quantum interference device magnetometry [16], Raman spectroscopy or x-ray magnetic circular dichroism. However, it has already been reported for small Wulff-shaped nanoparticles, that one additional layer on one of the facets greatly increases magnetic anisotropy of the nanoparticle which defines the magnetic energy barrier for magnetization switching [15]. Internal structural defects in the nanocrystals can be a possible origin of high magnetic anisotropy, but their effect is rarely discussed in the literature [11], and it is yet not clear how in detail the different energy contributions interplay. To address the effect of structure on magnetic properties of the particles, these observations strongly suggest that one should correlate the individual structure of the nanoparticle with its magnetic properties rather than to average over the entire ensemble.

In this Chapter, we address the correlation of magnetic and structural properties of individual cobalt nanoparticles. We combine XPEEM to determine magnetic behaviour of individual cobalt particles with HAADF-STEM to probe its crystal structure, crystallographic orientation with respect to the substrate, as well as the shape and structural defects in the particles. Our XPEEM approach allows us to reconstruct the spontaneous magnetization direction of individual nanoparticles in 3D and to directly correlate it with an STEM image of the very same individual nanoparticle.

4.1 XPEEM experiment and magnetization direction reconstruction

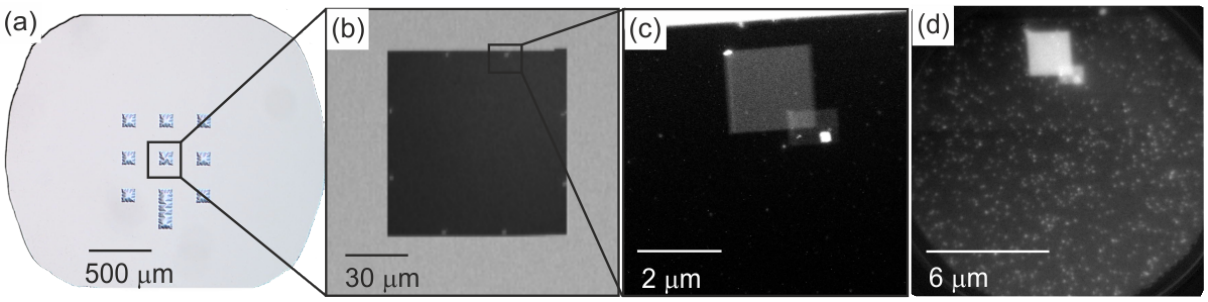

Figure 4.1: (a) Optical microscopy image of a TEM-compatible substrate with nine SiN membranes [66]. (b) SEM image of one of the membranes with Pt marker structures. (c) TEM image of a region of the membrane with a Pt marker structure. (d) Normalized XPEEM image of the region of the membrane with the Pt marker visible in (c) recorded with the photon energy set to the Co L_3 edge at 781 eV. Bright spots correspond to cobalt nanoparticles.

The sample for combined XPEEM and HAADF-STEM characterization was prepared as described in Section 3.1 (cf. Fig. 3.1 "A"). The nanoparticles were deposited at room temperature onto a TEM-compatible substrate with 10 nm thin SiN membranes. An optical microscopy image of the sample on a membrane is presented in Fig. 4.1(a). After nanoparticle deposition, the sample is covered with 1-2 nm of amorphous carbon to avoid oxidation from exposure of the sample to the ambient conditions when transferred to STEM. The sample has Pt markers which ensure an unambiguous identification of the area of interest and individual nanoparticles on it. In Fig. 4.1(b-d) one can identify the marker structures as bright quadrilaterals imaged with SEM [cf. Fig. 4.1(b)], STEM [cf. Fig. 4.1(c)] and XPEEM [cf. Fig. 4.1(d)].

After nanoparticle deposition, the sample was transferred under ultrahigh vacuum conditions to the XPEEM instrument. Then the sample was cooled down to 100 K in order to reach the blocking temperature of some of the particles (increase relaxation time τ_m). A normalized XPEEM image of the sample obtained according to the procedure described in Section 3.2.2 is shown in Fig. 4.1(d). Bright spots correspond to individual nanoparticles. We perform XMCD imaging (cf. Fig. 4.2) to reveal the magnetic contrast of individual nanoparticles as described in Section 3.2.3.

The cobalt nanoparticles used in the particular experiment, have a size distribution between 8 and 25 nm. The performed STEM investigation showed that the particles have a predominantly fcc crystal structure. For a given size distribution of fcc nanoparticles, a single domain assumption can be applied. Therefore, the nanoparticles magnetization can be characterized with $\vec{m}$, uniform for each nanoparticle (as discussed in Chapter 2). As described in Section 3.2.4, nanoparticles in our samples can be divided into three groups depending on their magnetic contrast variation visible with XPEEM magnetic contrast imaging: (i) magnetically blocked with $\tau_m > \tau_x$, (ii) superparamagnetic with $\tau_m < \tau_x$ and (iii) fluctuating with $\tau_m \sim \tau_x$. In this Chapter we will only consider the magnetically blocked nanoparticles case (i) since their magnetic contrast in XPEEM is proportional to the projection of the $\vec{m}$ onto the x-rays propagation direction $\vec{k}$. For the superparamagnetic and fluctuating nanoparticles with $\tau_m \leq \tau_x$ the magnetic contrast is the sum of multiple projections of $\vec{m}$ onto the $\vec{k}$ over the acquisition time and results in zero contrast or reduced contrast, for superparamagnetic and fluctuating nanoparticles, respectively.

The direction of $\vec{m}$ can be reconstructed with a systematic XPEEM investigation according to the procedure described in [71]. To do that, we rotate the sample in plane around its normal z by an angle ϕ_s [cf. Fig. 4.2(a)] to acquire four different magnetic

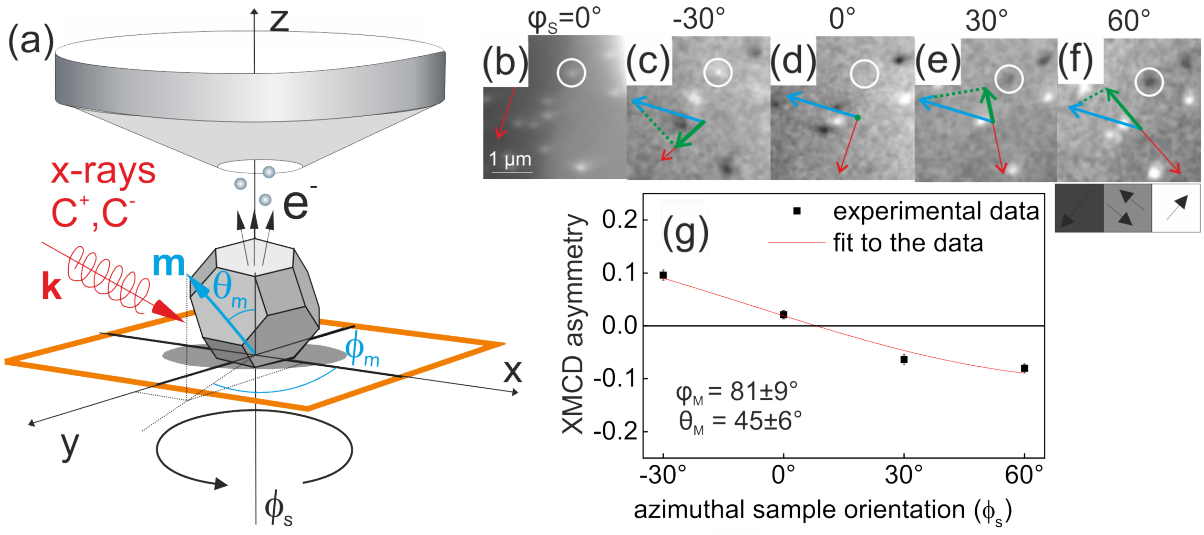

Figure 4.2: (a) Schematics of the experimental geometry. The red arrow shows the x-ray propagation direction $\vec{k}$. The vector $\vec{m}$ represents the spontaneous magnetization direction of the nanoparticle. Probing the sample with circularly polarized x-rays we obtain the XMCD asymmetry A which is given by the product $\vec{m} \cdot \vec{k}$ as explained in Section 3.3. (b) Normalized XPEEM recorded at Co L_3 absorption edge. The x-ray propagation direction $\vec{k}$ is represented by the red arrow. Panels (c)-(f) show the respective magnetic contrast of the same area on the sample at different angles ϕ_s denoted above each image (images are rotated to the same orientation for convenience). Magnetic contrast of the nanoparticle in white circle changes from white to black for respective angles. Magnetization $\vec{m}$ is presented in panels (c)-(f) by the turquoise arrow. There red and green arrows represent $\vec{k}$ and the component of $\vec{m}$ on $\vec{k}$, respectively. The inset with arrows depicts magnetic contrast variation depending on the in-plane magnetization orientation.(g) Asymmetry A as a function of ϕ_s fitted according to the procedure described in [71].

contrast maps of the very same field of view. The XMCD asymmetry A derived from the XPEEM data is proportional to the projection of $\vec{m}$ on the x-ray propagation vector $\vec{k}$ (cf. Section 3.2.3). For fcc cobalt thin films, the maximal absolute value of XMCD of 0.24 has been found [79]. For our experiments, the asymmetry value can vary in an interval (-0.24; 0.24) according to the respective $\vec{m}$ and $\vec{k}$ orientations. With our data, we are able to reveal angles ϕ_m and θ_m of the magnetization vector [cf. Fig. 4.2(a)]. An example of such data is plotted in Fig. 4.2(g) for one particle at ϕ_s equal to -30°, 0°, 30°, 60°. There, ϕ_m=81±9° and θ_m=45±6°.

In Fig. 4.2, the panel (b) shows a normalized XPEEM image of the same region of the sample. The x-ray propagation direction $\vec{k}$ is represented by the red arrow in each

panel. The respective magnetic contrast maps of the investigated area at different angles ϕ_s are given in panels (c)-(f), the corresponding angles ϕ_s are denoted above each image (images are rotated to the same orientation for convenience). The magnetic contrast of the nanoparticle highlighted with a white circle changes upon sample rotation. Initially white, it gradually becomes grey and then black at ϕ_s=60°. The magnetization $\vec{m}$ is presented schematically in the insets by a turquoise arrow. The green arrow represents a component of $\vec{m}$ on the $\vec{k}$ direction, $\vec{m}_k$. The dashed lines are used as guides to the eye between the tip of $\vec{m}$ and its component $\vec{m}_k$. The panels in Fig. 4.2(b)-(f) show only a fraction of the field of view recorded with XPEEM. A full field of view is depicted in Fig. 4.1(d) and contains about 500 nanoparticles. Using the described method, we have reconstructed spontaneous magnetization direction of more then 200 magnetically blocked nanoparticles. The data is later used to plot the magnetization vector of the magnetically blocked nanoparticles onto the STEM images. After the XPEEM experiment, the sample was covered with an additional protection layer of amorphous carbon, extracted from ultrahigh vacuum and transferred to the transmission electron microscope in Antwerp. We have pre-identified magnetically blocked nanoparticles and superparamagnetic ones so that both types could be imaged with STEM. The microscopists have selected 40 nanoparticles: 18 superparamagnetic and 22 magnetically blocked. The results of the microscopy and the correlation with XPEEM data are shown below.

4.2 HAADF-STEM results

The experimental details for HAADF-STEM are described in Chapter 3. HAADF-STEM is capable of resolving individual atomic planes and columns of crystalline nanoparticles. The resulting images are presented in Figs. 4.3, 4.4 and 4.5 for superparamagnetic, magnetically blocked and large (diameter more then 18 nm at least in one direction) nanoparticles, respectively. The overall STEM investigation revealed a size distribution of the particles between 8 and 25 nm with average 13.1±2.0 nm. The aspect ratio of the particles (except few agglomerates shown in Fig. 4.5) was below 1.1, indicating low shape anisotropy. We have mentioned in Section 3.2.4 that the magnetically blocked particles have an energy barrier of at least 0.63 eV since their magnetic moment is stable over the measurement time τ_x. It has been estimated that for cobalt nanoparticles of a diameter of 12 nm and fcc crystal structure an aspect ratio of at least 1.17 is needed to overcome the magnetic energy barrier and reach magnetically blocked state at room temperature [11]. These considerations suggest that an additional source of magnetic

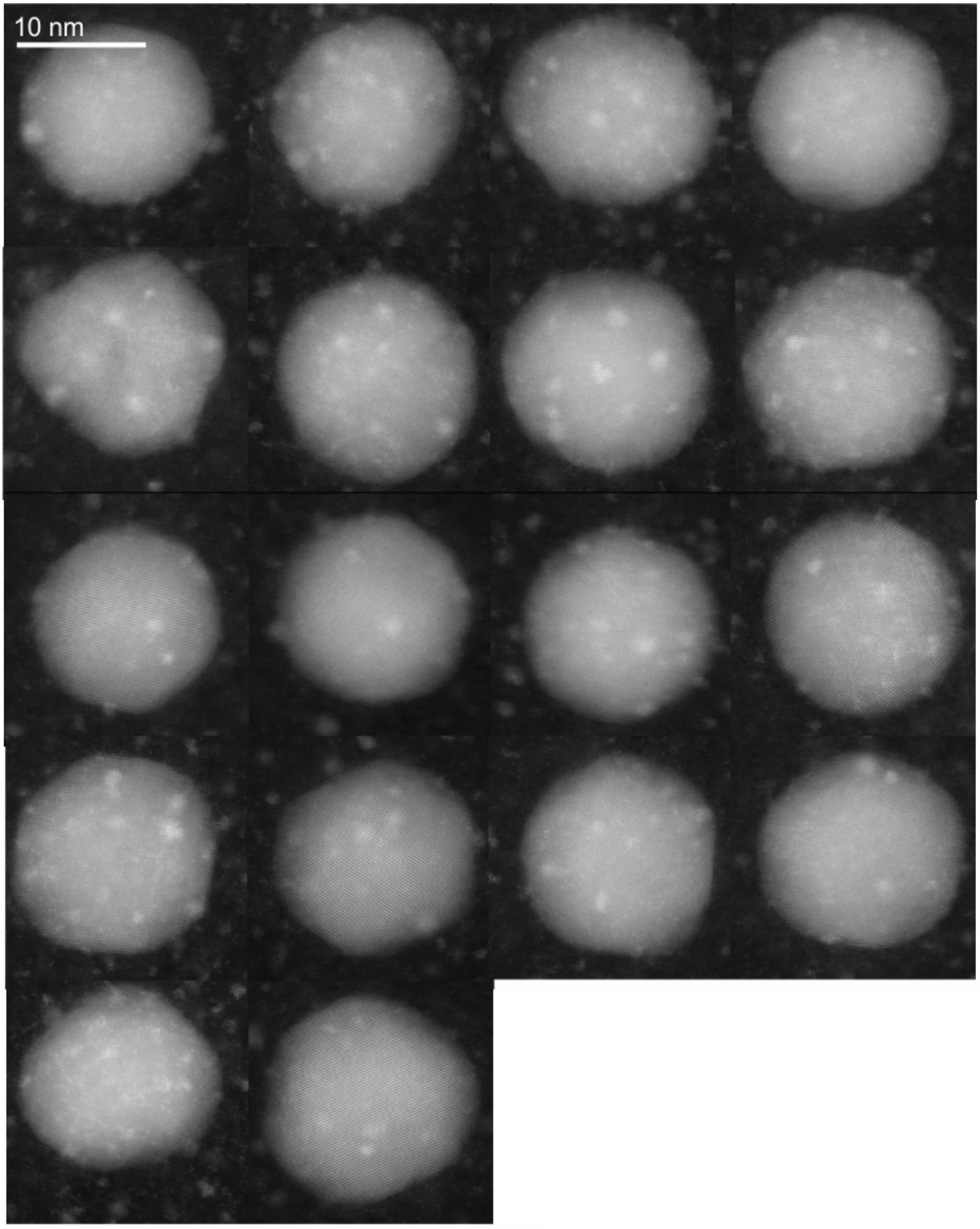

Figure 4.3: HAADF-STEM images of superparamagnetic cobalt nanoparticles.

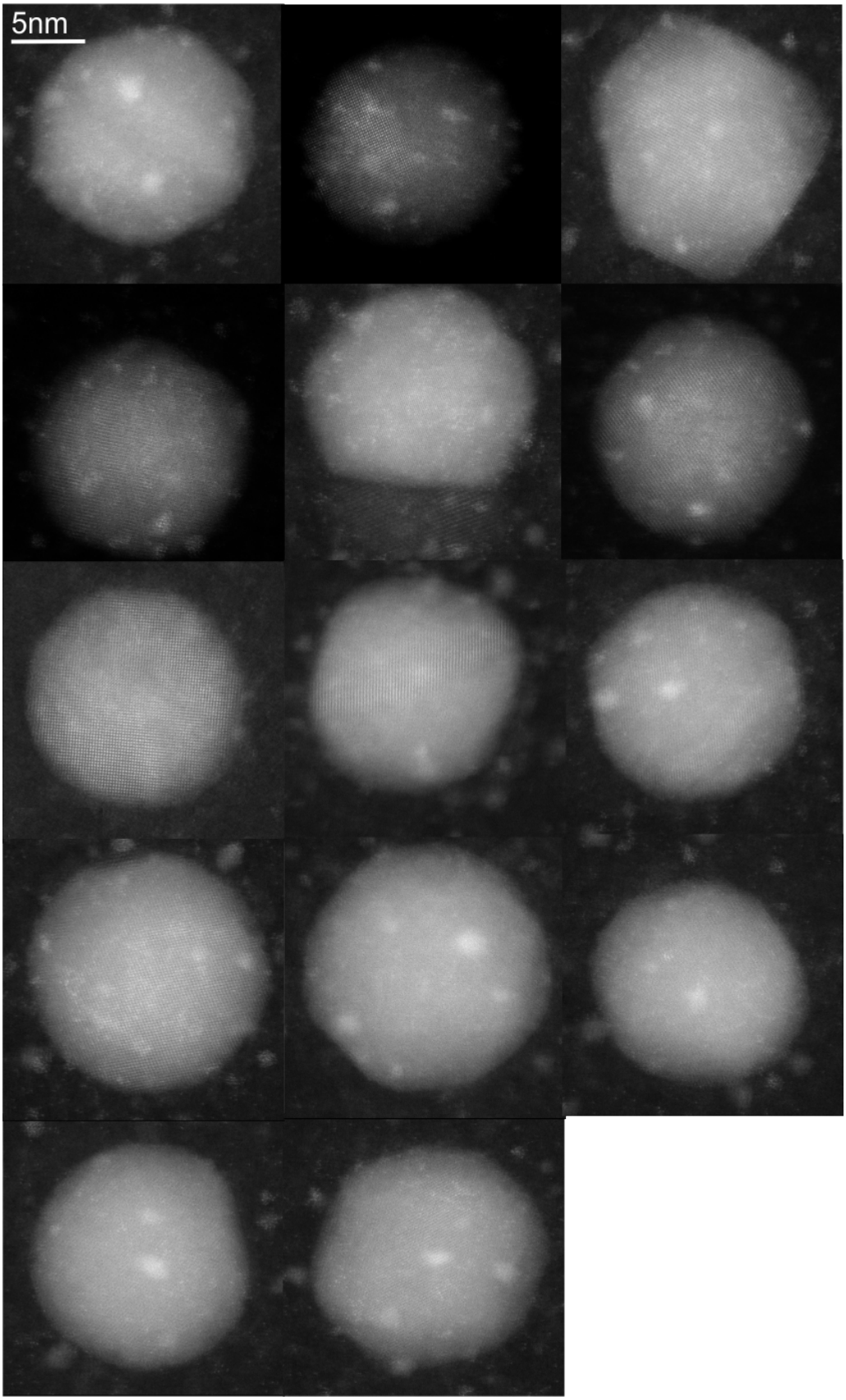

Figure 4.4: HAADF-STEM images of magnetically blocked cobalt nanoparticles.

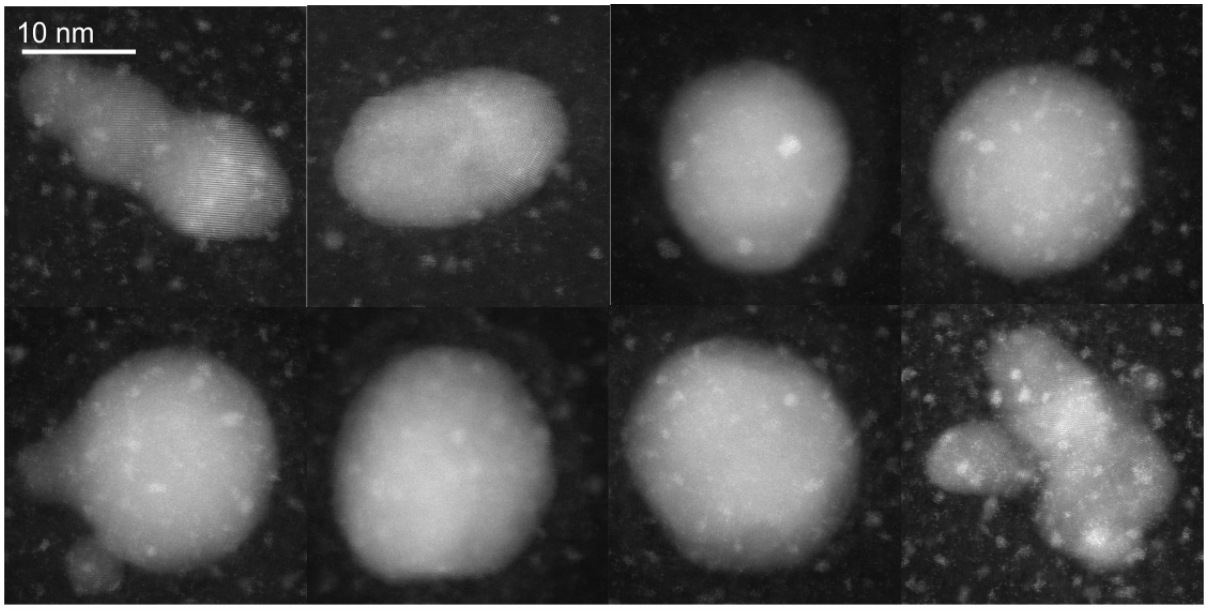

Figure 4.5: HAADF-STEM images of large (those with at least one dimension longer than 18 nm) magnetically blocked cobalt nanoparticles.

anisotropy might exist, namely, internal structural defects as was discussed in Ref. [11]. From the STEM imaging it is visible that a large fraction of nanoparticles consist of multiple grains and contain defects, but a precise characterization of the defects nature and positions is not possible. Therefore, a detailed investigation of the structure of the nanoparticles is required. HAADF-STEM technique allows one to reveal atomic columns and planes (not always visible) and therefore to determine the crystalline structure of individual nanoparticles. The methodology will be explained later in Section 4.2.2.

4.2.1 Correlation of HAADF-STEM and XPEEM results

We can not only address the crystal structure of individual nanoparticles, but also draw the spontaneous magnetization direction of individual nanoparticles on the HAADF-STEM image with respect to their crystal structure. This combination yields unprecedented insight into the magnetism of cobalt nanoparticles. The reconstruction of magnetization direction plotted onto STEM images is shown in Fig. 4.6. There, with turquoise arrows, the in-plane component of $\vec{m}$ is depicted directly onto the STEM images. Next to the STEM images the insets show the direction of out-of-plane $\vec{m}$ component (m_{OOP}). White squares in STEM images highlight atomic planes or columns and are enlarged in panels next to the STEM images. We have plotted the magnetization for the magnetically blocked nanoparticles. Among all of the investigated nanoparticles, it was not possible

to find any trend in the magnetization direction with respect to the crystal structure. Therefore, we payed more attention to the structure of the nanoparticles.

4.2.2 Crystal structure determination with 3D STEM

In fact, the information derived with standard 2D TEM technique does not allow a straightforward interpretation of the experimental data. For that, more than one STEM image of the particle is needed. The crystal structure can be unambiguously determined only by matching of interatomic plane distances acquired from different projections of the particle. Such parameters as atomic structure, morphology, occurrence of the surface facets and structural defects can be only confirmed with the 3D STEM technique. The STEM sample holder has two degrees of freedom that allow tilting the sample in a relatively large solid angle of 0.8-0.98 sr (steradian) and reveal quantitative information along the viewing direction of STEM. Images of such holders are presented in Fig. 4.7. 3D STEM imaging can reveal the hidden shape and structural features. The tilting/rotation data is recorded together with the STEM images and is used later to confirm that the particles have a specific crystal structure.

In order to determine the crystal structure of the particle, several STEM images are recorded for different sample holder orientations. An example of such procedure is shown in Fig. 4.8. The nanoparticle was observed from four directions sketched in Fig. 4.8(e): A (α=0°, β=-4.19°) [cf. Fig. 4.8(a)], B (α=0°, β=-39.79°) [cf. Fig. 4.8(b)], C (α=0°, β=40.53°) [cf. Fig. 4.8(c)] and D (α=45°, β=40.1°) [cf. Fig. 4.8(d)]. The imaging directions are decided based on the lattice fringes visibility, each image should contain atomic columns or planes. Then, for each image, a fast Fourier transformation (FFT) is taken (not shown) to observe a "diffraction pattern" from the image and to determine the crystal orientation assuming fcc or hcp symmetry in our case. The determined "theoretical" points are then plotted onto the so-called polar map [cf. pink squares in Figs. 4.8(f),(g)], and compared to the measured results denoted with yellow squares in Figs. 4.8(f) and (g). The plotted values are compared and the most matching crystal lattice is then determined. The particle shown in Fig. 4.8 has fcc crystal structure. From the 2D investigations of the particles shown in Figs. 4.3, 4.4 and 4.5, we concluded that 37 out of 40 particles have fcc structure and 3 have hcp but the results must be proven by 3D STEM investigation. We have determined the crystal structures for five nanoparticles using 3D STEM approach: three of them have fcc crystal structure and two of them are hcp (not shown). 3D STEM reveal the presence of defects: multiple grains with fcc and hcp structure in some particles and layers in some of the nanoparticles (not shown). The

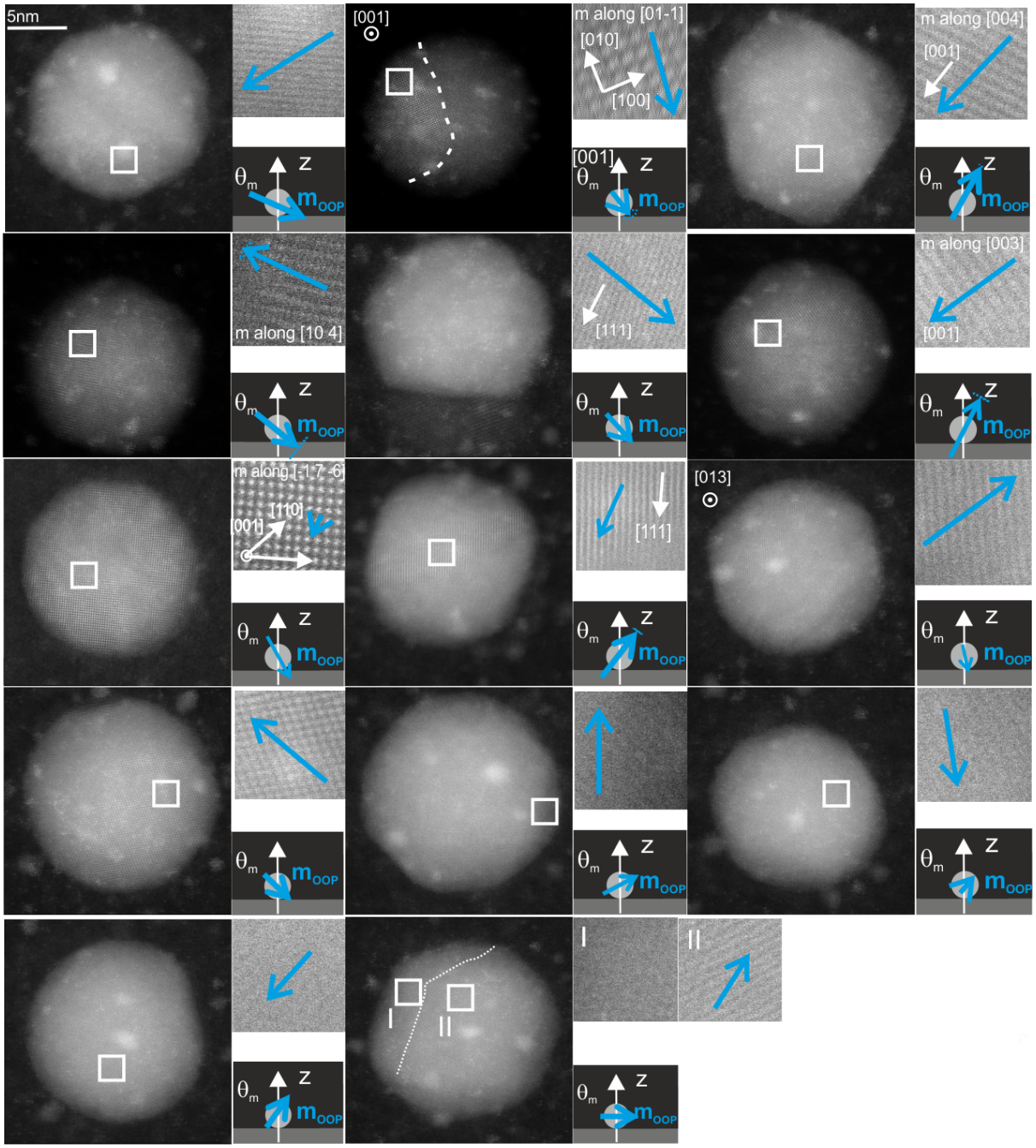

Figure 4.6: Magnetization direction reconstruction on HAADF-STEM images of magnetically blocked cobalt nanoparticles.

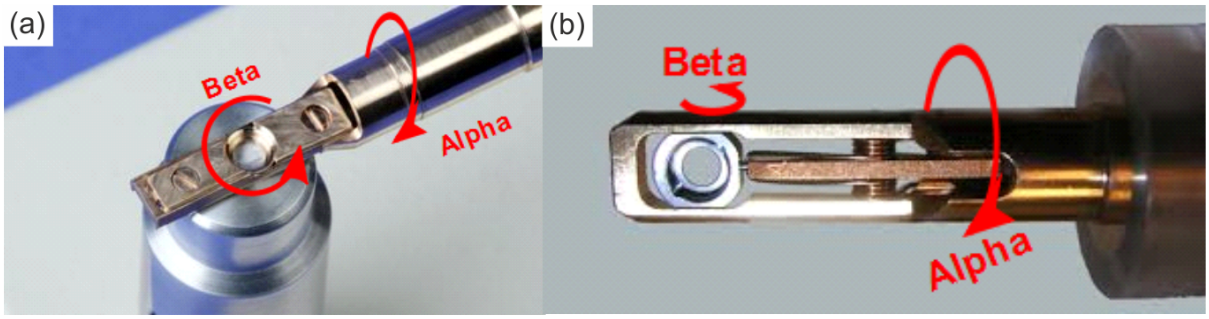

Figure 4.7: TEM sample holder imaged made by Dr. A. Béché. (a) A special tomography rotation tilt holder. Alpha angle is the standard rotation around the axis of the sample holder and the beta angle is a rotation of the entire sample cup.(b) A standard double tilt holder.

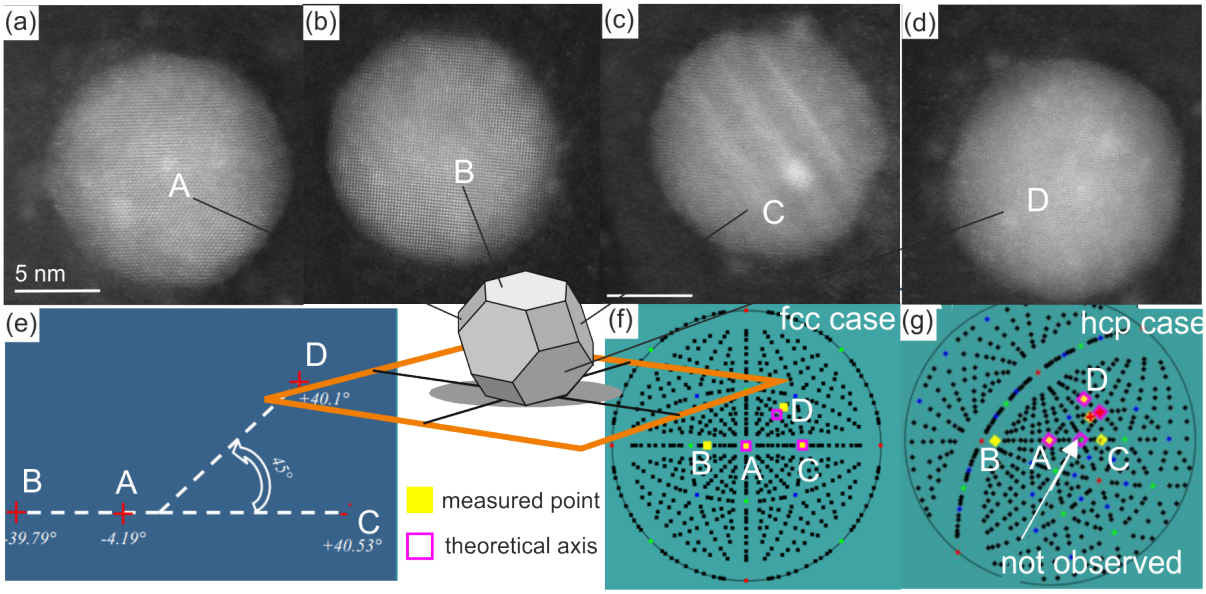

Figure 4.8: 3D STEM imaging of one nanoparticle from four different directions using the sample holder from Fig. 4.7(a): (a) A (α=0°, β=-4.19°) (b) B (α=0°, β=-39.79°) (c) C (α=0°, β=40.53°) (d) D (α=45°, β=40.1°) (e) Schematic drawing depicting how the projections are aligned in sample holder coordinates (f) polar maps depicting the measurement points (yellow squares) and theoretical points (pink squares) derived for the case of fcc crystal, (g) respective polar map for hcp crystal.

combination of XPEEM and HAADF-STEM gives an immence amount of information about a single nanoparticle. We will focus next on two of the particles and use the derived results for nanoparticle models, STEM images simulations and magnetic properties discussion. These particles serve good examples of (i) elongated nanoparticles and (ii) spherical nanoparticles with blocked magnetization.

Nanoparticle with strong shape anisotropy

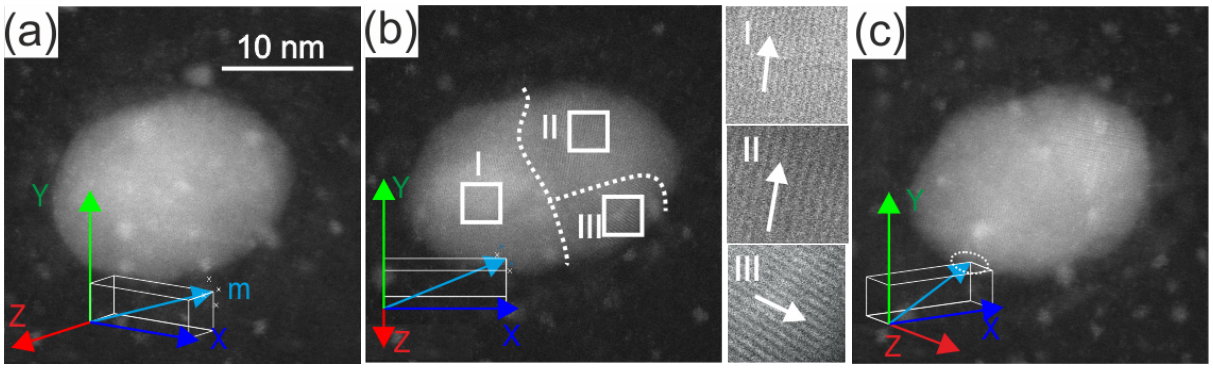

Figure 4.9: HAADF-STEM images of an elongated fcc cobalt nanoparticle. The orthogonal coordinate system is represented in the images with red, green and blue arrows. Panels (a), (b) and (c) present STEM images of the very same particle taken from different sample tilt angles around Y axis (green arrow). The turquoise arrow in the coordinate system represents magnetization direction of the particle reconstructed from XPEEM data and plotted directly to the STEM image. The magnetic moment of the nanoparticle is oriented along the long axis of the nanoparticle as predicted from the shape anisotropy considerations. Insets I, II and III show three different atomic planes in of the nanoparticle visible in the STEM.

The first example is an elongated nanoparticle with a strong shape anisotropy. It is expected, that the magnetic moment will orient along the long axis of the nanoparticle due to the shape anisotropy. 3D STEM investigation revealed the fcc structure of the nanoparticle by using the procedure described in Section 4.2.2. The HAADF-STEM image of the particle, taken from different directions, is presented in Fig. 4.9. Here on panel (b) the image is taken in the STEM geometry; panel (a) was acquired with the sample holder tilted around α (cf. Fig. 4.7) to 30° and to acquire panel (c) the sample holder was tilted to −30°. A coordinate system is presented in the Figures for better understanding of the imaging directions. The angle α rotates the sample around Y axis (cf. coordinate system in Fig. 4.9). The turquoise arrow shows the $\vec{m}$ direction

reconstructed from XPEEM measurements.

A detailed inspection of the HAADF-STEM data reveals that this particle is not mono-crystalline, but consists of at least three grains with individual crystallographic orientations. The dashed lines in Fig. 4.9 highlight the polycrystalline nature of the particle. Such structural effects may locally perturbate the electronic structure and/or cause sizable local strain and, thus, strongly affect the magnetic properties. However, in this particular case, a structurally highly defective nanoparticle has its magnetization direction defined by shape anisotropy. The observed results suggest that the shape anisotropy is dominating over the other possible magnetic energy contributions caused by local spin inhomogeneity, which could lead to spin reorientation. If we look at an almost spherical nanoparticle, we can neglect the shape anisotropy contribution. Thus, other components of magnetic anisotropy might play a more predominant role in defining the magnetization direction of the nanoparticle.

Spherical nanoparticle

The case of a spherical nanoparticle is presented here. The HAADF-STEM data together with their FFTs [cf. insets in Fig. 4.10] reveal the fcc structure of this particle according to the procedure described in Section 4.2.2. The coordinate system on each panel indicates the [100], [010] and [001] crystallographic directions and serves to visualize the different orientations of the particle. The respective [100]-directions are denoted by the colored arrows. The magnetization direction was determined from XPEEM data and is represented in Fig. 4.10 with a turquoise arrow. The data suggest that the magnetization direction is parallel to the [001]-direction within the error bar denoted with a dashed oval. This could suggest a dominant surface anisotropy contribution which prefers the magnetization to be oriented along the [001]-directions, as explained in [11].

The projection (b) in Fig. 4.10 reveals the stacking faults present in the particle, highlighted with the dashed lines. The three stacking faults are not clearly visible in panels (a), (c) and (d). The extended data set confirmed also that the nanoparticle is nearly spherical (72±1 atomic planes along 100 directions), with 12.8 nm diameter.

4.3 Discussion

In the above experiments, we have combined a magnetic characterization of individual nanoparticles with XPEEM and structural characterization with HAADF-STEM. The complementary data set enabled an unambiguous determination of the direction of mag-

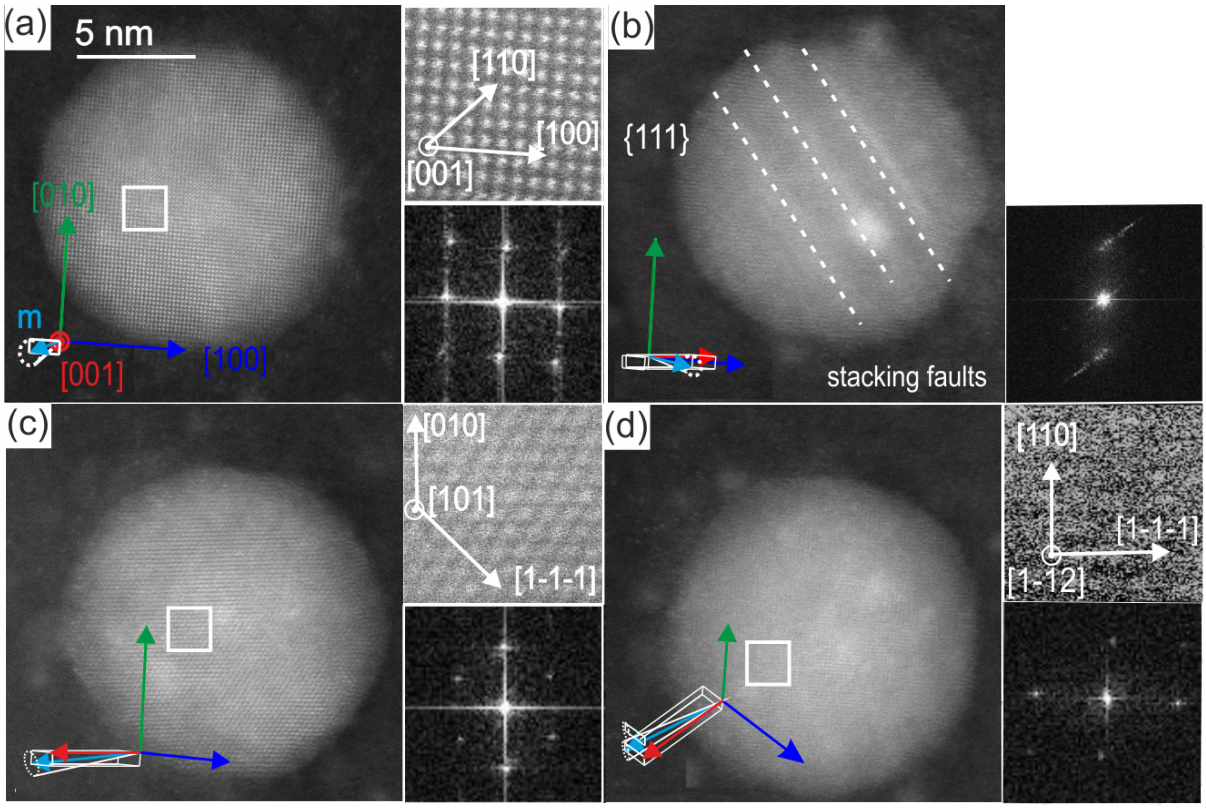

Figure 4.10: HAADF-STEM images of a spherical fcc cobalt nanoparticle. The respective [100]-directions are denoted in the STEM image by the colored arrows. The magnetization direction was determined from XPEEM data and is represented with the turquoise arrow. (a) represents a view on the nanoparticle along [001] direction. The crystall structure with atomic columns along the respective [001] directions is visible in this image and a fraction of the image in white square is enlarged in the inset on the right of (a), an inset below shows FFT transformation of the image with respective peaks corresponding to (220), (200) etc. respective diffraction peaks. (b) View on the very same nanoparticle as in (a) from α=0°, β=-39.79°, as described in Fig. 4.8. STEM data in panel (b) reveals stacking faults highlighted by dashed lines. (c) Another image of the very same particle at α=0°, β=40.53°. (d) Projection of the very same particle α=45°, β=40.1°.

netization of magnetically blocked nanoparticles with respect to their crystal lattice. The results revealed a complex crystal structure of nanoparticles including the presence of fcc and hcp phases, polycrystalline single particles, and the presence of defects. The magnetization of the magnetically blocked nanoparticles does not follow a specific crystal direction, particularly, the <111> easy axis of bulk fcc cobalt, but can have an almost arbitrary orientation with respect to the crystal lattice. At the same time, there is a large number of nanoparticles of similar size existing in the superparamagnetic state (cf. Fig. 4.3). Moreover, within the narrow size distribution, two crystal structures (fcc and hcp) of the particles were found. Our observations suggest that the magnetic stability as well as the direction of the magnetization in the particles are not defined by the size but depends significantly on the internal structure of individual nanoparticle. In this Chapter we have shown that an almost spherical fcc nanoparticle with stacking faults is magnetically blocked which indicates that such defects are crucial for the stabilization of the magnetization and affect magnetic energy barrier, since fcc cobalt nanoparticles are expected to be superparamagnetic at 12 nm diameter as discussed in Section 2.1.2. The staking faults correspond to the perturbation in the local atomic structure, which may affect the spin arrangement in the particle, for example via magnetoelastic coupling. In particular, the stacking faults introduce hcp planes in the fcc structure (cf. Section 2.1.1). To learn more about their effect of the nanoparticle stability, we have developed models of fcc nanoparticle with planar defects.

4.3.1 Atomic nanoparticles models

In order to confirm that the lines visible in Fig. 4.10(b) are the stacking faults and their positions in the particle shown in Fig. 4.10, we made a model of the atomic structure of nanoparticle containing stacking faults (cf. Section 2.1.1). 3D STEM imaging revealed that the nanoparticle was almost spherical, contained 72±1 planes along each respective [100] direction. The diameter of the particle was 12.8 nm. From Fig. 4.10(b) one can estimate that there are three staking faults in the particle, one is situated on the equator of the particle and two more are symmetrically placed within 13 atomic planes from the central one.

The modelling of the atomic structure of the nanoparticle was performed using Matlab. The code was written by Peter M. Derlet in Fortran and then modified for Matlab by myself. In our model, we used 72 (100) planes in each of three directions and spherical shape of the nanoparticle. The fcc cobalt crystal lattice constant l_c=3.5642 Å was used [80]. The crystal structure was built up along the [111] direction by repetition of (111)

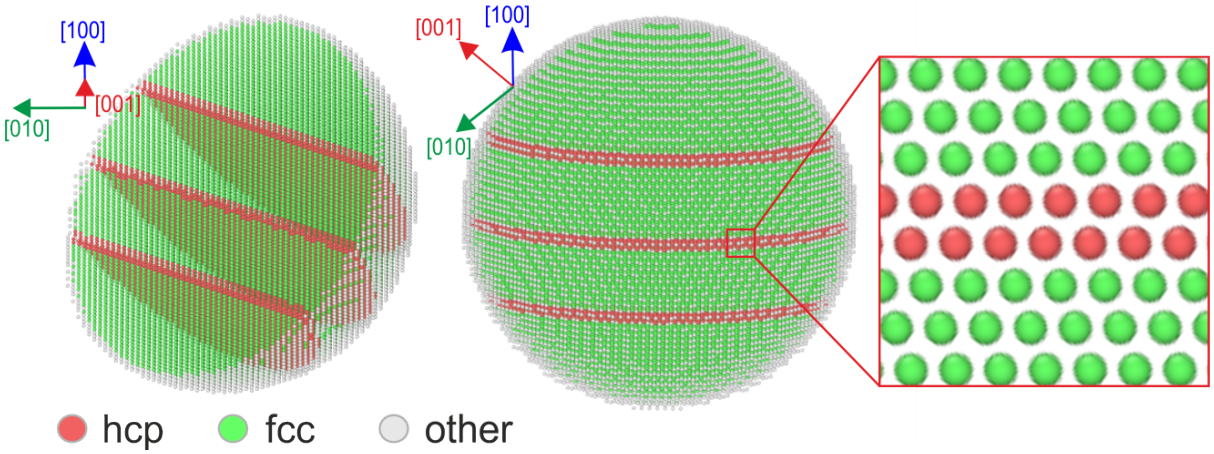

Figure 4.11: Model of a spherical nanoparticle with three stacking faults. The size of the nanoparticle is 12.8 nm, the model contains 72 (111) atomic planes and 97755 atoms. Each stacking fault is represented with red spheres which form local hcp order in the green fcc structure. White spheres indicate surface atoms with low coordination.

planes and cut as a sphere with a diameter of 12.8 nm around the coordinate center. Stacking faults were introduced to the fcc crystal along one of [111] directions by skipping one of the (111) planes (ABCAC, cf. Section 2.1.1): one at the equator and two more 13 atomic planes apart from the equator (cf. Fig. 4.11). Each stacking fault is represented with red spheres (atoms) which form hcp structure in green fcc structure. The white spheres indicate surface atoms with low coordination which cannot be assigned to either fcc or hcp structure. The final model contains 72 (100) atomic planes and 97755 atoms.

The cohesive energy of the modelled structures was then minimized using LAAMPS molecular dynamics package [81]. The total system energy minimization was done using the fcc cobalt potential from Ref. [82]. The introduced stacking faults were not perturbed by the minimization, which indicate their stability at least within the relaxation time. The relaxed atomistic model was then used to simulate the results of HAADF-STEM images (cf. Section 4.3.2).

We have created more models of spherical nanoparticles with different number of hcp planes in the fcc particles and also minimized the total interatom pair-interactions with LAMMPS. A full Table of simulated nanoparticles can be found in Tab. 4.1. The diameter of each nanoparticle is 12.8 nm, the number of stacking faults is described in the column "Type" of the Table, the positions of the stacking faults are stated in the column "hcp layer position", the total number of atoms as well as hcp and fcc atoms separately, is stated in the respective columns. The models are plotted in Fig. 4.12.

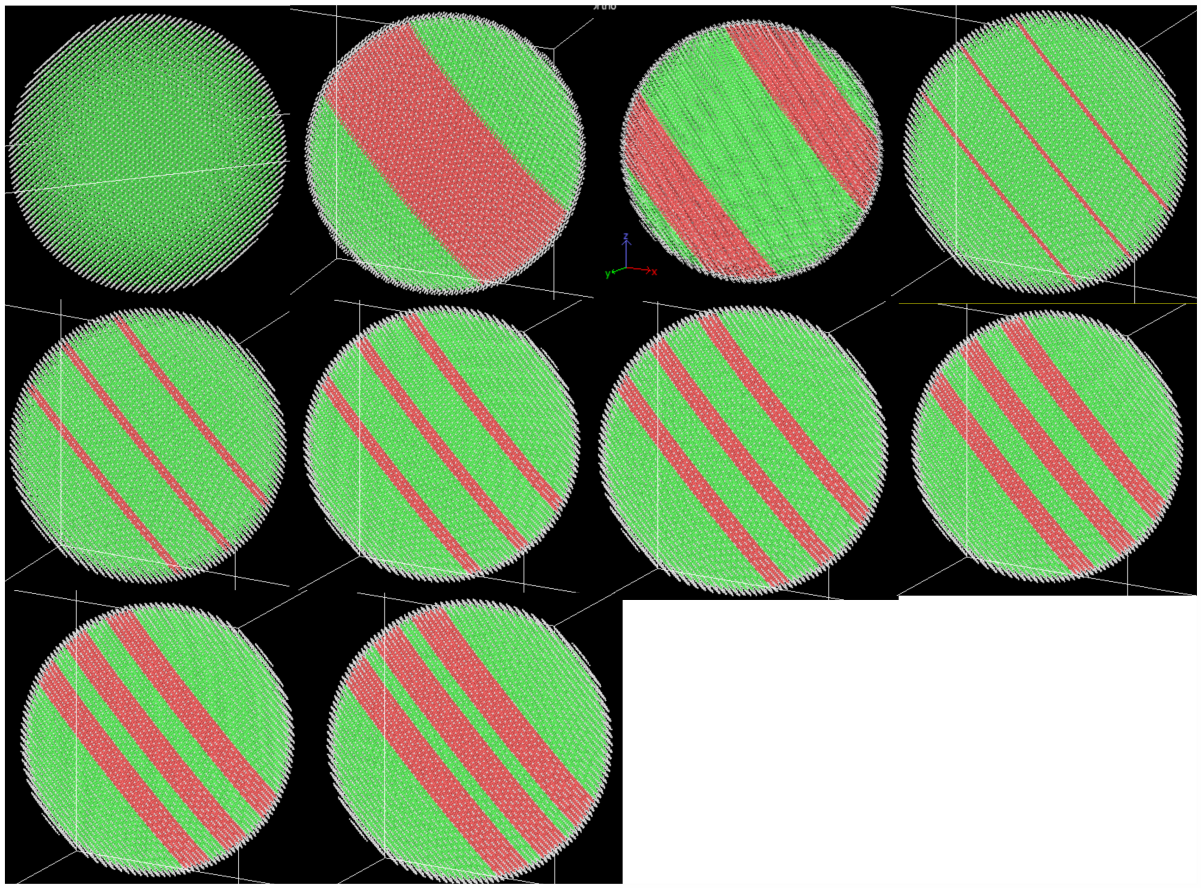

Figure 4.12: Nanoparticles models denoted in Tab. 4.1 relaxed with LAAMPS.

4.3.2 HAADF-STEM simulations

In order to test our hypothesis about the stacking faults and to prove the position of the stacking faults in the spherical nanoparticle, we simulated HAADF-STEM images based on our model. Knowing the orientation from which each image in Fig. 4.10 was taken, we have rotated the simulated nanoparticle respectively and performed a HAADF-STEM image simulation for all four projections. For that, frozen phonons calculation has been carried out by Ivan Lobato from EMAT, University of Antwerp [83, 84]. The calculation involves atomistic model of the nanoparticle relaxed with LAAMPS described in the previous section. For the simulations, 300 keV acceleration voltage, source spread function 0.45 A and an ideal detector with 50 mrad and 165 mrad inner and outer diameters, respectively, were used. The FFT insets to the panels in Fig. 4.13 are in agreement with respective experimental FFTs in Fig. 4.10, confirming that our models and directions of imaging have been determined correctly.

Model name	Type	Pos.$_{hcp}$	N$_{tot}$	N$_{fcc}$	N$_{hcp}$
Ideal	Spherical fcc	-	97773	87602	0
1stack25layers	wide hcp layer in the middle	0	97758	36204	51384
_2stack_2layers	Two symmetrical hcp layers	-12; 12	97723	54211	33330
_3×1_stf	3 single stacking faults	-13; 0; 13	97761	81830	5749
_3×2_stf	3 double stacking faults	-13; 0; 13	97755	75984	11594
_3×3_stf_mdyn	3 triple stacking faults	-13; 0; 13	97780	70056	17548
_3×4_stf_mdyn	3 × 4 stacking faults	-13; 0; 13	97758	63970	23616
_3×5_st_mdyn	3 × 5 stacking faults	-13; 0; 13	97763	57832	29749
_3×6_stf_mdyn	3 × 6 stacking faults	-13; 0; 13	97761	51605	35982
_3×7_stf_mdyn	3 × 7 stacking faults	-13; 0; 13	97740	45314	42256

Table 4.1: Atomic models of fcc cobalt nanoparticles with a different number of stacking faults (cf. column "Type"). The position of stacking faults is denoted on column Pos.$_{hcp}$, number of atoms in total, as well as hcp and fcc atoms denoted in columns N$_{tot}$, N$_{fcc}$, N$_{hcp}$, respectively.

4.3.3 Structural stability of fcc cobalt nanoparticle with planar defects

Upon relaxation, the total cohesive energy of the particles was determined. All of the simulated models have the same diameter of 12.8 nm and contain about 97700 atoms. The main difference between the models is the number of stacking faults introduced into the fcc structure. In Fig. 4.14 the cohesive energy per atom is presented as a function of number of hcp atoms in the particle. In fact, a totally hcp crystal has a lower energy than a totally fcc one. Nevertheless, most of our particles have fcc structure.

One possible explanation is that small magnetic clusters undergo a phase transformation and stabilize in crystal phases different from the bulk specimens [41]. The fcc structure for cobalt is expected for temperatures higher than room temperature, and the existence of fcc structures at room temperature is attributed to fast cooling in the growth process. Small clusters are also expected to exist in ideal polyhedral shapes because the surface facet energy stabilizes the nanoparticle [41]. However, our observations show that the variety of shapes and structural defects in the nanoparticles is much broader. Moreover, most of the reported nanoparticles have almost spherical shape and only few

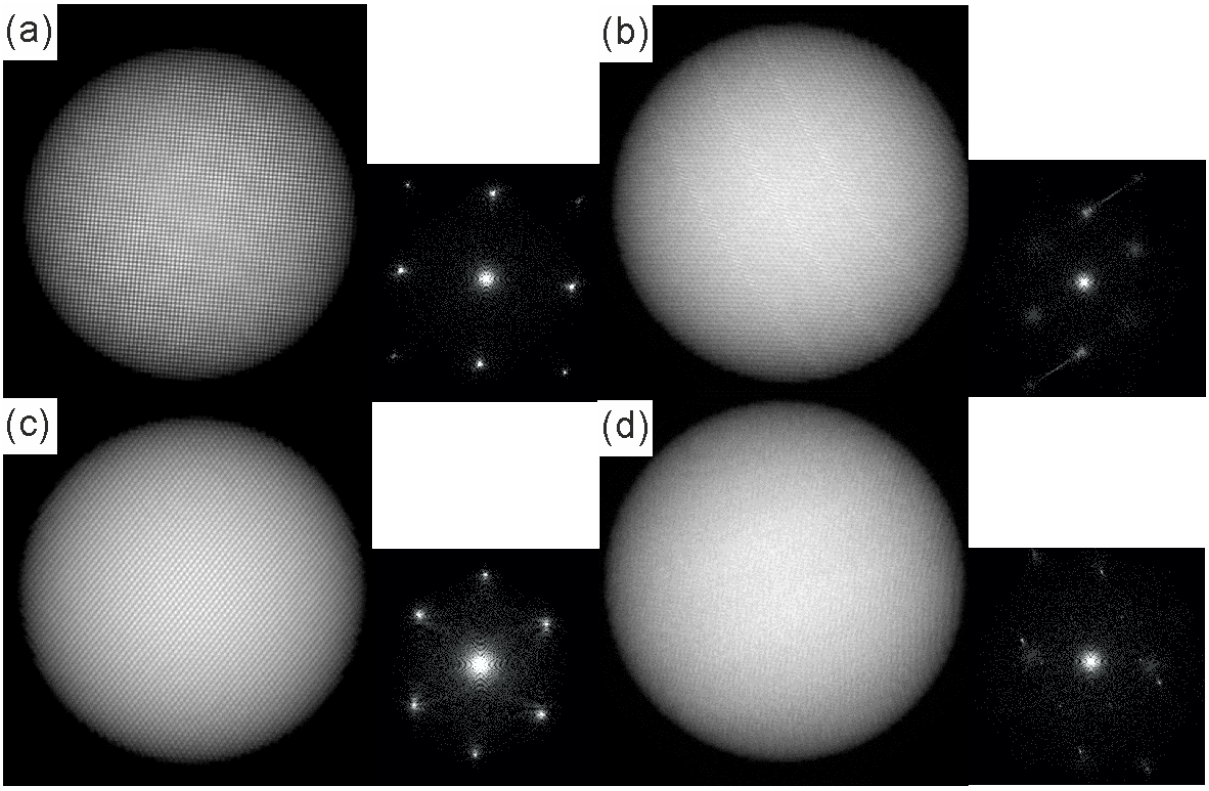

Figure 4.13: Simulated HAADF-STEM images of the nanoparticle model with stacking faults.

of them have strongly expressed surface facets.

4.3.4 Magnetic anisotropy of cobalt nanoparticles

The stability of magnetic moment in individual particle is a challenging topic. The magnetic energy barrier which determines the stability of the nanoparticle according to the Arrhenius law is a complex term, consisting of magnetocrystalline, shape, and surface anisotropy. An example of an almost spherical particle with a stable magnetic moment is shown in Fig. 4.10, illustrating that apart from shape and magnetocrystalline contribution, surface anisotropy may be significantly large and can govern the stability of the magnetization. But also the internal structural defects have to be taken into account. The existence of an hcp layer in an fcc crystal might locally affect the spin configuration due to the local changes in the bond lengths, resulting in magnetic anisotropy different from an ideal fcc crystal. It has been shown that stacking faults in bulk hcp cobalt reduce the magnetocrystalline anisotropy energy of the material in general and this deviations may be observed up to 15 atomic layers from the stacking fault [55]. Similar results for nanosized fcc cobalt would be very interesting. Unfortunately, the magnitude of

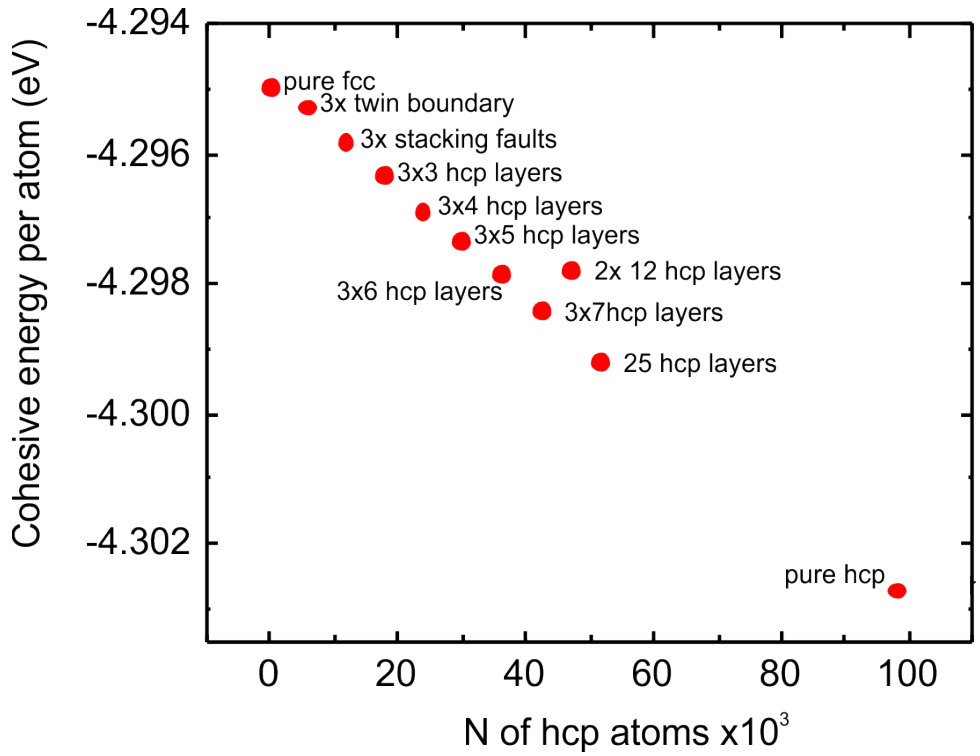

Figure 4.14: Cohesive energy of the particles models from 4.1 per atom as a function of the number of hcp atoms in the particle.

the anisotropy caused by the defects is unclear. This work would greatly benefit from calculation of the magnetic anisotropy using Néel-pair anisotropy model and employing the distance dependence of Néel constant:

$$E = L(\vec{e}_m \cdot \vec{e}); \tag{4.1}$$

$$L(r) = L(r_0) + [\frac{dL}{dr} \cdot r_0]\eta, \tag{4.2}$$

where $\vec{e}_m$ is a unit vector pointing along the direction of magnetization, $\vec{e}$ is an interatomic vector, L - is Néel constant and η is the atomic displacement [38]. These terms may come in play at hcp - fcc interface where the local symmetry is broken and some bonds are contracted whereas some are stretched. The results of such calculations might help us to understand how the inclusion of hcp planes affects the spontaneous magnetization direction and the structural stability of a spherical cobalt nanoparticle. However, without *ab initio* calculations it is not possible to determine whether the stacking faults act as a source of extra magnetic anisotropy in the system.

4.4 Conclusions

We perform magnetic and atomic resolution structural characterization of cobalt nanoparticles with size ranging between 8 and 25 nm (mean diameter 13±2 nm). Using XPEEM we determine the orientation of the magnetization at 100 K for more than 200 nanoparticles. Our structural investigations reveal that most of the particles have fcc crystal structure and nearly spherical shape. In addition, many of the particles have defects which can modify the magnetic anisotropy. For single crystalline, spherical cobalt nanoparticles with fcc structure in the present size range a superparamagnetic behavior is expected. However, contrary to this, half of the particles are magnetically blocked irrespective of the size of the nanoparticles, which suggests a significant magnetic energy barriers enhancement.

The orientation of the magnetization of the nanoparticles is not correlated with the crystal structure of the particles. Together with the observed structural defects this suggests a significant impact of defects not only on the magnetic energy barriers, but also on the orientation of the spontaneous magnetization axes of the nanoparticle.

3D STEM studies are performed for five of the particles and reveal the presence of multiple grains with fcc and hcp structure in some particles or layers in some of the nanoparticles. For one elongated nanoparticle consisting of several grains we find that shape anisotropy dominates over other contributions to the magnetic anisotropy, and therefore the magnetization of this particle is aligned parallel to the long axis. An other spherical particle contains three stacking faults not visible initially. In order to identify the nature of the defects we developed atomistic models for STEM simulations, which we compared to the experimental STEM data. Using this approach we could confirm the presence of the stacking faults and their orientation in the nanoparticle. Our simulation shows that the stacking faults are oriented parallel to (111) planes of the nanoparticle. In the same time, the magnetization of the nanoparticle we find to point along the [001] axis, which deviates from the easy axis known for the bulk fcc cobalt. In order to prove whether this deviation is due to the presence of the staking faults, a theoretical approach for calculating the magnetic properties of nanoparticles including structural defects is currently being developed.

Chapter 5

In situ oxidation of cobalt nanoparticles

In this Chapter, we investigate the effect of controlled *in situ* oxidation on the structural and magnetic properties of cobalt nanoparticles from the early stage of oxide formation.[1] Understanding the oxidation of metallic nanoparticles is important for producing nanoparticles for heterogeneous catalysts, biomedicine and electronics [85, 86, 87]. Particularly, it is important to understand the room temperature oxidation kinetics of cobalt and how the oxidation affects the magnetic properties of the nanoparticles since the surface atoms consitute a large fraction of the volume of the particles with average diameters below 20 nm. It has been reported that cobalt nanoparticles form Co/CoO core/shell structures upon exposure to ambient air conditions [63]. Others report on fully oxidized nanoparticles with Co_3O_4 stucture [27]. Sometimes the atoms of the particles completely diffuse out to the shell resulting in hollow oxide particles [88]. Still, the stabilization mechanism of shell growth is not well understood. One of the possible reasons could be stabilization of the surface with a metastable wurtzite phase [26]. However, such studies focus on rather long-term effects, whereas the initial stages of oxidation and the effect of the oxidation on magnetic properties of cobalt have not been studied in detail.

Cobalt and its oxides can be distinguished through x-ray absorption spectroscopy

[1]For this project, Dr. Jaianth Vijayakumar and me made equal contributions. Au/Cr marker deposition on the samples has been done by Dr. Anja Weber from Mesoscopic Systems group at PSI, Pt deposition has been done by Dr. Elizabeth Müller from Electron Microscopy Facility at PSI. XPEEM experiments have been done by J. Vijayakumar, Armin Kleibert, Dr. Carlos A. F. Vaz and me at the Surface/Interface: Microscopy (SIM) beamline at SLS at PSI; HAADF-STEM investigations have been done by Dr. A. Béché and Prof. Dr. Jo Verbeeck from EMAT, University of Antwerp, data analysis was done by Dr. J. Vijayakumar, Dr. A. Kleibert, Dr. C. A. F. Vaz and me.

at the Co L_3 absorption edge since the spectra of Co, CoO and Co_3O_4 have different characteristic peaks. Metallic cobalt appears as a single peak at 779 eV, as shown in panel (a) in Fig. 5.1. The rocksalt CoO spectrum has two additional peaks at 778 and 781 eV, as shown in panel (b) in Fig. 5.1. Lastly, the Co_3O_4 spectrum does not have a pre-peak at 779 eV but the peak at 781 eV is higher then the peak at 780 eV as shown in panel (c) in Fig. 5.1. XA spectroscopy performed as a function of gradual oxidation may reveal chemical changes in the cobalt nanoparticles as they react with oxygen.

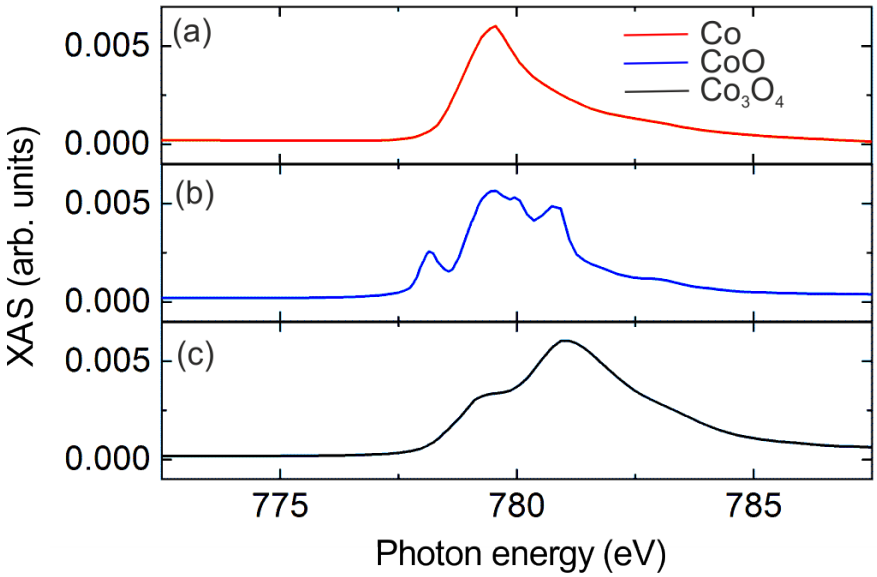

Figure 5.1: X-ray absorption spectra of (a) metallic cobalt, (b) CoO [89] and (c) Co_3O_4 (Supplementary Fig. 19 from [90]).

In Chapter 4 we discussed that the surface may play a key role in the magnetic stability of the nanoparticles and proposed that surface atoms and/or internal defects have a role in enhancing the magnetic anisotropy of cobalt particles. Controlled surface modification of the nanoparticle might be an efficient way to disentangle surface effects from the internal defects. In this work, we investigate the oxidation of metallic cobalt nanoparticles from the very early stage of the oxidation. Using x-ray photo-emission electron microscopy (XPEEM) and high angle annular dark field scanning transmission electron microscopy (HAADF-STEM) we correlate the magnetic properties with structural morphology and chemical state of individual cobalt nanoparticles starting from very low oxygen dosages.

5.1 Chemical and magnetic characterization of oxidized cobalt nanoparticles

The samples with cobalt nanoparticles were produced according to the procedure described in Section 3 (cf. Fig. 3.1 "B1", "B2"). In short, two procedures were used depending on whether the sample was produced for a combined XPEEM and STEM experiment or only for an XPEEM investigation. The nanoparticles for XPEEM and STEM investigations were deposited at room temperature onto the TEM-compatible substrates with SiN membranes (cf. Fig. 3.1 "B1"). The nanoparticles for XPEEM temperature dependent investigations were deposited at room temperature on Si(100) wafers (cf. Fig. 3.1 "B2"). After the deposition of the nanoparticles, the samples were transferred into the XPEEM chamber.

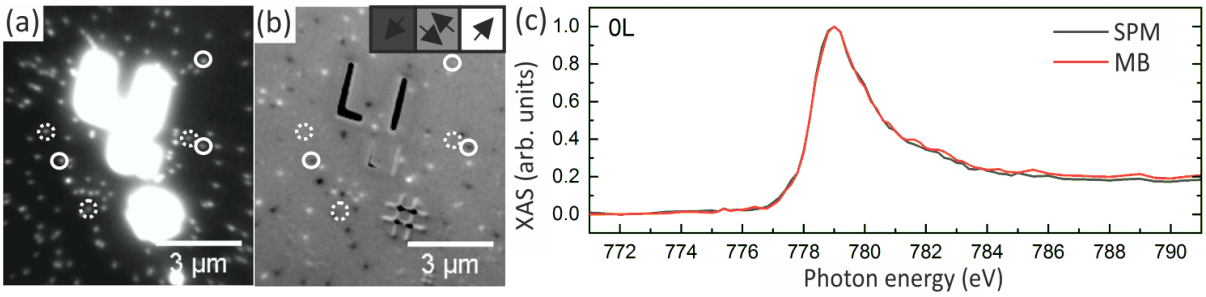

Figure 5.2: (a) Normalized XPEEM image of the sample on a silicon wafer recorded with the photon energy set to the Co L_3 edge at 779 eV. Bright spots correspond to cobalt nanoparticles. (b) Magnetic contrast map of the same region as in (a). Solid circles highlight magnetically blocked nanoparticles, dashed circles highlight superparamagnetic nanoparticles. The inset in the top right corner depicts magnetic contrast variation depending on the in-plane magnetization orientation. (c) XA spectrum of magnetically blocked (MB) and superparamagnetic (SMP) magnetic particles recorded at the Co L_3 edge.

A successful deposition of the particles on the substrate was confirmed by acquiring a normalized XPEEM image of the sample at the Co L_3 absorption edge. A fraction of 20 μm field of view of the sample on the silicon wafer is shown in Fig. 5.2(a). The magnetic properties of the sample were probed by taking an XMCD contrast map at the Co L_3 absorption edge [cf. Fig. 5.2(b)] according to Section 3.2.3. As it was described in Section 3.2.4, cobalt nanoparticles in our samples can be divided into three groups depending on their magnetic contrast variation, (i.e. their visibility in the XPEEM magnetic contrast image): (i) magnetically blocked with $\tau_m > \tau_x$ [cf. solid circles in

Fig. 5.2(b)], (ii) superparamagnetic with $\tau_m < \tau_x$ (dashed circles) and (iii) fluctuating with $\tau_m \sim \tau_x$ (not highlighted). The XA spectra in Fig. 5.2(c) show identical metallic peaks for both magnetically blocked and superparamagnetic nanoparticles, confirming that lack of magnetic contrast in the latter has no chemical origin.

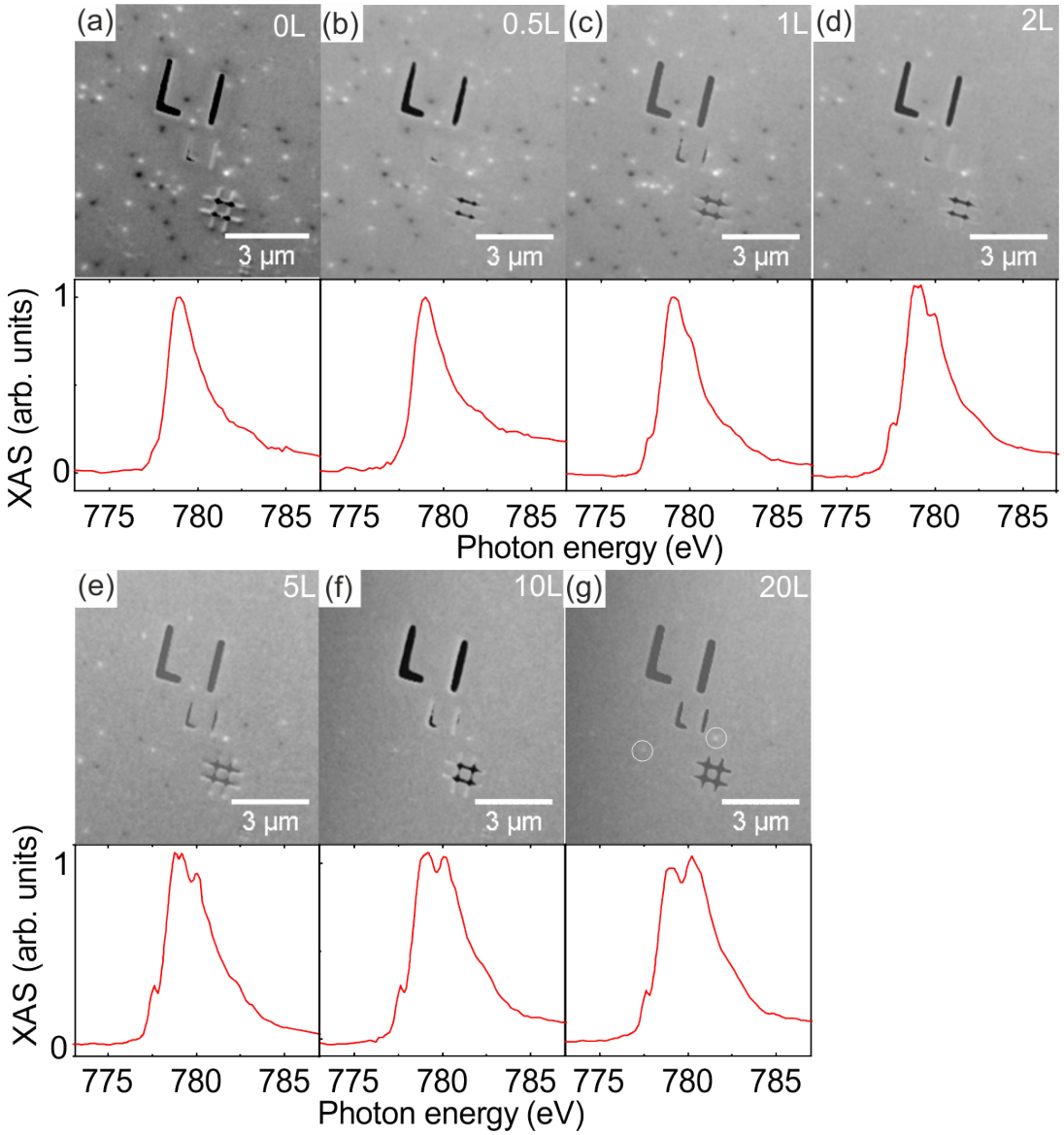

Figure 5.3: XMCD magnetic contrast maps of a fraction of the sample as a function of oxygen dosage: (a) before dosage, (b) after 0.5 L oxygen dosage, (c) after 1 L, (d) after 2 L, (e) after 5 L, (f) after 10 L, (g) after 20 L. The corresponding XA spectra are averaged from 30 nanoparticles.

The nanoparticles were thereafter exposed to molecular oxygen as described in Chapter 3. By definition, 1 Langmuir (L) dosage corresponds to 10^{-6} Torr (1.3×10^{-6} mbar) of gas pressure during one second of exposure [91, p.65]. In our experiment in order to

reach 1 L, we dosed oxygen at $4{\cdot}10^{-9}$ mbar pressure for 185 s. The dosage was varied between 0.5 L and 20 L. An XMCD contrast map and x-ray absorption spectrum of the sample was acquired before and after oxygen dosage. After the last dosage and XPEEM experiment, the samples were covered with 1-2 nm of amorphous carbon layer to avoid ambient air oxidation when transferring to STEM.

After the oxygen dosage, a clear reduction of the magnetic contrast is observed with increasing oxygen dosage. For the case presented in Fig. 5.3(a-g), the dosage was gradually increased from 0.5 L to 20 L on the same sample. In Fig. 5.3(a) many nanoparticles have magnetic contrast. Already after 2 L dosage a clear reduction of the number of magnetically blocked particles is observed [cf. Fig. 5.3(d)]. After 20 L dosage the magnetic contrast of the sample vanishes [cf. Fig. 5.3(g)]. A detailed inspection reveals that two particles still have magnetic contrast after higher oxygen dosages [cf. white circles in Fig. 5.3(g)]. Inspection of the full field of view revealed 10% of nanoparticles remaining magnetically blocked after 20 L dosage. The respective changes in the XA spectra of individual nanoparticle are consistent for all particles across the sample, therefore spectra were averaged between 30 nanoparticles to increase the signal to noise ratio. We classify three different oxidation stages according to their distinct spectral signatures (cf. Fig. 5.1), (i) pure metallic cobalt with a single peak at 779 eV as in panels (a-b), here XMCD contrast does not change, (ii) lower dosage where rocksalt CoO (c-CoO)-like spectrum is detected with the peaks at 778 and 781 eV as in panels (c-d), the magnetic contrast reduces and the number of blocked nanoparticles reduces, (iii) higher dosage, where the onset of Co_3O_4 spectrum begins, detected when the peak at 781 eV grows higher as on the panels (e-g), where only 10% of initially blocked nanoparticles remain magnetically blocked. Such strong contrast reduction may correspond to either a shrinking of the magnetic core volume and therefore transition of the nanoparticles to a superparamagnetic regime or to a formation of a thick non-magnetic oxide layer preventing magnetic imaging due to limited electron escape depth in cobalt (cf. Section 3.2.2).

5.2 Low temperature XPEEM characterization of oxidized nanoparticles

To prove our hypothesis about the magnetic cobalt core shrinking, we exposed a new sample to 2 L and 10 L of oxygen and compared its magnetic contrast maps at room temperature and at 114 K. The sample was deposited on a silicon wafer and pre-characterized in XPEEM before oxidation [cf. Fig. 5.4(a)]. There are many magnetically blocked nanopar-

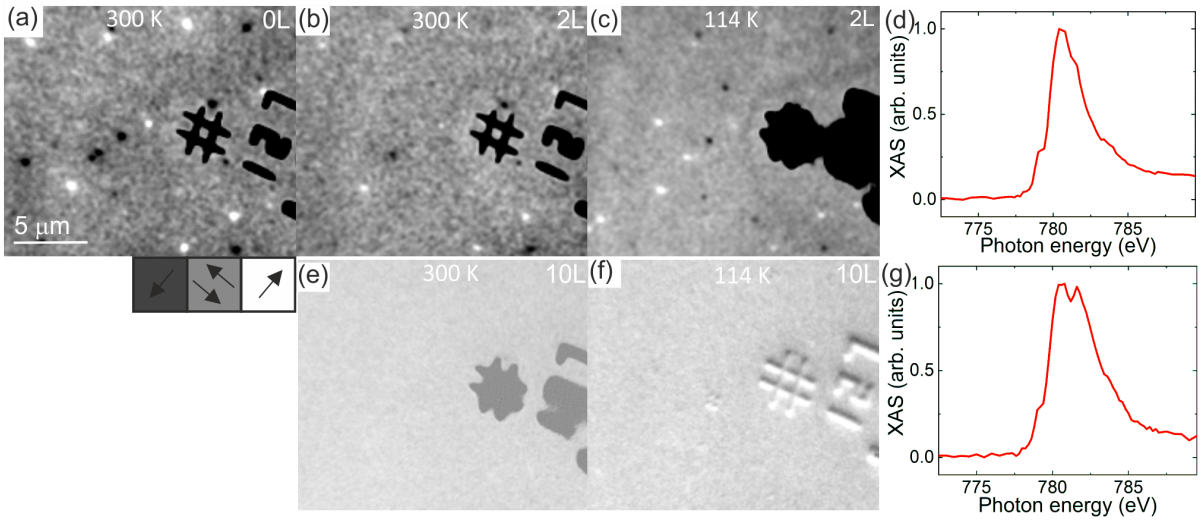

Figure 5.4: Magnetic contrast maps of oxidized nanoparticles upon cooling. Only a fraction of the field of view is shown. The inset in the bottom depicts magnetic contrast variation depending on the in-plane magnetization orientation. (a) XMCD contrast map of metallic cobalt nanoparticles before oxygen exposure. (b) XMCD contrast map of the very same region of she sample as in (a) dosed with 2 L oxygen at room temperature and (c) at 114 K. (d) XA spectrum of the sample with 2L dosage. (e) XMCD contrast maps of cobalt nanoparticles dosed with 10 L oxygen at room temperature and (f) at 114 K. (g) A respective XA spectrum of the 10 L dosed sample.

ticles (bright and dark dots on the image). The detailed inspection of the whole field of view revealed that 65 % of 200 nanoparticles were magnetically blocked after deposition. The XAS (not shown) showed that the sample was metallic and not oxidized. Then, the particles were dosed with oxygen until we observed a CoO signature in the XA spectrum corresponding to (ii) oxidation state, as shown in Fig. 5.4(d). After oxidation, an XMCD image [cf. Fig. 5.4(b)] confirms that half of magnetically blocked nanoparticles have lost their contrast. After that, the sample was cooled to 114 K where XMCD contrast [cf. Fig. 5.4(c)] reappeared for 23 nanoparticles in the full field of view. Further cooling lead to continuous reappearance of magnetic contrast in the sample. In total, XMCD contrast maps of the sample at 114 K, 75 K and 58 K were acquired (not shown). Such behavior correlates with magnetic blocking of the sample below 114 K, indicating T_b to be above 114 K for at least 23 nanoparticles.

Our results with intermediate oxidation confirm that the net magnetic moment of the particles is not affected by the surface oxidation since 23 of 65 initially magnetically blocked nanoparticles reappeared upon cooling to 114 K, 13 of them with the same

magnetic contrast as before the oxidation. Such an effect was observed in all particles independently of the size and shape similar to the magnetic behavior of iron nanoparticles upon oxidation [23].

To investigate the temperature effect at higher dosages, the sample was warmed up to room temperature, then the particles were dosed further until a Co_3O_4 signature was observed in the XA spectra [cf. Fig. 5.4(g)]. At this oxidation stage, we find that most of the particles lost their magnetic contrast [cf. Fig 5.4(e)]. The sample was cooled again down to 114 K and in this case no magnetic contrast recovery was observed as shown in Fig. 5.4(f). Our results do not allow to conclude whether the XPEEM probing depth through cobalt oxide was reached which made the magnetic core of the particles undetectable or the reached temperature was higher than the blocking temperature of cobalt cores. In total, 20 % of initially blocked nanoparticles kept magnetic contrast even after higher oxygen dosage (not shown). We attribute the magnetization stability of some particles to a strong shape anisotropy contribution similar to the results discussed in Section 4.2.2.

5.3 HAADF-STEM structural characterization

In order to investigate the structure of the particles at different oxidation levels, HAADF-STEM was performed. The goal of STEM imaging was to determine the core-shell structure of the particles, correlate shell thickness with XAS results and to look at the oxide species forming at early oxidation stages. Three samples on TEM-compatible membranes were produced for three dosages: 1 L, 2 L and 20 L. Six particles were imaged for each dosage. For each image an electron energy loss spectroscopy (EELS) scan has been done separately for the core and shell. We have compared these data with XAS spectra that we obtained from XPEEM characterization. The results are shown in Fig. 5.5.

The STEM images of individual cobalt nanoparticles, one for each dosage, the corresponding EELS and the XAS are shown in Fig. 5.5. From the STEM images shown in Fig. 5.5(a-c), we find that the nanoparticles indeed represent a core/shell structure with a dense metallic core appearing brighter in the figure and a lighter oxide shell with darker contrast in STEM. The particles have polycrystalline structure. Some of the atomic planes are enlarged in the panels below the STEM images. Insets "I" show some of the crystallites in the shells, insets "II" show crystallites visible within the core of the particles, which however, may also partly correspond to the shell. The oxide shell grows inhomogeneously with dosage. A detailed inspection of STEM images revealed that at

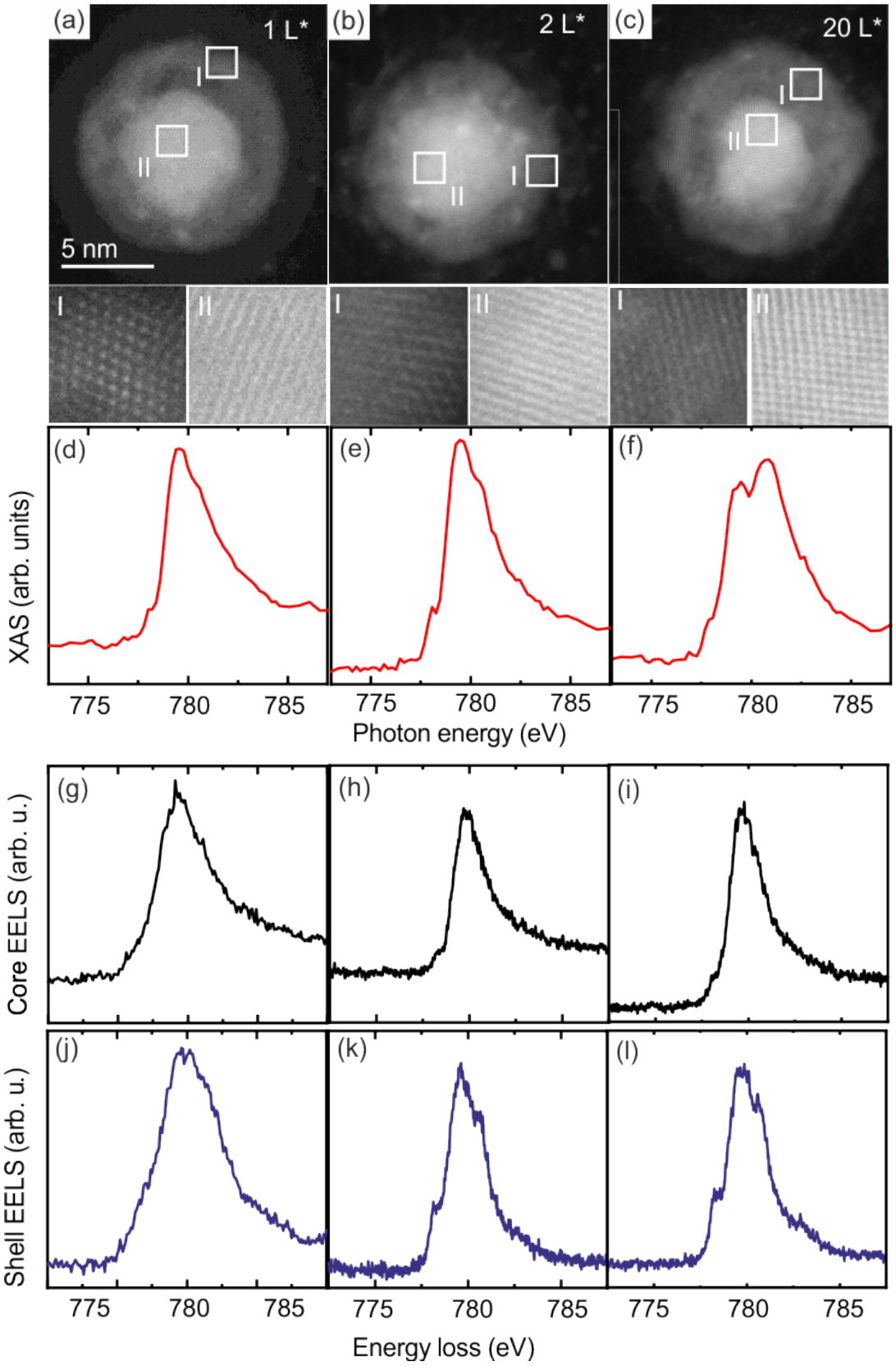

Figure 5.5: (a-c) HAADF-STEM images of nanoparticles. (d-f) XA spectra acquired from XPEEM. (g-i) EEL spectra of the core. (j-l) EEL spectra of the shell.

1 L a thick shell with many defects is formed, and the average shell thickness is 4.3±0.5 nm. At 2 L dosage a more compact shell is observed, and the average shell thickness is 3.5±0.3 nm. At 20 L dosage the shell grows thicker resulting in a shell thickness of 4.5±0.4 nm, with the shell looking denser. The core diameter is 12.4±2.4, 12.6±3.6, 9.2±2.8 nm for 1 L, 2 L and 10 L, respectively. Already at 1 L dosage the shell looks complete but inhomogeneous. It is possible that at the lower dosages the shell starts to develop in the form of islands on top of the cobalt core and grow till the islands merge, forming a rough polycrystalline shell full of defects. Longer oxygen dosage results in thickening of the oxide shell similar to some other experimental observations [88, 92]. Even at the highest dosage (20 L for STEM measurement) a metallic core is still visible below the oxide shell in STEM.

Figure 5.5 show EELS spectra of individual nanoparticles acquired from the core (g-i) and shell (j-l) regions which can be clearly compared with the averaged XA spectra of the same sample acquired using XPEEM shown in (d-f). We find that the EELS spectra of the shell and XAS are in good agreement for 1 L and 2 L dosages. However, for 20 L dosage, the EELS spectra show the signature of a lower oxidation state (CoO), even though we find a characteristic spectrum of Co_3O_4 in XAS. Such lower oxidation state found in the shell in EELS may be assigned to a partial reduction of the oxide shell by the electron beam during the STEM measurements. Furthermore, we find that the EELS spectra for the core show a weak oxide signature which can be attributed to the shell signal interfering with the core since STEM signal is collected in a transmission whereas XAS gives surface information of few nanometers and largely consists of the signal of the shell. Our results also confirm that the carbon layer protects the nanoparticles from further oxidation, since no evidence of stronger oxidation was detected.

5.4 Discussion

5.4.1 Fits to the x-ray absorption spectra

To obtain a quantitative insight onto the structure of the oxide shell, the XA spectra shown in Fig. 5.3 were fitted using a model based on the total electron yield (TEY) signal for a multilayer system using a combination of reference spectra for Co, CoO and Co_3O_4 shown in Fig. 5.1 [23, 89]. We assume that upon *in situ* oxidation, at first cobalt oxide isles are formed on top of the nanoparticle and not detected with XA spectroscopy and therefore XAS for 0.5 L dosage [cf. Fig. 5.3(b)] looks similar to the metallic cobalt spectrum [cf. Fig. 5.3(a)]. At higher dosages, a complete oxide shell is formed first

with CoO and then a core/shell/shell structure composed of Co/CoO/Co_3O_4 resulting in drastic changes in the XAS. A simplified model of the nanoparticle oxidation is sketched in Fig. 5.6.

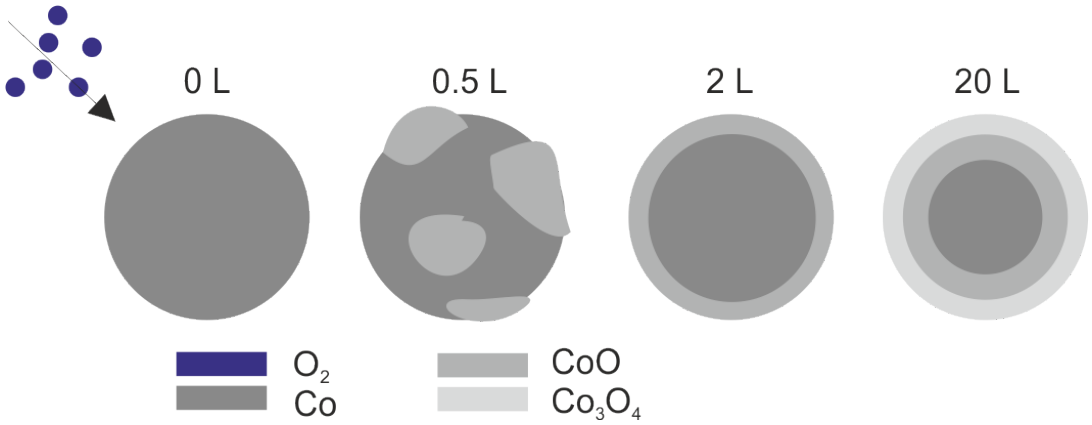

Figure 5.6: A simplified model of cobalt core/ cobalt oxide shell formation. The cobalt nanoparticle is exposed to molecular oxygen, which results in a formation of CoO-like clusters on top of the nanoparticles at 0.5 L dosage. At higher dosages, the clusters close into an amorphous shell. Even higher dosages lead to further oxidation and formation of Co_3O_4 layer.

For the fit, we do not take into account the curvature of the nanoparticles but only the thickness of the layers. The thickness of the oxide layers is varied to fit the simulated XA spectra with the experiment [cf. Fig. 5.3] and in order to estimate the thickness of the different oxide layers. For the fits, we have used normal x-rays incidence and the escape depths 22 Å for cobalt and 30 Å for cobalt oxides [89]. The results of the fitting are presented in Fig. 5.7. The XA spectra acquired after each dosage are plotted in red lines and the fits to the XA spectra with dashed lines. The thickness used for the fits are denoted above each spectrum. From our fitting we observe that at the early oxidation stage (i) no oxide shell can be detected with XAS showing that the particles are still largely unoxidized. At 1 L and up to 2 L dosage (ii), the onset of CoO spectrum starts to be visible, which can be observed from the presence of a shoulder before and after the Co metallic peak at 778 eV and 781 eV, respectively. At 5 L and further on (iii) a spectral signature of spinel Co_3O_4 starts to form and CoO contribution saturates at a certain thickness. At the maximum oxygen dosage, the total oxide shell reaches 40 Å.

Fitting of the intermediate stage may not look perfect due to simplicity of the model. For instance, the model does not reflect the inhomogeneous structure of the shell. The fit confirms that the oxide shell consists of CoO up to 2 L oxygen dosage and of CoO and Co_3O_4 for higher dosages. The fit estimates for the shell thickness shown that it grows

to almost the limit of XPEEM probing depth (5 nm for cobalt) which could be one of the reasons for XMCD contract reduction.

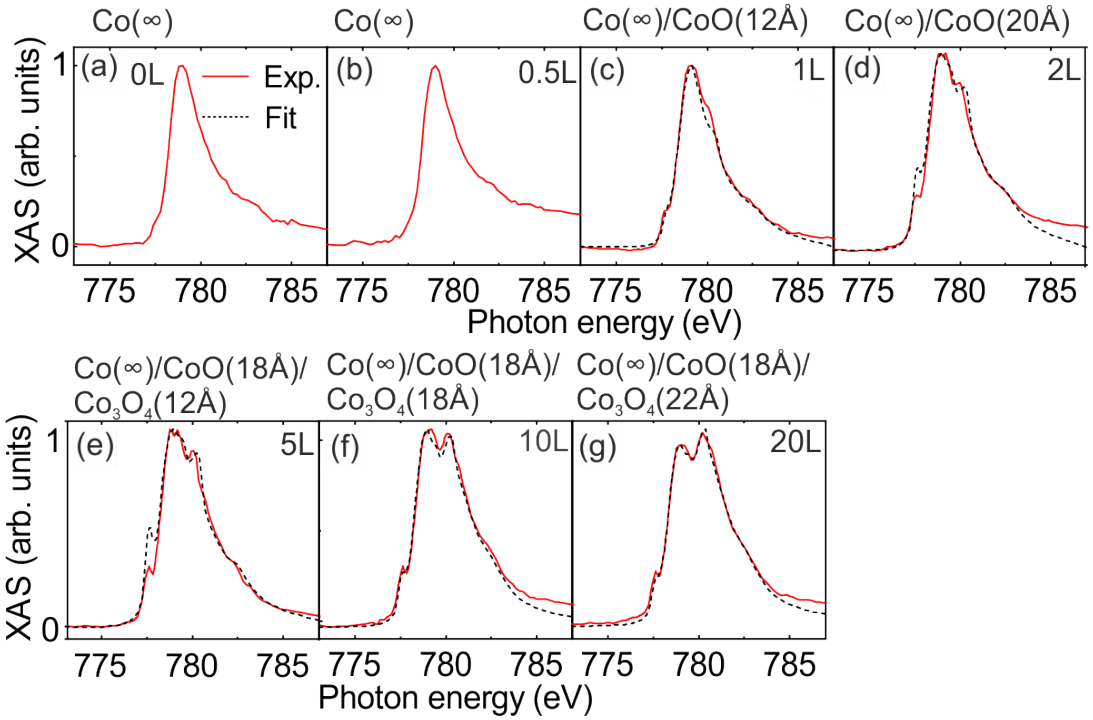

Figure 5.7: Fitting of the x-ray absorption spectra for cobalt oxide nanoparticles dosed with (a) 0 L, (b) 0.5 L, (c) 1 L, (d) 2 L, (e) 5 L, (f) 10 L, (g) 20 L of molecular oxygen using total electron yield model [89] for a stack of $Co/CoO/Co_3O_4$.

The shell thickness derived from XAS fits underestimates real shell thickness obtained from STEM investigations by almost a factor of 2. STEM imaging reveals that the actual shell thickness reaches 5.1 nm at 20 L dosage which is at the limit of XPEEM probing depth.

We can estimate how the blocking temperature of the metallic core changes upon the oxidation of the nanoparticle. The volume of the magnetic core shrinks with the growth of an oxide shell on top of it. According to STEM data, an average core diameter is 12.4±2.4 nm for low dosage and, 9.2±2.8 nm for high dosage. The blocking temperature can be calculated by the Arrhenius law $T_b = K \cdot V \cdot ln(\tau_x \cdot \nu_0)/k_B$, where K=3.8 μeV/atom is the magnetocrystalline anisotropy energy [11], V is the particle volume (in atoms for convenience), k_B is the Boltzmann constant, τ_m=400 s is the measurement time and ν_0=$1.9 \cdot 10^9$ s^{-1} is the attempt frequency of fcc cobalt, respectively, as discussed in Section 2.1.3. We estimated T_b= 50 K for 20 L and T_b= 90 K for 2 L oxygen dosage. That would mean, the nanoparticles undergo a transition to the magnetically blocked state while cooling and we were able to see the recovery of magnetic contrast at 58 K.

In Chapter 4 we have proposed that the origin of high magnetic anisotropy of cobalt nanoparticles may be due to a high surface anisotropy. The results of the current Chapter show that even though the surface of the nanoparticles was modified, the magnetic contrast and therefore the magnetization direction remains for a large number of nanoparticles, as discussed in Section 5.2. The strong anisotropy of the nanoparticles might have another origin, for example, structural defects.

5.5 Conclusions

In summary, we have investigated the magnetic, chemical and structural evolution of cobalt nanoparticles in the early stages of oxidation. Our magnetic characterization shows that the magnetic contrast of individual nanoparticles, gradually reduces with oxygen dosage due to the attenuation of the signal of the metallic core by the growth of the oxide shell. Ultimately, this results in a transition from magnetically blocked to superparamagnetic state, which is assigned to the reduced magnetic volume of the nanoparticle. By reducing the temperature down to 58 K, we find that the magnetic contrast, which disappeared with formation of CoO oxide shell, reappears, showing that the magnetic core is magnetically blocked at low temperature. From our results we conclude that the cobalt nanoparticles have a strong anisotropy which does not originate from a surface anisotropy contribution but is rather associated to internal structural defects of the particle. Our STEM data shows a surprisingly complicated oxidation kinetics and formation of core/shell structure. We find that after 1 L oxygen dosage, the initial oxidation of cobalt nanoparticles results in a rough CoO shell with apparent voids while at higher oxygen exposure the oxide shell appears more compact; at the highest oxygen dosage the shell is composed of both CoO and Co_3O_4. We have fitted a core/shell model based on reference spectra to the XA spectra to estimate the oxide shell thickness forming on the nanoparticles. Our HAADF-STEM data suggests that the fits significantly underestimate the oxide shell thickness probably because of a complex structure of the shell especially at low oxidation stages. These observations suggest that the initial oxidation occurs on the surface in the form of islands at certain favorable reaction sites, while a complete oxide shell is formed only at later stages of oxidation. The complex morphology of the nanoparticles could have implications for understanding catalytic activity of cobalt nanoparticles in chemical reactions such as the Fischer-Tropsch synthesis. Moreover, cobalt oxide phases present in the oxide shell might be helpful to understand the exchange bias effect in these materials.

Chapter 6

Laser induced manipulation of cobalt nanoparticles

We investigate the effect of 50-fs laser pulses of different intensities and polarizations on individual, supported cobalt nanoparticles.[1] Purely laser-induced magnetization switching, so-called all-optical switching, is a promising approach, which might be employed for fast data recording at unprecedented bit rates. So far, most studies on laser excitation of magnetic media are carried out on thin films [31, 33, 30], granular media [93] or micron-sized structures [64]. Although all-optical switching was found in several materials, the microscopic mechanism of the switching remains unclear. The occurence of all-optical switching depends on the material and experimental parameters [33]. Switching may occur deterministicly after one pulse (eg. GdFeCo [31, 64, 33]) or after a large number of laser pulses (eg. Co/Pt, TbCo [33, 64] or orthoferrites [94]), be dependent on laser polarization and laser fluence (eg. Co/Pt, TbCo [33] or FePt [33, 93]) or independent of those (eg. GdFeCo), happen thermally or athermally. First reported for GdFeCo thin films, a helicity-dependent magnetization switching has been observed at fluences higher than 2.9 mJ/cm^2 [31], when film was heated close to the Curie temperature ($T_C = 500K$). For a narrow fluence window, a deterministic switching occurs only at one of the two circular

[1] In this work, XPEEM experiments have been carried out by Dr. Michelle Buzzi, Dr. Ludovic Howald, Dr. Jaianth Vijayakumar, Martin Timm, David Bracher, Dr. Carlos A. F. Vaz, Dr. Armin Kleibert and me at the Surface/Interface: Microscopy (SIM) beamline of the Swiss Light Source (SLS) at PSI. The alignment of the laser setup was done by Dr. M. Buzzi, Dr. L. Howald, Dr. J. Vijayakumar, Dr. Susmita Saha and me. The samples were prepared by Dr. A. Kleibert and me. Au/Cr marker deposition on the samples has been done by Dr. Anja Weber from the Mesoscopic Systems group at PSI, Pt deposition has been done by Dr. Elizabeth Müller from the Electron Microscopy Facility at PSI. Temperature modelling was done by Dr. A. Kleibert and Dr. Sergiu Ruta from Department of Physics, University of York. Data analysis was done by Dr. A. Kleibert and me.

polarizations, which was attributed to magnetic circular dichroism effect [95] due to the different absorption of polarized light of opposite helicities. While for one helicity the material is being heated above the T_C, for other one the T_C is not achieved. For higher fluences, switching occurs in the outer perimeter of the laser spot where the temperature is just below the T_C, deterministically, and only for circular light polarization [31, 64, 33]. The internal part of the spot remains with no magnetic contrast for both circular and linear polarization. For other materials, like Co/Pt and TbCo, the all-optical switching effect is helicity-dependent but can only be achieved after a large number of shots through formation of multi-domain structure.

Several microscopic effects were proposed to explain the all-optical switching. Most of them require the instantaneous overcoming of either the T_C or compensation temperature, where magnetization of rare earth sublattice equals to the magnetization of transition metal lattice. One of the proposed mechanisms is the inverse Faraday effect, that induces a helicity-dependent magnetization component in the material exposed to the polarized light, but an exact nature of this effect is not understood. Another effect is the formation of transient ferromagnetic state due to different demagnetization times for the rare earth and transition metal atoms [33]. However, while those effects can explain switching of GdFeCo films and the effect of circular polarized light to achieve deterministic switching, they cannot provide an explanation for the results on Co/Pt and Co thin films. There, a multiple shot helicity-dependent switching is achieved on the outer rim of the laser spot and in the center the material switches into a multiple domain state due to stray field minimization. Using intrinsically single domain magnets would help to avoid multiple domain state formation. Therefore, excitation of individual single domain nanoparticles with fs-laser opens up an opportunity to study a pure optical switching.

Many magnetic nanoparticles express superparamagnetic behaviour at room temperature. The magnetization of superparamagnetic particles fluctuates rapidly, which makes it difficult to investigate effect of laser pulses on the nanoparticles. Recently, cobalt nanoparticles have been found in a magnetically blocked state with a magnetic energy barrier of about 0.63 eV at room temperature [11]. Their sizes distributed around 10 nm make it energetically unfavourable to form a multiple domain state within the nanoparticle. Hence, the absorption of a single laser pulse could result in a thermally driven stochastic magnetization reversal due to laser-induced heating. We investigate the effect of single 50 fs laser pulse excitation with a wavelength of 800 nm on individual, well isolated cobalt nanoparticles with sizes ranging from 8 to 20 nm, covered with 1-2 nm of amorphous carbon. We employ a laser excitation with circular and linear polarization in

order to determine helicity-dependent effect from helicity-independent one. In general, we are sensitive to the equilibrium state of the system after a single fs laser pulse. The response of the nanoparticles to the laser pulses is studied by combining x-ray photoemission electron microscopy (XPEEM) with x-ray magnetic circular dichroism (XMCD) and x-ray absorption spectroscopy (XAS). This approach allows us to determine the magnetic and chemical state of individual nanoparticles before and after a laser pulse excitation.

Stochastic thermal fluctuations of magnetic energy of the nanoparticle lead to the energy to overcome the magnetic anisotropy barrier as discussed in Chapter 2. At room temperature such fluctuations can happen, however the probability of such switches increases with growing temperature of the system. Thus, laser heating can potentially lead to a stochastic switching of nanoparticles magnetization. As discussed in Chapter 4, internal structural defects lead to increased magnetic anisotropy in fcc cobalt nanoparticles, but modification of surface leads to less magnetic stability as discussed in Chapter 5. Therefore, structure and chemical modification may affect magnetization stability of the nanoparticles.

Extrapolating from the results reported for thin cobalt films and nanoparticles, the following effects of laser pulses on cobalt nanoparticles could occur:

1. Thermal effects:
   (a) Stochastic thermally driven magnetization fluctuations,
   (b) Changing of magnetic anisotropy of the particles due to structural deffects,
   (c) Thermally induced chemical modification.
2. Ultra-fast effects at the T_C:
   (a) Inverse Faraday effect (for σ_+ and σ_- polarization),
   (b) Momentum transfer via exchange coupling (for lin., σ_+ and σ_- polarization).

6.1 XPEEM characterization

The samples for the *in situ* XPEEM experiments were prepared according to the procedure described in Section 3.1 [cf. Fig. 3.1 "C1","C2"]. In short, the nanoparticles are deposited at room temperature onto Si wafers, with a native SiO_x layer, and are subsequently covered with 1-2 nm of amorphous carbon under UHV conditions as schematically depicted in Fig. 6.1(a). The carbon layer is used in our experiments to avoid the loss of

contrast after many hours of x-ray exposure. The size of the nanoparticles varies between 8 and 20 nm, and the average particles density on the wafer is 1 particle per μm^2. Then the sample is transferred under UHV conditions into the microscope. The nanoparticles are metallic after deposition, which was confirmed with XA spectroscopy at the Co L_3 absorption edge where only the the metallic Co peak is visible at 781 eV [cf. Fig. 6.1(b)].

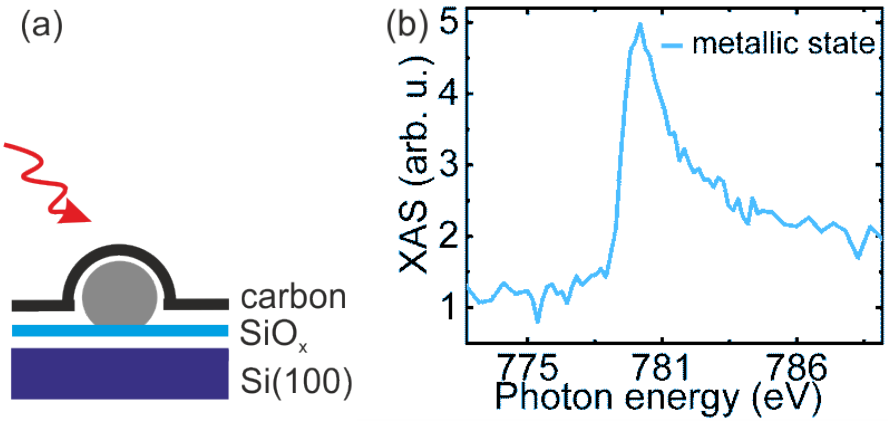

Figure 6.1: (a) Schematic drawing of the sample: fcc cobalt nanoparticle (grey disk), Si(100) wafer (violet) with a native oxide layer (blue), and the amorphous carbon film with a thickness of 1 – 2 nm (black). (b) XA spectrum of the nanoparticles recorded prior to the laser experiment at the Co L_3 edge.

The distribution of the nanoparticles on the wafer is shown in Fig. 6.2(a) which displays a normalized XPEEM image recorded at the Co L_3 edge. Bright spots correspond to individual cobalt nanoparticles. The depicted image shows only a smaller area of the investigated field of view of 20 μm, which is centered around the laser spot. Fig. 6.2(b) shows the magnetic contrast map of the same sample area as in Fig. 6.2 (a). The laser spot size impinging on the sample is 20×70 μm^2 and is determined with femtosecond laser illumination in PEEM on a Cs sample [cf. Fig. 6.2(c)] prior to the actual experiment. As described in Section 3.2.4, nanoparticles in our samples can be divided into three types depending on their magnetic contrast variation visible with XPEEM: (i) magnetically blocked with magnetic relaxation time $\tau_m >$ the acquisition time τ_x, (ii) superparamagnetic with $\tau_m < \tau_x$ and (iii) fluctuating with $\tau_m \sim \tau_x$.

In the experiment, we employ single 50 fs laser pulses to excite the nanoparticles. The laser polarization is adjusted with a $\lambda/4$ plate between linear and circular (σ_+ and σ_-). The laser fluences employed for the experiment repoted here are listed in Tab. 6.1 and vary between 1 and 21 mJ/cm^2.

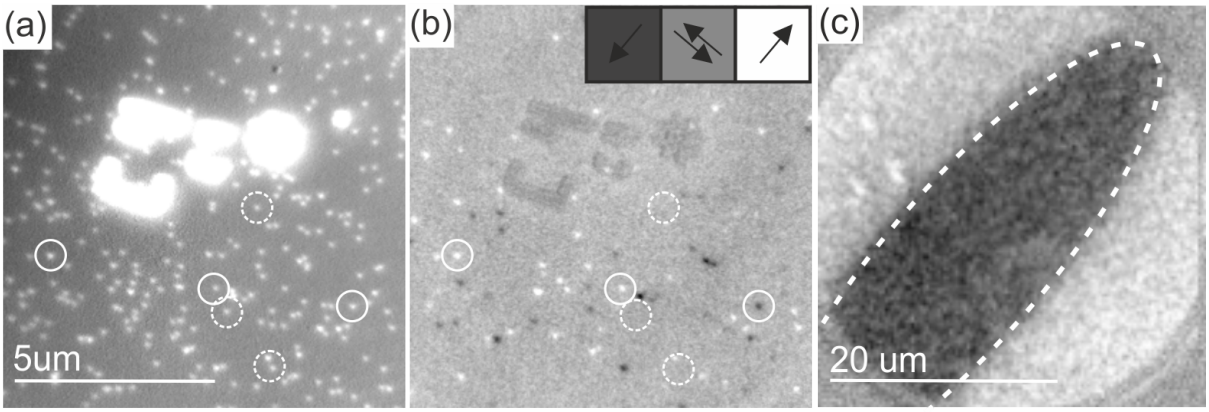

Figure 6.2: (a) Normalized XPEEM image of a sample recorded with the photon energy set to the Co L_3 edge at 781 eV. Bright spots correspond to cobalt nanoparticles. (b) Magnetic contrast map of the same region. Solid circles highlight some magnetically blocked nanoparticles. Dashed circles denote nanoparticles without magnetic contrast. The inset in the top right corner depicts magnetic contrast variation depending on the in-plane magnetization orientation. (c) Laser spot in XPEEM. Dashed line highlights the spot.

Laser pulse energy E(nJ)	14 ±1	65±3	150±8	270±14	352±18
Peak fluence F_0 (mJ/cm^2)	1±1	4±1	9±3	16±6	21±8
Photon density n_{Ph} (photons/nm^2)	35±10	160±60	370±130	660±240	860±310

Table 6.1: Investigated laser pulse energies, peak fluences, and respective photon densities with estimated errors.

6.1.1 Series of magnetic contrast images without laser exposure

Each experiment starts from a series without laser exposure where ten subsequent XMCD contrast maps are recorded as a control experiment to determine the initial magnetic state of the nanoparticles and to distinguish possible thermally induced spontaneous magnetization flipping events. The first image in Fig. 6.3(a) shows a normalized XPEEM image of a smaller region of the sample, which is representative for the investigated field of view of 20 μm. Then, panels (b)-(k) display a series of ten magnetic contrast maps of the very same region as in (a), acquired without laser excitation and averaged over τ_x^{short}=400 s (a typical acquisition time for a magnetic contrast map, cf. Section 3.2.2), the total series time τ_x^{long}=4000 s. An example of magnetically blocked nanoparticle (nanoparticle "1") is highlighted in Fig. 6.3(b) –(k) with a solid circle as a guide to the eye. This nanoparticle is stable all over the series, i.e. $\tau_m > \tau_x^{long}$. At the same time, a

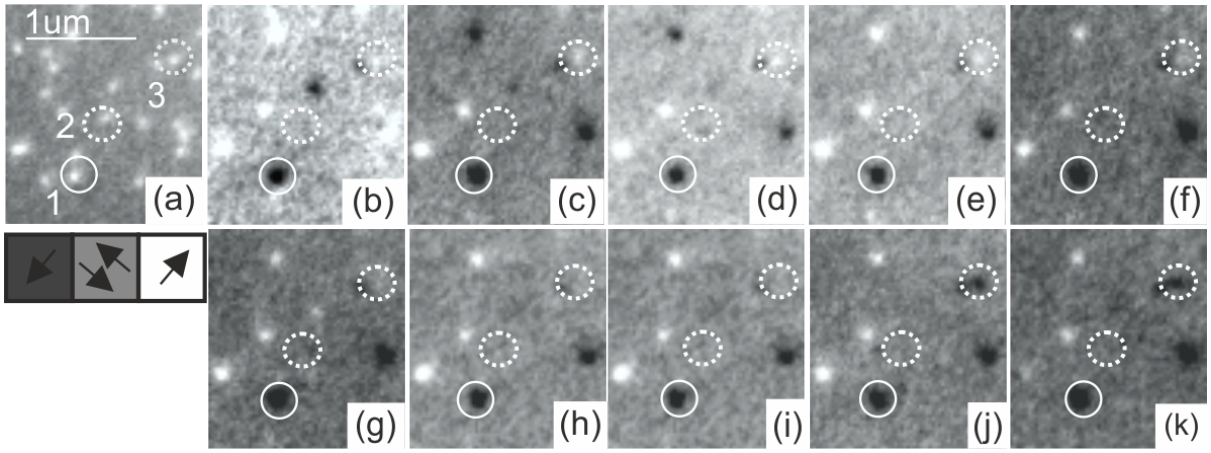

Figure 6.3: Series without laser exposure before low intensity laser pulse exposure. (a) Normalized XPEEM image recorded at the Co L_3 edge. (b)-(k) Sequence of magnetic contrast maps without laser exposure. The scale bar in (a) corresponds to 1 μm. The solid circle denotes a magnetically blocked nanoparticle while the two dashed circles highlight nanoparticles, which exhibit no or unstable contrast over the sequence. The inset with arrows depicts magnetic contrast variation depending on the in-plane magnetization orientation.

number of nanoparticles without or with unstable magnetic contrast can be identified. For instance particle "2", which exhibits no contrast in all images. In contrast to particles "1" and "2", particle "3" shows white magnetic contrast in the panels (b) – (f), but changes then to black in (j) and (k). For such particles magnetic contrast is fluctuating with $\tau_x^{short} < \tau_m < \tau_x^{long}$. The statistics of magnetic contrast of the particles without laser excitation is listed in Tab. 6.2, 1^{st} series. In the experiment, out of 566 nanoparticles visible in the field of view, 182 nanoparticles are magnetically blocked, 338 nanoparticles do not have magnetic contrast and the remaining 46 are thermally unstable over the series without laser excitation.

6.1.2 Low laser fluence excitation

After exposing the sample to very low intensity linear polarized laser pulses with E = 14 nJ we have not observed any effect different from the series without laser exposure. Therefore, we switched to the next laser intensity. The effect of excitation with low intensity laser pulses with E = 65 nJ ($\mathcal{F}_0$= 4 mJ/cm^2) and linear polarization is presented in Fig. 6.4, panels (b)-(k). All magnetic contrast maps were acquired with the same timing, statistics and on the same spot as the series without laser excitation in Fig. 6.3. First, we observe that the black contrast of the nanoparticle "1" remains unaffected by all

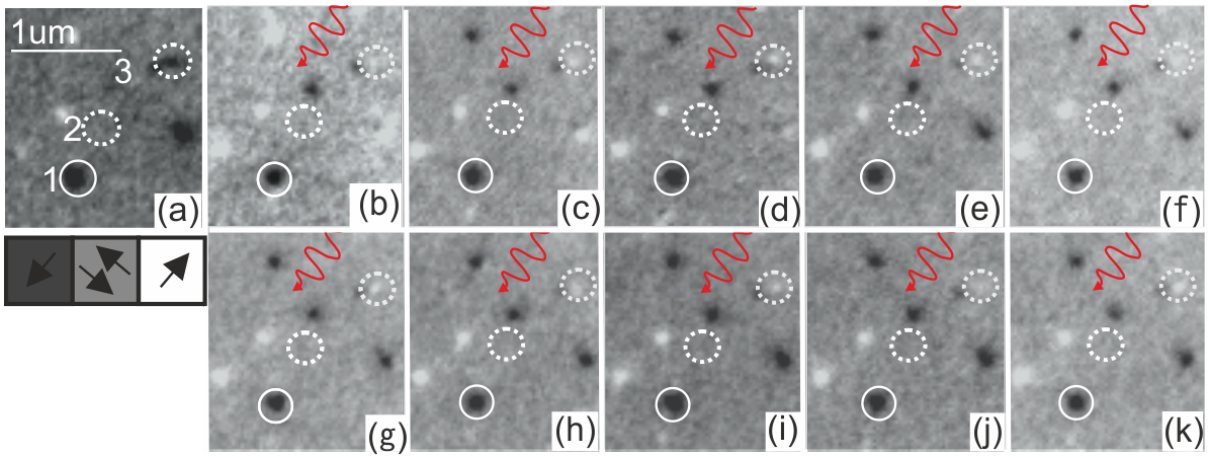

Figure 6.4: Laser exposure series with E = 65 nJ ($\mathcal{F}_0 = 4$ mJ/cm^2) and linear polarization together. (a) Magnetic contrast map at the Co L_3 edge before the laser pulse was applied. (b)-(k) Magnetic contrast maps, each recorded upon the exposure to a single laser pulse. The scale bar in (a) corresponds to 1 μm. The solid circle denotes a magnetically blocked nanoparticle while the two dashed circles highlight nanoparticles, which exhibit no or unstable contrast over the full experimental sequence. The inset with arrows depicts magnetic contrast variation depending on the in-plane magnetization orientation.

laser pulses. This behavior is found in most magnetically blocked particles at this laser pulse energy and for this laser polarization. The total number of magnetically blocked particles is 173 (cf. Tab. 6.2, 2^{nd} series). Only in a few particles we observed a change of the sign or loss of magnetic contrast. However, with the available data it is impossible to conclude, whether such magnetic contrast loss/reversal was a stochastic magnetization reversal, a consequence of a chemical modification of the particles or indeed was a magnetization switching induced by the laser pulses. Similarly to the case of magnetically blocked particle "1", particle "2" in Fig. 6.4 reveals no detectable change in magnetic behavior upon laser excitation. Finally, the particle "3" changes black contrast to white after the first laser pulse and remains with white contrast throughout the sequence of laser pulses showing an evidence of magnetic blocking. In total out of 338 nanoparticles without magnetic contrast, all remained with no contrast and 6 more (magnetically blocked) nanoparticles lost their contrast resulting in total of 344 particles without magnetic contrast (cf. 6.2, 2^{nd} series). Only in four nanoparticles a transition from thermally unstable to the magnetically blocked behavior was found, similar to the nanoparticle "3", which could potentially be associated with a presence of lattice defects and their enhancement upon laser excitation causing magnetic stabilization within τ_x^{long}.

Laser excitation with circular polarized light has also been performed at the very

No of particles: No of series (pulses):	In total	Magnetic. blocked	No magn. contrast	Thermally unstable	Comments
1^{st} series (0)	566	182	338	46	without laser
2^{nd} series (10)	566	173	344	49	lin. hor. polariz.
3^{rd} series (20)	566	111	384	71	σ_+/σ_- polariz.

Table 6.2: Summary of magnetic contrast of the nanoparticles with and without low intensity laser excitation (4 mJ/cm^2).

same spot as in Figs. 6.2 and 6.3. The laser fluence was kept at 4 mJ/cm^2. Single laser pulses were applied in alternating fashion: $\sigma_+, \sigma_-, \sigma_-, \sigma_+, \sigma_+$... and so on. After each laser pulse an XMCD image of the spot has been taken. 10 images were recorded in total. The results are summarized in Tab. 6.2, 3^{rd} series. 62 of previously magnetically blocked nanoparticles turned into thermally unstable or lost their contrast which indicates a reduction of magnetic energy barrier after laser pulses.

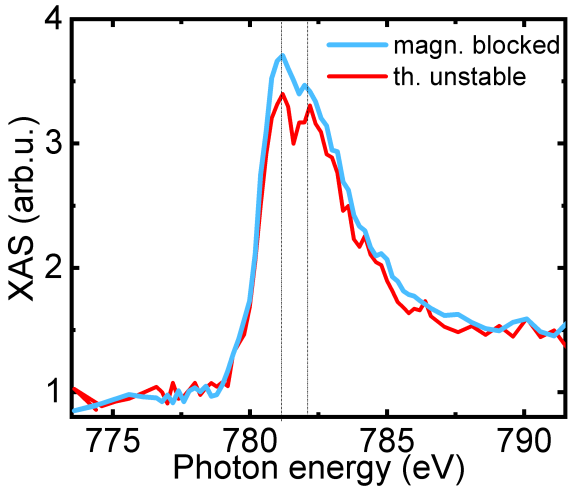

Figure 6.5: XA spectra of long-term blocked nanoparticles (blue line) and thermally unstable nanoparticles (red line).

XA spectra recorded after the laser experiments separately for blocked nanoparticles and for thermally unstable ones revealed a slight oxidation/carbonation of both types of the particles. Each XA spectrum was averaged from signals from 100 nanoparticles. A small difference between the spectra is within error bars (cf. Fig. 6.5), which arises from the noise in single nanoparticle XAS. It is not clear why red curve is lower than the blue (cf. Fig. 6.5), but could be associated with microfocusing effect [96]. If the height

of the XAS peaks would be associated with nanoparticle's size, then thermally unstable nanoparticles would have less magnetic volume and therefore their magnetization would be less stable. The evidence of turning of part of the particles from magnetically blocked to thermally unstable ones can be described by gradual chemical modification of the particles after each laser pulse and will be addressed in the discussion. Such behavior was found for 4 mJ/cm^2 fluence, at lower fluences no effect of laser pulses was detected for all polarizations.

6.1.3 High laser fluence excitation

At higher fluences of the laser pulse, we observed even more drastic effect of the laser on the sample. In this section we present the results for 150 nJ fluence (9 mJ/cm^2). Fig. 6.6 shows a series of XMCD contrast images without laser exposure. We present a different fraction of the same 20×20 μm^2 field of view, previously exposed to low intensity laser. Here, as before, the magnetically blocked nanoparticle ("1"), nanoparticle with no magnetic contrast ("2") and nanoparticle with thermally unstable magnetic contrast ("3") are observed in the sample.

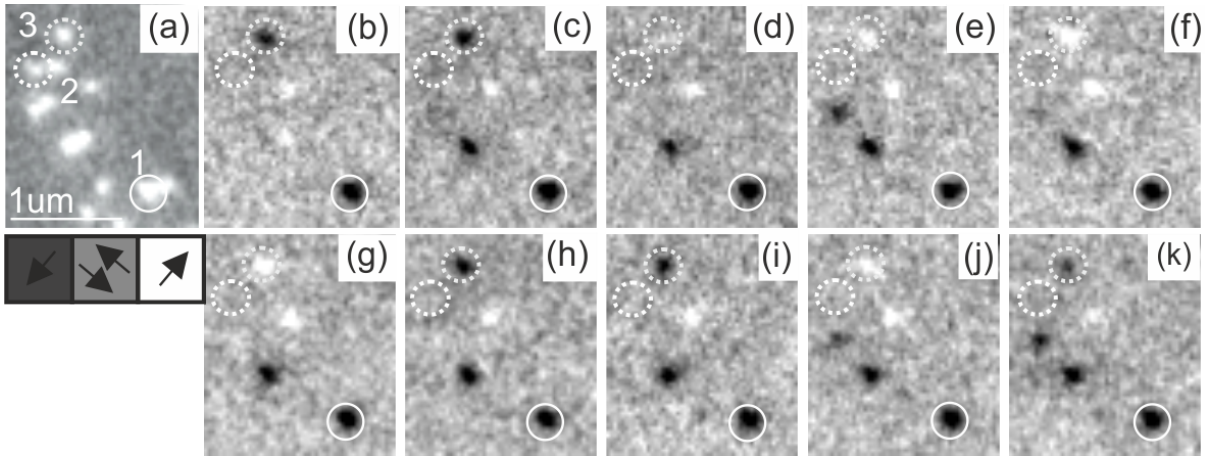

Figure 6.6: Series without laser exposure before 9 mJ/cm^2 fluence laser pulses. (a) Normalized XPEEM image recorded at Co L_3 edge. The scale bar in (a) corresponds to 1 μm. Similar to Fig. 6.3, the solid circle denotes a magnetically blocked particle "1" while the two dashed circles highlight nanoparticles, which exhibit no or no stable contrast over the experimental sequence. (b)-(k) Sequence of 10 magnetic contrast maps without laser exposure. The inset with arrows depicts magnetic contrast variation depending on the in-plane magnetization orientation.

The XA spectroscopy performed after the high intensity laser pulse experiment, re-

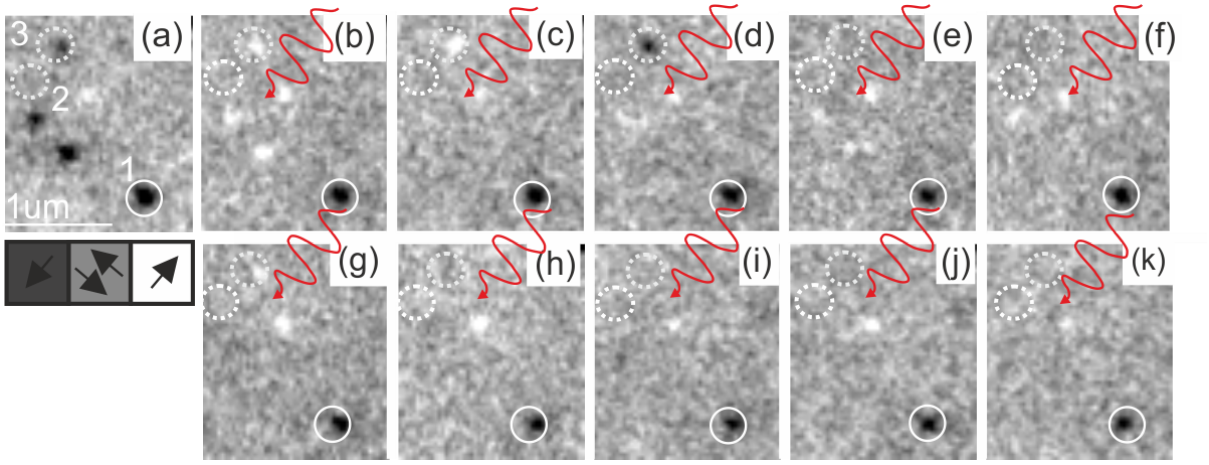

Figure 6.7: Laser exposure series with 9 mJ/cm^2 fluence with linear polarization of the very same area of the sample as in Fig. 6.6. The scale bar in (a) corresponds to 1 μm. (a) XMCD contrast image of the sample before laser exposure recorded at Co L_3 edge. The solid circles denote a magnetically blocked particle "1", while the two dashed circles highlight nanoparticles, that exhibit no or no stable contrast over the experimental sequence. (b)-(k) Sequence of magnetic contrast maps, each recorded after exposure to a single laser pulse. The inset with arrows depicts magnetic contrast variation depending on the in-plane magnetization orientation.

vealed even stronger additional peak than in Fig. 6.5 at 782 eV next to Co L_3 edge, [cf. Fig. 6.8(a), red curve], indicating a change in the chemical state of the particles. We have compared the resulting spectrum to the metallic state before laser experiment [cf. Fig. 6.8(a), blue curve]. As a reference, we have added a cobalt oxide spectrum from *in situ* cobalt oxidation experiment discussed in Chapter 5, where nanoparticles were dosed with 2 L of oxygen that caused a formation of 12 Å of oxide layer. A similar peak at 782 eV is visible [cf. Fig. 6.8(b)], but a shoulder at 779 eV is present. This shoulder is not observed however for the nanoparticles XA spectrum in Fig. 6.8(a). Instead, cobalt carbide [cf. Fig. 6.8(c)] exhibits a characteristic peak at 782 eV, but no shoulder at 779 eV. To prove that the chemical reaction does not come from the native oxide layer on Si substrate, we will use a different sample design, described below.

Overall sample surface does not look damaged after many laser pulses as was confirmed with SEM of the sample [cf. Fig. 6.8(d)]. A small dark spot in the middle of the image corresponds to carbon deposition due to SEM. The rest of the area was not exposed to the laser. SEM revealed no sign for nanoparticles damage such as ablation of the substrate or melting of the nanoparticles. The particles themselves are not visible in Fig. 6.8 due to the resolution but a few examples of particles, exposed to the laser are given in panels (e) and

(f) in Fig. 6.8. The particles presented in panels (g) and (h) were not exposed to the laser. For comparison, in Fig. 6.8(i), an SEM image after static heating of cobalt nanoparticles produced in the same ACIS and heated to 800 K, is presented. Static heating causes structural changes on the surface of the sample. There nanoparticles become rectangular and establish an epitaxial relationship with the substrate [cf. Fig. 6.8(j)-(k)].

All higher fluences reveal similar behavior but even more drastic for all polarizations. The lack of magnetic contrast of the particles does not indicate that the detection is not possible for example due to too thick oxide shell. On the contrary, a few nanoparticles still have a detectable magnetic contrast. And since all of the particles have a similar oxidation/carbonization state proven with XA spectroscopy, the lack of magnetic contrast in some of the particles arises due to the change in magnetic energy barriers in many of the nanoparticles.

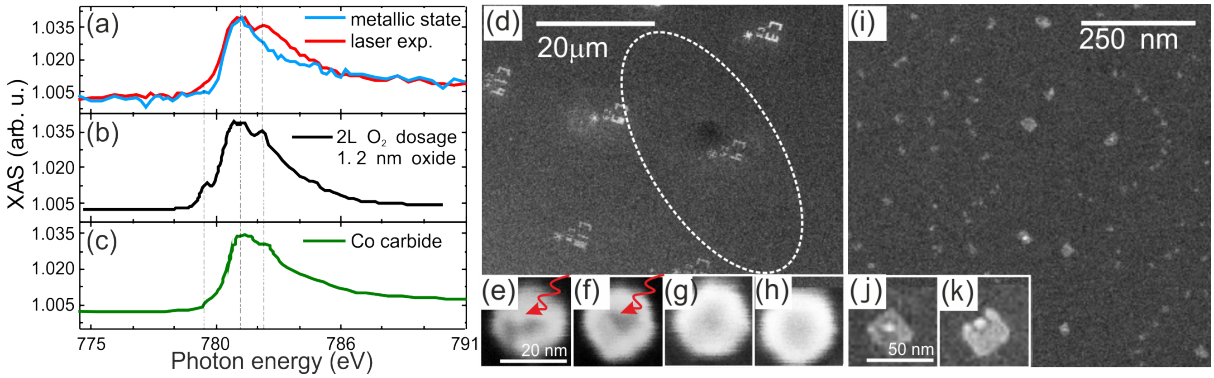

Figure 6.8: (a) XA spectra of the nanoparticles before (blue line) and after high intensity laser excitation (red line). For comparison, panel (b) shows XA spectrum of cobalt nanoparticles upon controlled *in situ* oxidation with molecular oxygen (cf. Chapter 5) and on the panel (c) XA spectrum of cobalt carbide nanoparticles [97] is depicted. Dashed lines indicate the characteristic peaks of the plots at 779, 781 and 782 eV. (d) SEM image of the sample after laser exposure. The white ellipse highlights the laser spot. Nanoparticles are not visible at this scale. The insets represent enlarged SEM images of individual nanoparticles after laser exposure (e,f) and unexposed ones (g,h). For comparison, (i) shows an SEM image of cobalt nanoparticles after static heating to 800 K. Nanoparticles alloy with Si(100) and get rectangular shape as shown in the insets (j) and (k).

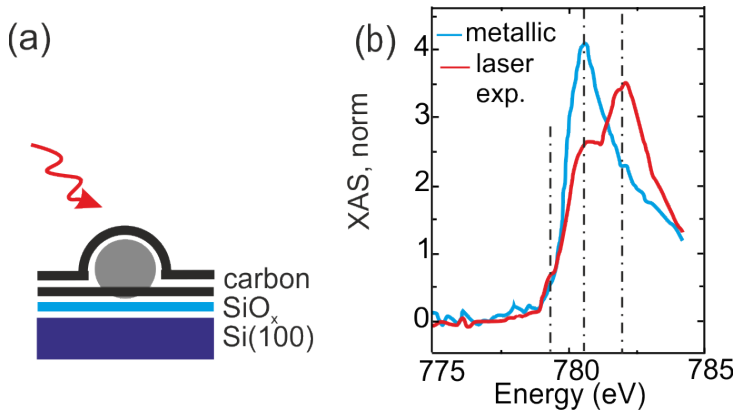

Figure 6.9: (a) Schematic view of the modified sample design: fcc cobalt nanoparticles with sizes ranging from 8 to 20 nm (grey) circle, Si(100) wafer (violet) with a native oxide layer (blue), and the amorphous carbon films with a thickness of 1 – 2 nm (black). (b) XA spectra of the sample before (blue line) and after high intensity laser excitation (red line). For comparison, black line shows XA spectra of cobalt nanoparticles upon controlled *in situ* oxidation with molecular oxygen (cf. Chapter 5).

6.1.4 Second sample design

In order to avoid possible oxidation of the nanoparticles from the native oxide layer on the Si wafer, which was in a direct contact with the nanoparticles [cf. Fig. 6.1(a)], the second sample design was used [cf. Fig. 6.9(a)]. The second sample was covered with amorphous carbon prior to the deposition of the nanoparticles. The rest of the the deposition process was exactly similar to the first sample. Then, a similar experiment as described before in Section 6.1 was performed. The new sample design was chosen to avoid cobalt oxidation after high fluence laser pulses, but still some chemical reaction occurred, as evidenced by XAS [cf. Fig. 6.9(b)]. No deterministic switching of magnetically blocked nanoparticles occurred and an additional peak in the spectrum was detected with XA spectroscopy around 782 eV, possibly, due to the reaction with amorphous carbon at the substrate/nanoparticle interface. To investigate the effect of sample heating in more detail, some calculations were performed (cf. discussion).

6.2 Discussion

In the experiment discussed above, we have collected magnetic contrast data of more then 500 nanoparticles before and after excitation with single 50-fs laser pulses of increasing intensities (for low intensity case cf. Tab. 6.2). Single laser pulse series revealed no

deterministic magnetization switching for individual cobalt nanoparticles for all fluences between 1 and 21 mJ/cm^2 for linear, σ_+ and σ_- laser polarization. Laser fluences higher than 4 mJ/cm^2 induced chemical modification of the nanoparticles confirmed with XA spectroscopy [feature at 781-782 eV in Figs. 6.5, 6.8(a) and 6.9(b)]. For less then 12 % of the particles, low intensity laser excitation resulted with reduction or loosing of magnetic contrast. There are few possible reasons why a chemical reaction of cobalt could take place. First, the laser pulse energy absorbed by the sample heats it up significantly and causes a reaction between cobalt nanoparticles and neighboring carbon/oxygen atoms. It is not clear, which part of the sample heats the most: cobalt, carbon or silicon. Second, laser pulses could destroy the carbon protection layer and chemical modification is caused by oxidation from residual gas in the XPEEM chamber.

In this section, we will estimate the temperature increase in the sample from simple considerations for 150 nJ (9 mJ/cm^2) fluence, the first one from the high fluence series. The temperature estimation will answer several questions. First, along with the discussion in the introduction for this Chapter, we want to address the probability of stochastic thermal switches (1.a). Higher temperature promotes more rapid switching according to Arrhenius law. Second, structural changes caused in cobalt nanoparticles upon moderate laser heating may affect overall magnetic anisotropy and therefore magnetization stability of the nanoparticles (1.b). Third, temperature estimation will answer the question, which part of the sample heats the most and whether the chemical reaction occurs between cobalt and carbon or oxygen (1.c). Fourth, we would like to determine, if the temperature of the nanoparticle reaches the T_C of cobalt, the necessary condition for inverse Faraday effect and the switching due to the momentum transfer (2.a and 2.b).

6.2.1 Temperature increase due to absorption of laser pulses

Isolated nanoparticles

In order to estimate the temperature increase of the sample caused by the single laser pulse, we will start with a simple model of equilibrium heat transfer between photons, electrons and lattice. First, we will assume **isolated nanoparticles** without heat transfer between particles and substrate/coating layer. At the beginning, the absorbed photons excite electrons and by electron-electron scattering the electron system thermalize. Then the energy is transferred from electrons through electron-phonon interactions to the lattice (without losses). The number of absorbed photons in an isolated cobalt nanoparticle can be estimated by considering the (peak) photon density on the surface $n_{ph} = \mathcal{F}_0/E_{ph}$ (cf. Tab. 6.1) and the effect of Rayleigh scattering from a spherical particle, which is

important in the present case, since the nanoparticle diameters are much smaller when compared to the exciting laser wavelength. Assuming a spherical shape for the nanoparticles, the total absorption cross section is given by $\sigma_{abs} = \frac{3}{\lambda}\frac{\pi^2\varepsilon'' D^3}{(\varepsilon'+2)^2+\varepsilon''^2}$, where ε'= -17.75 and $\varepsilon'' = 25.19$ are the real and imaginary parts of the dielectric constant of cobalt at laser wavelength λ = 800 nm, and D is the particle diameter [98]. The number of absorbed photons is then given by

$$N_{abs} = \sigma_{abs} n_{ph}. \tag{6.1}$$

Absorption of photons results in a temperature increase of $\Delta T = 6\mathcal{F}_0\sigma_{abs}/\pi C_p \varrho D^3$, where $\mathcal{F}_0$ is the laser fluence, C_p=0.42 J/(g· K) is cobalt heat capacity, and ϱ=8900 kg/m^3 is the density of fcc cobalt (cf. Tab. 6.3). It is noteworthy that the temperature rise does not depend on the nanoparticles diameter but only on laser fluence since D^3 term cancels out: $\Delta T \sim \mathcal{F}_0\sigma_{abs}/D^3 \sim \mathcal{F}_0 D^3/D^3 = \mathcal{F}_0$. Respective temperature increase of the electron gas system can be similarly derived: $\Delta T_e = (\mathcal{F}_0 \cdot \sigma_{abs})/C_V \cdot m_{particle}$, where C_V=52 J/(kg · K) is the electron gas heat capacity at 300 K derived from the linear temperature dependence of the electron gas heat capacity $C_V = \gamma T$ where γ_{Co}=4.38 mJ/(mol · K^2) and M_{Co}=58900 kg/mol [99] is the molar mass of cobalt.

	d	ρ	C_p	λ	n	k
	nm	10^3 kg m^{-3}	J· kg^{-1} K^{-1}	W·m^{-1}K^{-1}		
Co	10	8.90	420	69.21-100[a,b]	2.56	4.92
$\alpha-$C	3	2.00[c]	900[d]	∼1.0[e]	2.24	0.80
SiOx	2	2.21	840	1.2[f]	1.45	0.00
Si	∞	2.32	712	130	3.69	0.01

a Ref. [100], b Ref. [101], c Ref. [102], d Ref. [103], e Ref. [104], f Ref. [105].

Table 6.3: Parameters used for simulating the temperature increase in the system depicted in Fig. 6.9(a): d - diameter/thikness of the layer, material's density ρ, heat capacity C_p, thermal conductivity λ, refractive index n and extinction coefficient k.

At 9 mJ/cm^2 photon fluence, the number of absorbed photons in the nanoparticles with 10 nm diameter is estimated to about 700 photons. The temperature rise of the electron gas and the full system as a dependence on laser fluence are shown in Fig. 6.10. The electron gas temperature increases by about 970 K, which would mean that the final electron gas temperature would reach of about 1270 K, which is lower than the T_C of bulk cobalt (1390 K). Although the electron gas temperature increases sufficiently,

the lattice does not heat up as considerably. In the Fig. 6.10 the full system (electrons and lattice) temperature is shown with the red line and a respective axis on the right of the panel. The total, temperature increase for 150 nJ (9 mJ/cm^2) is 50 K, which would mean that the system will reach an insufficient temperature for thermal expansion of the crystal. Indeed, Rayleigh scattering significantly reduce the amount of absorbed energy and therefore the heating of the nanoparticles. Assuming no thermal contact of the particle with the substrate, the particle can potentially stay at 350 K temperature for a long time.

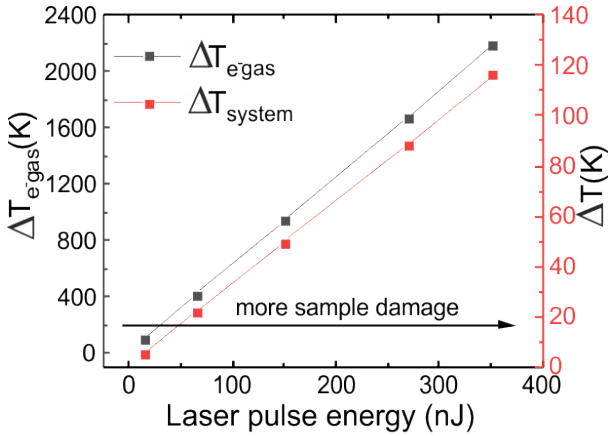

Figure 6.10: Temperature increase of the electron gas (left axis) and the full system (right axis) as a function of laser pulse energy.

Since the full system temperature is far below the T_C of cobalt, all-optical magnetization switching is not possible (2.a and 2.b). Nevertheless, final temperature of the electrons could be sufficient to drive stochastic magnetization reversal process (1.a). The magnetic relaxation time depends on the temperature according to Arrhenius law: $\tau_m = \frac{1}{\nu_0} e^{\frac{E_m}{kT}}$, where E_m is magnetic energy barrier of the particle, k is Boltzman's constant, T is a temperature, ν_0 is switching probability which depends on crystal symmetry and material and equals 1.9 $10^9 s^{-1}$ for fcc cobalt at room temperature. Increasing the temperature of the full system should result in an increase of the switching rate. For E_m = 0.63 eV [11] and T=350 K, we can estimate τ_r= 0.69 s whereas for 300 K this value is 20 s. Thus, if the particles would be thermally isolated from the substrate, and all the heat effectively conserves in the particles, we could indeed expect an enhanced (observable) switching rate in our experiments, and therefore no observable magnetic contrast in XPEEM due to rapid magnetization fluctuation $\tau_m < \tau_x^{short}$. Indeed, we do see a considerable loss of magnetic contrast in the high intensity experiment. However, we see that the particle "3" in Fig. 6.4 shows more or less the same rate of fluctuations

before and after the laser pulses. We also see a change in the XAS of the particles which suggests an interaction to the substrate. Therefore, a heat diffusion between the particles and the substrate has to be taken into account.

Heat diffusion between nanoparticles and substrate/carbon layer

Eventually, the heat diffusion between the nanoparticles and the substrate/capping layer has to be considered. The calculation was performed similarly to [106]. We used a sample stack as depicted in Fig. 6.9(a) with thicknesses denoted in Tab. 6.3. Here we consider the stack without nanoparticles assuming low laser energy absorption on the particles. To estimate the temperature profile created upon laser energy in the multilayer, the differential absorptance dA was calculated using a matrix formalism of the light scattering at the different interfaces and the light propagation inside the layers based on Abeles's formulas [106]. Neglecting any heat diffusion, the laser-induced temperature increase is simply given by $\Delta T = \mathcal{F}_0 dA/(\rho C_p)$, where $\mathcal{F}_0$ is the incoming laser fluence, ρ is the density, and C_p is the heat capacity (cf. Tab. 6.3). Calculating the heat profile upon absorption of the laser pulse with 150 nJ energy (cf.Tab.6.1) shows that the maximal temperature of the sample is reached in the carbon capping layer. Fig. 6.11 shows the temperature distribution in the sample after the laser pulse. The maximal temperature of carbon layer is 770 K. Photons interact with the substrate much stronger than with the nanoparticles because of negligible Rayleigh scattering on the substrate. The heat diffuses later to the particles via thermal conductivity.

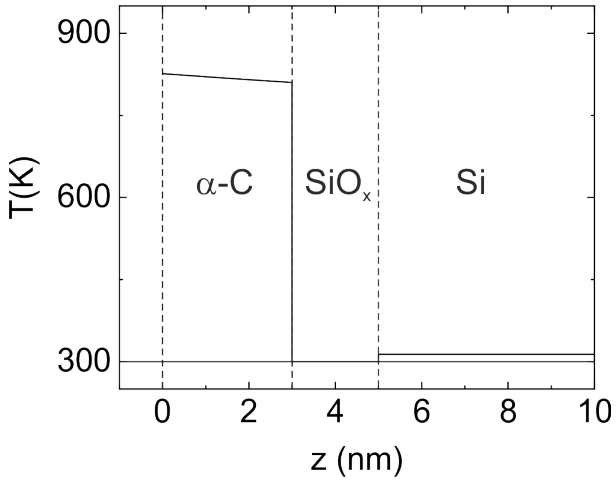

Figure 6.11: Temperature profile within the sample (without nanoparticles) calculated for 150 nJ and the actual experimental geometry using the values in Tab. 6.3.

.

The calculated heat profile in the sample is then used in the time dependent heat

diffusion distribution calculation performed by S. Ruta with COMSOL software. The results of this simulation are presented in Fig. 6.12. The SiO_x layer due to its low thermal conductivity, acts as a thermal barrier between the carbon layer and the substrate. This enables an efficient heat transfer to the cobalt nanoparticles, leading to the temperature increase to ΔT=160 K. The calculation has been performed for 100 K base temperature. If we assume 300 K base temperature, we will end up with 460 K final temperature of the nanoparticles.

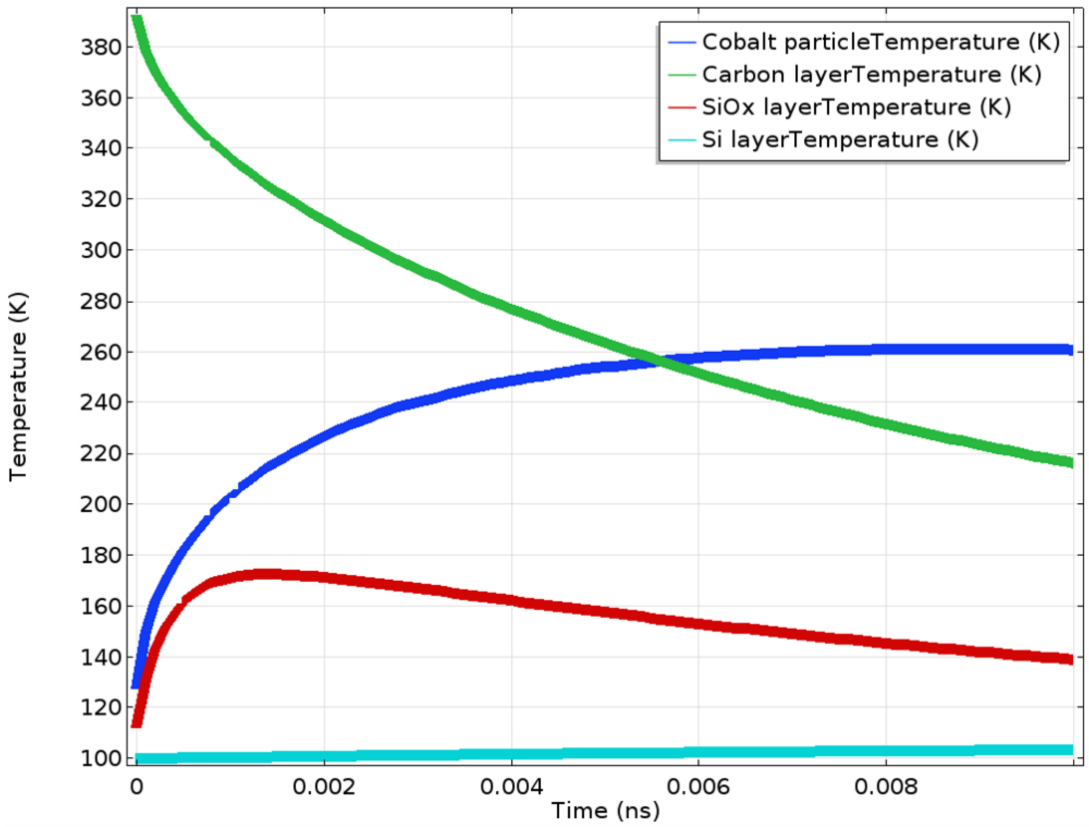

Figure 6.12: Temperature evolution in the sample right after the illumination of the sample with a 150 nJ laser pulse calculated with COMSOL for the actual experimental geometry using the values in Tab. 6.3.

.

COMSOL software also allows us to estimate the time interval when the laser pulse heating will dissipate into Si substrate. After about 100 ps the sample thermalizes to the room temperature.

Although the nanoparticles heat up quite significantly due to heating of carbon, the maximal temperature of cobalt nanoparticles is still well below the T_C and neither of all-optical switching mechanism (2.a) or (2.b) can be expected in the material. However, it is still likely that superparamagnetic stochastic magnetization reversal occurs in the

particles. We will use the calculated temperature of the nanoparticles to estimate the stochastic fluctuation rate for our system.

6.2.2 Stochastic thermal reversal probability

To estimate the switching rate, we can consider that the probability for zero thermal switches $P(0,t)$=exp(-λ), where λ=t/τ_m [cf. eq.(4.46) in [107]] t is time of the experiment and magnetic relaxation time of the particles τ_m was defined in Section 3.2.4, we can derive the switching probability as P(t)=1-$P(0,t)$:

$$P(t) = 1 - e^{\frac{t}{\tau_m}}, \tag{6.2}$$

However, assuming that lattice stay at the increased temperature for about 100 ps and attempt frequency for fcc cobalt 1.9 $\cdot 10^9$ s, τ_m = 400 s, probability that a successful thermal excitation occurs is as low as $5 \cdot 10^{-11}$ according to Eq. 6.2. Summarizing, the probability of stochastic switching is negligibly low and the mechanism described in (1.a) is not realized.

6.2.3 Changes in magnetic anisotropy

Changes in magnetic anisotropy of the particles may cause spin reorientation or altered magnetic energy barrier in cobalt [11]. In our case only for few nanoparticles a laser-induced transition from thermally unstable to magnetically blocked behavior was found after low intensity pulses excitation. Earlier by Kleibert *et.al.* it has been demonstrated that static heating at 470 K can irreversibly transform cobalt nanoparticles from superparamagnetic regime into magnetically blocked state, most likely this is due to temperature-induced lattice relaxation accompanied with a respective change in the magnetic energy barriers [11]. Probably, to induce lattice relaxation, the lattice should be kept at high temperature for a descent period of time which can not be achieved with a single fs laser pulse.

In Figs. 6.6 and 6.6 particle "3" shows stochastic fluctuations without the laser. However, after applying high intensity laser pulse, the switching events stopped to occur. That could happen due to increasing of the magnetic anisotropy of the particle. We can estimate upper and lower boundaries of the magnetic energy barrier for thermally unstable nanoparticles. The particle "3" switches four times in a time interval of 4000 s (measurement time for 10 images, cf. Section 3.2.2). Accordingly, the energy barrier which is required to observe a switching probability of 95% within t = 1000 s at room temperature equals to $E_m > 0.65$ eV. Likewise, one can estimate an upper limit of the magnetic energy

barrier by calculating the minimum value required so that the particle does not switch before 4000 s obtaining $E_m < 0.84$ V. Thus, the actual magnetic energy barrier of the thermally unstable particles can be found in the interval 0.65 eV $< E_m <$ 0.84 eV with a probability of 95%. But unfortunately such approach does not work for estimation of energy boundaries of the magnetically blocked and superparamagnetic nanoparticles. The energy barrier of 0.63 eV for nanoparticle with a switching time t=400 s has been calculated in Ref. [11]. We will use this number in our estimates.

6.2.4 Chemical changes in the nanoparticles

Based on our calculations and on the SEM observations, the chemical modifications of the nanoparticles are likely induced by thermal heating of carbon layer leading to an uptake of carbon or oxygen by the nanoparticles. A chemical reaction of the nanoparticle's surface may result in a reduction of the magnetic volume of the particles and, hence, in an increase of the stochastic fluctuations rate as discussed in Chapter 5. Furthermore, this would also lead to a changing surface anisotropy of the particles and strain effects in the particle. In chapter 5 we show that early oxidation states of cobalt nanoparticles affect magnetic stability of the sample and that changes of XA spectrum happen evenly throughout the sample. The formation of cobalt carbide has been also reported upon heating of cobalt nanoparticles [97].

6.2.5 Altering the Curie temperature of the nanoparticles

In the previous section, we have determined that optical pulse leads mainly to the heating of the carbon layer and the cobalt nanoparticles heat only secondary up to about 460 K which is well below the Curie temperature of the bulk material. Reaching laser-induced all-optical switching would require a significantly stronger heating, but already at existing laser fluences we observe a chemical reaction with the substrate. Another option to reach the Curie temperature with lower laser fluences could be using of particles with lower T_C. According to Ref. [108] the size dependency of T_C of the nanoparticles can be approximated by the following relation:

$$T_c(d) = T_c(\infty)[1 - (d_0/D)^{(1/\nu)}], \tag{6.3}$$

where ν =0.82±0.02 is a scaling exponent, and d_0=0.51±0.02 nm is a microscopic length scale close to the lattice constant. $T_c(\infty)$=1390 K is the Curie temperature for bulk cobalt [65] and D is the diameter of the nanoparticle. Note that Eq. 6.3 is applicable only for diameters larger than d_0. For the size distribution of our sample, T_C does not

significantly deflect from the bulk value of 1390 K as shown in Fig. 6.13. Using Eq. 6.1, the number of absorbed photons for nanoparticles of different diameter can be calculated for 150 nJ laser pulses (9 mJ/cm^2). The upper grid in Fig. 6.13 shows the number of photons absorbed by a nanoparticles depending on its diameter. The inset in Fig. 6.13 details the photon absorption and the T_C for D=1-3 nm. For 9 mJ/cm^2 laser fluence no photons will be absorbed by nanoparticles smaller than 1.5 nm in diameter according to the model described here. However, the magnetic properties of such small particles might be significantly different and very low temperatures are required to stabilize their magnetization.

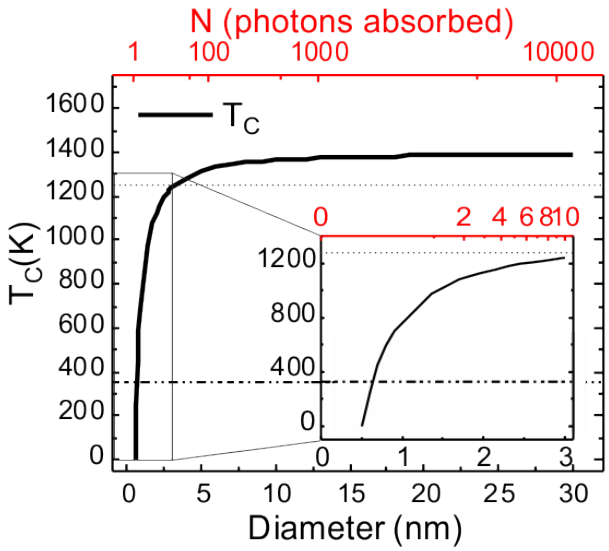

Figure 6.13: Curie temperature as a function of the nanoparticle diameter and the number of photons absorbed at a fluence of 150 nJ/μm^2. The inset shows a close-up look on the T_C dependence for diameters smaller than 3 nm. Dashed and dotted lines show the temperature of the lattice and the electrons, respectively, upon a 150 nJ laser pulse excitation.

According to our estimates, to reach the (nearly bulk-like) Curie temperature of (any diameter) cobalt nanoparticle, laser intensities as high as 11 mJ/cm^2 are required. It can be estimated from the Fig. 6.10, to heat up the electrons from room temperature to 1390 K, ΔT should be 1090 K which is reached at approximately 180 nJ laser pulses. However, already for fluence as high as 9 mJ/cm^2, a chemical modification of nanoparticles is clearly visible (cf. Fig. 6.8) and thus, in addition to the expected chemical modifications.

Alternatively, reduction of T_C of the nanoparticles can be achieved by alloying nanoparticles with noble metals (e.g. Au or Ag) or the choice of a suitable other material with lower T_c might be considered (GdFeCo, LSMO). Another option of reducing T_C is cre-

ating thin disk-like structures of 1-3 atomic layers with strong perpendicular magnetic anisotropy [109]. In all cases, the heat exchange with the substrate needs to be considered, since the latter determines the probability of additional thermal reversals after the laser pulse. Cooling down the sample may be considered to avoid strong overheating of the medium. Alternatively, nanoparticles produced of materials with low T_C like GdFeCo,LSMO or YIG [110] with the T_C in the range of 300-600 K might be used. Finally, a multiple laser pulse regime can be exploited to reach deterministic switching similar to the case of FePt granular medium.

A stochastic thermal driven magnetization reversal mechanism can be considered. For that mechanism realization, the nanoparticles have to stay at higher temperature for a longer period of time. These results suggest that either longer laser pulses or thermal isolation of nanoparticles should be considered.

Small nanoparticles do not absorb enough photons due to Rayleigh scattering. To avoid it, a design of special matrix materials or plasmonic enhancement are required to achieve laser-induced switching in individual nanoparticles.

6.3 Conclusions

In this work, we address the effect of single fs laser pulses on the magnetization of individual cobalt nanoparticles. We show that 800 nm pulses with fluences up to 21 mJ/cm^2 do not deterministically reverse the magnetization of the nanoparticles for all laser polarizations. The cobalt nanoparticles absorb only a small fraction of photons due to the Rayleigh scattering effect. Already for laser excitation with small fluences a transition of a number of initially magnetically blocked nanoparticles to a superparamagnetic state is observed.

Starting from laser pulses with a fluence of 9 mJ/cm^2, an irreversible loss of the XMCD contrast in an increasing fraction of nanoparticles is observed after each pulse. Based on the total absorption cross section we estimate that the electronic system under these conditions heats up to 1270 K, while the equilibrium temperature of nanoparticles increases only to 350 K, if no thermal contact with the substrate is assumed. We assign the absence of laser-induced switching to this estimate, namely that the system temperature increase is below the T_C=1390 K of cobalt. However, estimating the temperature increase of the substrate due to laser pulses, we show that the carbon capping layer heats up to 770 K. Further, using time dependent heat diffusion calculations, we show that the cobalt nanoparticles heat up to 460 K due to heat transfer from the carbon capping

layer. Further heat diffusion lead to thermalization with the remaining substrate at base temperature after approximately 100 ps. This heat dissipation is too fast to result in a stochastic, thermally induced magnetization reversal of the cobalt nanoparticles. XA spectra reveal that the loss of magnetic contrast is involved with a chemical reaction towards cobalt oxide or cobalt carbide. In case of laser excitation, the chemical reaction might be promoted by the temperature increase in the carbon layer.

Our results suggest that either longer laser pulses (nanoseconds) or nanoparticles with lower T_C or the design of special matrix materials or plasmonic enhancement by means of dedicated structures used as nano antennas are required to reach laser-induced single pulse magnetization switching in individual nanoparticles. For example, low T_C materials such as GdFeCo, LSMO or YIG might be considered [110].

Chapter 7

Summary

In this work, we use a combination of characterization techniques in order to directly correlate magnetic properties, crystal structure and morphology of the very same individual cobalt nanoparticles with the size ranging between 8 and 25 nm. We use XPEEM, employing XMCD effect and XA spectroscopy for magnetic and chemical characterization and HAADF-STEM for atomic resolution structural characterization of cobalt nanoparticles, cobalt nanoparticles upon *in situ* oxidation and upon fs laser exposure.

Using XPEEM, we directly correlate the orientation of the magnetization in individual cobalt nanoparticles with their crystallographic axes, morphology and defects. Our data shows that the nanoparticles have a narrow size distribution with a mean size of 13±2 nm and an aspect ratio close to 1. More than 40% of the nanoparticles are magnetically blocked with a relaxation time $\tau_m > 400$ s at 100 K which suggests an enhanced magnetic anisotropy when compared to the respective bulk property. The magnetic blocking of the nearly spherical particles occurs independently of the particle size. The HAADF-STEM suggests fcc structure for most of the particles. However detailed structural characterizations requires a 3D STEM investigations in order to confirm the crystal structure. The data show that the magnetization orientation in individual nanoparticles is not correlated with the crystal structure of the particles. This suggests a more complex internal structure of each of the particles individually and a role of defects in magnetization orientation. For the elongated nanoparticles and agglomerates, we find that shape anisotropy dominates over the other contributions and the magnetization is aligned parallel to the long axis of the particles. For a spherical nanoparticles with stacking faults, the magnetization direction is aligned nearly parallel to the [111] axis which is a hard axis of bulk fcc cobalt, and thus, implies a significant impact of the staking faults on the magnetic anisotropy of the nanoparticles. Our structural investigations show that many particles have structural defects that modify magnetic anisotropy. We created an atomistic model

of the particle with stacking faults, which was successfully used to reproduce the experimental HAADF-STEM images proving the presence and position of these stacking faults in the crystal. The model shall be used for atomistic spin modelling in order to reveal the role of the defects in magnetization stability.

Further, we address the early stages of oxidation. Our results show that cobalt oxide forms a closed inhomogeneous shell around the metallic core already at dosages as low as 1 L where the XA spectrum does not differ much from the metallic spectrum. With intermediate dosage, the oxide shell becomes more dense and XA spectrum becomes more similar to the CoO spectrum. Vanishing of magnetic contrast for some of the nanoparticles occurs due to the shrinking of the magnetic core volume, which lowers the magnetic anisotropy of the particle and causes the transition to superparamagnetic regime. At intermediate dosages, the magnetic contrast of the nanoparticles can be recovered by cooling to lower temperatures which demonstrates reduced blocking temperature for the oxidized nanoparticles. With the highest dosage, we observe a dense shell of a thickness of 4.5 nm, consisting of CoO and Co_3O_4 and vanishing magnetic contrast for 99% of the nanoparticles which can not be recovered with cooling. Our data suggests that the orientation of the easy axis of the nanoparticles does not change after the oxidation. We have fitted a core/shell model based on reference spectra to the XA spectra to estimate the oxide shell thickness forming on the nanoparticles. Our HAADF-STEM data suggests that the fits to XA spectra significantly underestimate the shell thickness due to a complicated oxidation kinetics.

Finally, we address the effect of fs laser pulse excitation on cobalt nanoparticles. No deterministic switching is found independently on laser fluence and polarization. We find that the absorption of the laser pulses is inefficient due to Rayleigh scattering. Nevertheless, photon absorption leads to gradual chemical reaction of the particles with the substrate. The reason for that is strong heating of the amorphous carbon protection layer. The resulting temperature increase in the particles is not enough to reach the Curie temperature of the material which is crucial for all-optical switching. We did also not observe laser-induced thermal fluctuations of the magnetization of the particles which is due to the low attempt frequency of fcc cobalt. Increasing the pulse energy leads to a progressing chemical reaction. Our results show the limitations of ultrafast pulse manipulation of the nanoparticles and suggest using nanoparticles with lower T_C to achieve laser-induced switching in nanoparticles. The lower T_C can be reached either by using nanoparticles with smaller diameters or selecting different materials such as GdFeCo.

7.1 Future prospects

Advanced technology strives for faster, tinier and cheaper devices. One of the current challenges in magnetism is to achieve fast energy-saving switching of the smaller structures, a question interesting both for technology and research. For applications, the required nanomagnets should have controlled and predictable properties, with reversible and deterministic behavior, and, low dimensions. At the nanoscale, the magnetic properties of objects can differ from the bulk specimen due to high impact of structure inhomogeneities, strain and chemical composition on magnetic anisotropy.

Our results show that structural defects are important for magnetic properties of cobalt nanoparticles especially for stability of their magnetization and its orientation. The structural defects can promote a complex spin arrangement in the materials such as vortex structures observed in the vicinity of screw and edge dislocations of thin films. Therefore, theoretical calculations of the magnetic properties of nanoparticles including the role of the defects are needed. The complex oxidation kinetics in cobalt nanoparticles might help to better understand magnetic and chemical properties of cobalt oxide shell-metallic cobalt core nanoparticles. In particular, the cobalt oxide phases present in the oxide shell might be the key to understand the exchange bias effect in these structures as well as the chemical reactions in important catalytic processes such as the Fischer-Tropsch synthesis. Furthermore, our data urgently call for pushing the spatial resolution and sensitivity of soft x-ray magnetic microscopy to directly address the role of structural defects on the local magnetic structure of individual nanoparticles. A promising pathway towards this goal could be the development of soft x-ray ptychography with nanometer resolution. Finally, we propose that applying nanoparticles with lower T_C might present a feasible route towards achieving of laser-induced switching in isolated nanomagnets.

Appendix A

Sample preparation

A.1 Pt markers deposition

For Pt marker structure deposition, the TEM-compatible substrate with nine membranes was mounted on special sample holder from Ted Pella Inc. [cf. Fig. A.1], compatible with focused ion beam (FIB) microscope. Then the membranes were transferred to a scanning electron microscope (SEM) with FIB functionality (Zeiss NVision). The FIB microscope is started with 15 kV "high tension", in-Lens detector and 3 mm working distance are used to acquire the image.

Then Pt evaporator was degassed according to a standard procedure for Pt deposition. Than a number of marker structures were deposited by thermal decomposition of Pt precursor molecules with help of electron beam on the membranes. The Pt markers were deposited in two sizes. For 2×2 μm^2 squares, the Pt was deposited for 30 s with low scanning speed (#8 in the software). For the deposition of 200×200 nm^2 markers, a low deposition speed (#8 in the software) for 7 s was used. Deposition of markers in a unique arrangement for each membranes allowed faster and unambiguous orientation on the sample.

Figure A.1: SEM and FIB-compatible membrane sample holder [111].

A.2 Substrate annealing for nanoparticles deposition

The silicon substrate was mounted on the XPEEM-compatible sample holder with a heating coil and Pt100 temperature sensor and inserted to the preparation system (PS) at SIM beam line. In the PS, the sample was mounted on the manipulator where a current was applied to the heating coil of the sample holder whereas the temperature was monitored from the multimeter connected to the Pt100 contacts. The current applied to the heating coil was increased gradually, by monitoring the pressure in the PS not to overcome $5{\cdot}10^{-7}$ mbar. The table of time, currents, temperature of the substrate and the pressure in the PS is listed in Tab. A.1.

t, min	I, A	R, Ω	T, C°	p_{PS}, mbar
0	0	127.6	20	$5.9{\cdot}10^{-9}$
5	0.2	127.7	-	$6.09{\cdot}10^{-9}$
10	0.4	129.7	-	$7.46{\cdot}10^{-9}$
15	0.6	134.7	-	$1.43{\cdot}10^{-8}$
20	0.8	139.9	-	$2.04{\cdot}10^{-8}$
25	1	147.9	-	$3.62{\cdot}10^{-8}$
30	1.2	158.9	-	$5.93{\cdot}10^{-8}$
35	1.4	173.5	140	$1.31{\cdot}10^{-7}$
40	1.6	174	-	$1.5{\cdot}10^{-7}$
45	1.8	186.3	-	$1.67{\cdot}10^{-7}$
50	2.0	200	-	$1.93{\cdot}10^{-7}$
55	2.0	208.7	240	$2.08{\cdot}10^{-7}$

Table A.1: Substrate annealing procedure. t - time of the annealing, I - current, applied to the heating coil, R - resistance of the Pt100, T - temperature estimated from [112], p_{PS} - pressure in the PS.

For TEM-compatible substrate the maximum temperature for annealing was 120°C in order to protect the membranes. For that, the maximum current in the coil was kept at 1.2 A.

Bibliography

[1] S. A. Majetich, T. Wen, and O. T. Mefford, "Magnetic nanoparticles," *MRS Bulletin*, vol. 38, no. 11, pp. 899–903, 2013. DOI 10.1557/mrs.2013.230.

[2] A. Aharoni and R. Aharoni, *Introduction to the Theory of Ferromagnetism*. Oxford University Press, 2000. ISBN 9780198508083.

[3] J. Wang, H. Duan, X. Lin, V. Aguilar, A. Mosqueda, and G.-M. Zhao, "Temperature dependence of magnetic anisotropy constant in iron chalcogenide Fe_3Se_4: Excellent agreement with theories," *Journal of Applied Physics*, vol. 112, no. 10, p. 103905, 2012. DOI 10.1063/1.4759352.

[4] S. Rohart, V. Repain, A. Tejeda, P. Ohresser, F. Scheurer, P. Bencok, J. Ferré, and S. Rousset, "Distribution of the magnetic anisotropy energy of an array of self-ordered Co nanodots deposited on vicinal Au(111): X-ray magnetic circular dichroism measurements and theory," *Phys. Rev. B*, vol. 73, p. 165412, Apr 2006. DOI 10.1103/PhysRevB.73.165412.

[5] S. Oyarzun, A. Tamion, F. Tournus, V. Dupuis, and M. Hillenkamp, "Size effects in the magnetic anisotropy of embedded cobalt nanoparticles: from shape to surface," *Sci. Rep.*, vol. 5, p. 14749, 2015. DOI 10.1038/srep14749.

[6] J. P. Chen, C. M. Sorensen, K. J. Klabunde, and G. C. Hadjipanayis, "Magnetic properties of nanophase cobalt particles synthesized in inversed micelles," *Journal of Applied Physics*, vol. 76, no. 10, pp. 6316–6318, 1994. DOI 10.1063/1.358280.

[7] F. Luis, J. M. Torres, L. M. García, J. Bartolomé, J. Stankiewicz, F. Petroff, F. Fettar, J.-L. Maurice, and A. Vaurès, "Enhancement of the magnetic anisotropy of nanometer-sized Co clusters: Influence of the surface and of interparticle interactions," *Phys. Rev. B*, vol. 65, p. 094409, Feb 2002. DOI 10.1103/PhysRevB.65.094409.

[8] R. Morel, A. Brenac, C. Portemont, T. Deutsch, and L. Notin, "Magnetic anisotropy in icosahedral cobalt clusters," *Journal of Magnetism and Magnetic Materials*, vol. 308, no. 2, pp. 296 – 304, 2007. DOI 10.1016/j.jmmm.2006.06.004.

[9] M. Respaud, J. M. Broto, H. Rakoto, A. R. Fert, L. Thomas, B. Barbara, M. Verelst, E. Snoeck, P. Lecante, A. Mosset, J. Osuna, T. O. Ely, C. Amiens, and B. Chaudret, "Surface effects on the magnetic properties of ultrafine cobalt particles," *Phys. Rev. B*, vol. 57, pp. 2925–2935, Feb 1998. DOI 10.1103/PhysRevB.57.2925.

[10] F. Kronast, N. Friedenberger, K. Ollefs, S. Gliga, L. Tati-Bismaths, R. Thies, A. Ney, R. Weber, C. Hassel, F. M. Römer, A. V. Trunova, C. Wirtz, R. Hertel, H. A. Dürr, and M. Farle, "Element-specific magnetic hysteresis of individual 18 nm Fe nanocubes," *Nano Letters*, vol. 11, no. 4, pp. 1710–1715, 2011. DOI 10.1021/nl200242c.

[11] A. Kleibert, A. Balan, R. Yanes, P. M. Derlet, C. A. F. Vaz, M. Timm, A. Fraile Rodríguez, A. Béché, J. Verbeeck, R. S. Dhaka, M. Radovic, U. Nowak, and F. Nolting, "Direct observation of enhanced magnetism in individual size- and shape-selected 3*d* transition metal nanoparticles," *Phys. Rev. B*, vol. 95, p. 195404, May 2017. DOI 10.1103/PhysRevB.95.195404.

[12] A. Balan, P. M. Derlet, A. F. Rodriguez, J. Bansmann, R. Yanes, U. Nowak, A. Kleibert, and F. Nolting, "Direct observation of magnetic metastability in individual iron nanoparticles," *Phys. Rev. Lett.*, vol. 112, no. 10, p. 107201, 2014. DOI 10.1103/PhysRevLett.112.107201.

[13] S. Krause, G. Herzog, T. Stapelfeldt, L. Berbil-Bautista, M. Bode, E. Y. Vedmedenko, and R. Wiesendanger, "Magnetization reversal of nanoscale islands: How size and shape affect the Arrhenius prefactor," *Phys. Rev. Lett.*, vol. 103, p. 127202, Sep 2009. DOI 10.1103/PhysRevLett.103.127202.

[14] M. J. Martínez-Pérez, B. Müller, D. Schwebius, D. Korinski, R. Kleiner, J. Sesé, and D. Koelle, "NanoSQUID magnetometry of individual cobalt nanoparticles grown by focused electron beam induced deposition," *Superconductor Science and Technology*, vol. 30, p. 024003, Dec 2016. DOI 10.1088/0953-2048/30/2/024003.

[15] M. Jamet, V. Dupuis, P. Mélinon, G. Guiraud, A. Pérez, W. Wernsdorfer, A. Traverse, and B. Baguenard, "Structure and magnetism of well defined cobalt nanoparticles embedded in a niobium matrix," *Physical Review B - Condensed Matter and Materials Physics*, vol. 62, no. 1, pp. 493–499, 2000. DOI 10.1103/PhysRevB.62.493.

[16] S. D. Pollard, J. A. Garlow, J. Yu, Z. Wang, Y. Zhu, and H. Yang, "Observation of stable Néel skyrmions in cobalt/palladium multilayers with Lorentz transmission electron microscopy," *Nature Communications*, vol. 8, pp. 14761–14761, 2017. DOI 10.1038/ncomms14761.

[17] M. Varón, M. Beleggia, T. Kasama, R. J. Harrison, R. E. Dunin-Borkowski, V. F. Puntes, and C. Frandsen, "Dipolar magnetism in ordered and disordered low-dimensional nanoparticle assemblies," *Scientific Reports*, vol. 3, p. 1234, 2013. DOI 10.1038/srep01234.

[18] S. Eisebitt, J. Lüning, W. F. Schlotter, M. Lörgen, O. Hellwig, W. Eberhardt, and J. Stöhr, "Lensless imaging of magnetic nanostructures by x-ray spectro-holography," *Nature*, vol. 432, no. 7019, pp. 885–888, 2004. DOI 10.1038/nature03139.

[19] D. J. Vine, G. J. Williams, B. Abbey, M. A. Pfeifer, J. N. Clark, M. D. de Jonge, I. McNulty, A. G. Peele, and K. A. Nugent, "Ptychographic Fresnel coherent diffractive imaging," *Phys. Rev. A*, vol. 80, p. 063823, Dec 2009. DOI 10.1103/PhysRevA.80.063823.

[20] P. A. Midgley and R. E. Dunin-Borkowski, "Electron tomography and holography in materials science," *Nature Materials*, vol. 8, p. 271, 2009. DOI 10.1038/nmat2406.

[21] F. Luis, F. Bartolomé, F. Petroff, J. Bartolomé, L. M. García, C. Deranlot, H. Jaffrès, M. J. Martínez, P. Bencok, F. Wilhelm, A. Rogalev, and N. B. Brookes, "Tuning the magnetic anisotropy of Co nanoparticles by metal capping," *Europhysics Letters (EPL)*, vol. 76, pp. 142–148, oct 2006. DOI 10.1209/epl/i2006-10242-2.

[22] T. Yokoyama, T. Nakagawa, and Y. Takagi, "Magnetic circular dichroism for surface and thin film magnetism: Measurement techniques and surface chemical applications," *International Reviews in Physical Chemistry*, vol. 27, no. 3, pp. 449–505, 2008. DOI 10.1080/01442350802127608.

[23] C. A. F. Vaz, A. Balan, F. Nolting, and A. Kleibert, "*In situ* magnetic and electronic investigation of the early stage oxidation of Fe nanoparticles using x-ray photo-emission electron microscopy," *Phys. Chem. Chem. Phys.*, vol. 16, no. 48, pp. 26624–26630, 2014. DOI 10.1039/C4CP02725F.

[24] Z. Yang, N. Yang, J. Yang, J. Bergström, and M. P. Pileni, "Control of the oxygen and cobalt atoms diffusion through Co nanoparticles differing by their crystalline structure and size," *Advanced Functional Materials*, vol. 25, no. 6, pp. 891–897, 2015. DOI 10.1002/adfm.201403617.

[25] A. Pratt, L. Lari, O. Hovorka, A. Shah, C. Woffinden, S. Tear, C. Binns, and R. Kröger, "Enhanced oxidation of nanoparticles through strain-mediated ionic transport," *Nature Materials*, vol. 13, pp. 26–30, 1 2014. DOI 10.1038/nmat3785.

[26] V. Papaefthimiou, T. Dintzer, V. Dupuis, A. Tamion, F. Tournus, D. Teschner, M. Hävecker, A. Knop-Gericke, R. Schlögl, and S. Zafeiratos, "When a metastable oxide stabilizes at the nanoscale: Wurtzite CoO formation upon dealloying of PtCo nanoparticles," *The Journal of Physical Chemistry Letters*, vol. 2, no. 8, pp. 900–904, 2011. DOI 10.1021/jz2003155.

[27] S. Bartling, M. M. Pohl, K. H. Meiwes-Broer, and I. Barke, "Morphological impact on the reaction kinetics of size-selected cobalt oxide nanoparticles," *J. Chem. Phys.*, vol. 143, no. 11, p. 114301, 2015. DOI 10.1063/1.4930853.

[28] A. V. Kimel, A. Kirilyuk, P. A. Usachev, R. V. Pisarev, A. M. Balbashov, and T. Rasing, "Ultrafast non-thermal control of magnetization by instantaneous photomagnetic pulses," *Nature*, vol. 435, no. 7042, pp. 655–657, 2005. DOI 10.1038/nature03564.

[29] F. Hansteen, A. Kimel, A. Kirilyuk, and T. Rasing, "Femtosecond photomagnetic switching of spins in ferrimagnetic garnet films," *Phys. Rev. Lett.*, vol. 95, p. 047402, Jul 2005. DOI 10.1103/PhysRevLett.95.047402.

[30] J. Hohlfeld, T. Gerrits, M. Bilderbeek, T. Rasing, H. Awano, and N. Ohta, "Fast magnetization reversal of GdFeCo induced by femtosecond laser pulses," *Phys. Rev. B*, vol. 65, p. 012413, Dec 2001. DOI 10.1103/PhysRevB.65.012413.

[31] C. D. Stanciu, F. Hansteen, A. V. Kimel, A. Kirilyuk, A. Tsukamoto, A. Itoh, and T. Rasing, "All-optical magnetic recording with circularly polarized light," *Phys. Rev. Lett.*, vol. 99, p. 047601, Jul 2007. DOI 10.1103/PhysRevLett.99.047601.

[32] S. Alebrand, M. Gottwald, M. Hehn, D. Steil, M. Cinchetti, D. Lacour, E. E. Fullerton, M. Aeschlimann, and S. Mangin, "Light-induced magnetization reversal of high-anisotropy TbCo alloy films," *Applied Physics Letters*, vol. 101, no. 16, p. 162408, 2012. DOI 10.1063/1.4759109.

[33] C.-H. Lambert, S. Mangin, B. S. D. C. S. Varaprasad, Y. K. Takahashi, M. Hehn, M. Cinchetti, G. Malinowski, K. Hono, Y. Fainman, M. Aeschlimann, and E. E. Fullerton, "All-optical control of ferromagnetic thin films and nanostructures," *Science*, vol. 345, no. 6202, pp. 1337–1340, 2014. DOI 10.1126/science.1253493.

[34] A.-M. Balan, *Studying individual magnetic nanoparticles with X-ray PEEM*. PhD thesis, University of Basel, Faculty of Science, Basel, Switzerland, 2014. DOI 10.5451/unibas-006327922.

[35] I. M. Billas, A. Châtelain, and W. A. de Heer, "Magnetism from the atom to the bulk in iron, cobalt, and nickel clusters," *Science*, vol. 265, no. 5179, pp. 1682–1684, 1994. DOI 10.1126/science.265.5179.1682.

[36] S. Sun, C. B. Murray, D. Weller, L. Folks, and A. Moser, "Monodisperse FePt nanoparticles and ferromagnetic FePt nanocrystal superlattices," *Science*, vol. 287, no. 5460, pp. 1989–1992, 2000. DOI 10.1126/science.287.5460.1989.

[37] V. Skumryev, S. Stoyanov, Y. Zhang, G. Hadjipanayis, D. Givord, and J. Nogués, "Beating the superparamagnetic limit with exchange bias," *Nature*, vol. 423, no. 6942, pp. 850–853, 2003. DOI 10.1038/nature01687.

[38] M. Jamet, W. Wernsdorfer, C. Thirion, V. Dupuis, P. Mélinon, A. Pérez, and D. Mailly, "Magnetic anisotropy in single clusters," *Physical Review B*, vol. 69, no. 2, 2004. DOI 10.1103/PhysRevB.69.024401.

[39] D. A. Garanin and H. Kachkachi, "Surface contribution to the anisotropy of magnetic nanoparticles," *Phys Rev Lett*, vol. 90, no. 6, p. 065504, 2003. DOI 10.1103/PhysRevLett.90.065504.

[40] A. Balan, A. Fraile Rodriguez, C. A. F. Vaz, A. Kleibert, and F. Nolting, "Effect of substrate interface on the magnetism of supported iron nanoparticles," *Ultramicroscopy*, vol. 159 Pt 3, pp. 513–519, 2015. DOI 10.1016/j.ultramic.2015.05.008.

[41] O. Kitakami, H. Sato, Y. Shimada, F. Sato, and M. Tanaka, "Size effect on the crystal phase of cobalt fine particles," *Phys. Rev. B*, vol. 56, pp. 13849–13854, Dec 1997. DOI 10.1103/PhysRevB.56.13849.

[42] L. Meziane, C. Salzemann, C. Aubert, H. Gérard, C. Petit, and M. Petit, "Hcp cobalt nanocrystals with high magnetic anisotropy prepared by easy one-pot synthesis," *Nanoscale*, vol. 8, pp. 18640–18645, 2016. DOI 10.1039/C6NR05792F.

[43] S. Sun and C. B. Murray, "Synthesis of monodisperse cobalt nanocrystals and their assembly into magnetic superlattices (invited)," *Journal of Applied Physics*, vol. 85, no. 8, pp. 4325–4330, 1999. DOI 10.1063/1.370357.

[44] V. A. de la Peña O'Shea, P. R. de la Piscina, N. Homs, G. Aromí, and J. L. G. Fierro, "Development of hexagonal closed-packed cobalt nanoparticles stable at high temperature," *Chemistry of Materials*, vol. 21, no. 23, pp. 5637–5643, 2009. DOI 10.1021/cm900845h.

[45] O. V. Yazyev and L. Helm, "Defect-induced magnetism in graphene," *Phys. Rev. B*, vol. 75, p. 125408, Mar 2007. DOI 10.1103/PhysRevB.75.125408.

[46] A. Mayoral, H. Barron, R. Estrada-Salas, A. Vazquez-Duran, and M. Jose-Yacaman, "Nanoparticle stability from the nano to the meso interval," *Nanoscale*, vol. 2, no. 3, pp. 335–342, 2010. DOI 10.1039/b9nr00287a.

[47] L. Berbil-Bautista, S. Krause, M. Bode, A. Badía-Majós, C. de la Fuente, R. Wiesendanger, and J. I. Arnaudas, "Nanoscale spin structures dominated by magnetoelastic interactions around dislocation cores as seen via spin-polarized STM," *Phys. Rev. B*, vol. 80, p. 241408, Dec 2009. DOI 10.1103/PhysRevB.80.241408.

[48] D. Hull and D. J. Bacon, *Introduction to Dislocations (Fifth Edition). Chapter 1 - Defects in Crystals*, pp. 1–20. Oxford: Butterworth-Heinemann, 2011. DOI 10.1016/B978-0-08-096672-4.00001-3.

[49] J. Stöhr and H. C. Siegmann, *Magnetism: from Fundamentals to Nanoscale Dynamics*. Springer-Verlag Berlin Heidelberg, 2006. ISBN 978-3-540-30283-4.

[50] D. Le Roy, R. Morel, S. Pouget, A. Brenac, L. Notin, T. Crozes, and W. Wernsdorfer, "Bistable coupling states measured on single Co nanoclusters deposited on CoO(111)," *Phys. Rev. Lett.*, vol. 107, p. 057204, Jul 2011. DOI 10.1103/PhysRevLett.107.057204.

[51] N. Weiss, T. Cren, M. Epple, S. Rusponi, G. Baudot, S. Rohart, A. Tejeda, V. Repain, S. Rousset, P. Ohresser, F. Scheurer, P. Bencok, and H. Brune, "Uniform magnetic properties for an ultrahigh-density lattice of noninteracting Co nanostructures," *Phys. Rev. Lett.*, vol. 95, p. 157204, Oct 2005. DOI 10.1103/PhysRevLett.95.157204.

[52] W. Wernsdorfer, C. Thirion, N. Demoncy, H. Pascard, and D. Mailly, "Magnetisation reversal by uniform rotation (Stoner–Wohlfarth model) in fcc cobalt nanoparticles," *Journal of Magnetism and Magnetic Materials*, vol. 242-245, pp. 132 – 138, 2002. DOI 10.1016/S0304-8853(01)01153-2.

[53] L. Néel, "Anisotropie magnétique superficielle et surstructures d'orientation," *J. Phys. Radium.*, vol. 15, no. 376, pp. 225–239, 1954. DOI 10.1051/jphysrad:01954001504022500.

[54] A. Aldea and V. Bârsan, *Trends in Nanophysics*. Springer-Verlag Berlin Heidelberg, 2010. ISBN 978-3-642-12070-1.

[55] C. J. Aas, L. Szunyogh, R. F. L. Evans, and R. W. Chantrell, "Effect of stacking faults on the magnetocrystalline anisotropy of hcp Co: a first-principles study," *Journal of Physics: Condensed Matter*, vol. 25, p. 296006, jul 2013. DOI 10.1088/0953-8984/25/29/296006.

[56] W. F. Brown, "Thermal fluctuations of a single-domain particle," *Physical Review*, vol. 130, no. 5, pp. 1677–1686, 1963. DOI 10.1103/PhysRev.130.1677.

[57] V. Papaefthimiou, T. Dintzer, V. Dupuis, A. Tamion, F. Tournus, D. Teschner, M. Hävecker, A. Knop-Gericke, R. Schlögl, and S. Zafeiratos, "When a metastable oxide stabilizes at the nanoscale: Wurtzite CoO formation upon dealloying of PtCo nanoparticles," *The Journal of Physical Chemistry Letters*, vol. 2, no. 8, pp. 900–904, 2011. DOI 10.1021/jz2003155.

[58] U. Wiedwald, M. Spasova, E. L. Salabas, M. Ulmeanu, M. Farle, Z. Frait, A. F. Rodriguez, D. Arvanitis, N. S. Sobal, M. Hilgendorff, and M. Giersig, "Ratio of orbital-to-spin magnetic moment in Co core-shell nanoparticles," *Phys. Rev. B*, vol. 68, p. 064424, Aug 2003. DOI 10.1103/PhysRevB.68.064424.

[59] J. B. Tracy, D. N. Weiss, D. P. Dinega, and M. G. Bawendi, "Exchange biasing and magnetic properties of partially and fully oxidized colloidal cobalt nanoparticles," *Physical Review B*, vol. 72, no. 6, pp. 64404–64404, 2005. DOI 10.1103/PhysRevB.72.064404.

[60] A. M. Hibberd, H. Q. Doan, E. N. Glass, F. M. F. de Groot, C. L. Hill, and T. Cuk, "Co polyoxometalates and a Co_3O_4 thin film investigated by *L*-edge x-ray absorption spectroscopy," *The Journal of Physical Chemistry C*, vol. 119, no. 8, pp. 4173–4179, 2015. DOI 10.1021/jp5124037.

[61] P. Dutta, M. S. Seehra, S. Thota, and J. Kumar, "A comparative study of the magnetic properties of bulk and nanocrystalline Co_3O_4," *Journal of Physics: Condensed Matter*, vol. 20, p. 015218, dec 2007. DOI 10.1088/0953-8984/20/01/015218.

[62] Y. Wang, H. Y. Zou, and C. Z. Huang, "Real-time monitoring of oxidative etching on single Ag nanocubes via light-scattering dark-field microscopy imaging," *Nanoscale*, vol. 7, pp. 15209–15213, 2015. DOI 10.1039/C5NR04234H.

[63] U. Wiedwald, K. Fauth, M. Heßler, H.-G. Boyen, F. Weigl, M. Hilgendorff, M. Giersig, G. Schütz, P. Ziemann, and M. Farle, "From colloidal Co/CoO core/shell nanoparticles to arrays of metallic nanomagnets: Surface modification and magnetic properties," *ChemPhysChem*, vol. 6, no. 12, pp. 2522–2526, 2005. DOI 10.1002/cphc.200500148.

[64] M. S. El Hadri, M. Hehn, P. Pirro, C.-H. Lambert, G. Malinowski, E. E. Fullerton, and S. Mangin, "Domain size criterion for the observation of all-optical helicity-dependent switching in magnetic thin films," *Phys. Rev. B*, vol. 94, p. 064419, Aug 2016. DOI 10.1103/PhysRevB.94.064419.

[65] J. Crangle, "LIX. The magnetic moments of cobalt-copper alloys," *The London, Edinburgh, and Dublin Philosophical Magazine and Journal of Science*, vol. 46, no. 376, pp. 499–513, 1955. DOI 10.1080/14786440508520586.

[66] "Simpore inc. website," 2018. www.simpore.com.

[67] J. Bansmann, A. Kleibert, F. Bulut, M. Getzlaff, P. Imperia, B. C., and K.-H. Meiwes-Broer, "Temperature dependent magnetic spin and orbital moments of mass-filtered cobalt clusters on Au(111)," *Eur. Phys. J. D*, vol. 45, pp. 521–528, 2007. DOI 10.1016/j.ultramic.2016.06.003.

[68] A. Kleibert, J. Passig, K.-H. Meiwes-Broer, M. Getzlaff, and J. Bansmann, "Structure and magnetic moments of mass-filtered deposited nanoparticles," *Journal of Applied Physics*, vol. 101, no. 11, p. 114318, 2007. DOI 10.1063/1.2745330.

[69] H. Haberland, Z. Insepov, and M. Moseler, "Molecular-dynamics simulation of thin-film growth by energetic cluster impact," *Phys. Rev. B*, vol. 51, pp. 11061–11067, Apr 1995. DOI 10.1103/PhysRevB.51.11061.

[70] V. N. Popok, I. Barke, E. E. Campbell, and K.-H. Meiwes-Broer, "Cluster–surface interaction: From soft landing to implantation," *Surface Science Reports*, vol. 66, no. 10, pp. 347–377, 2011. DOI 10.1016/j.surfrep.2011.05.002.

[71] L. Le Guyader, A. Kleibert, A. Fraile Rodríguez, S. El Moussaoui, A. Balan, M. Buzzi, J. Raabe, and F. Nolting, "Studying nanomagnets and magnetic heterostructures with x-ray PEEM at the Swiss Light Source," *Journal of Electron Spectroscopy and Related Phenomena*, vol. 185, no. 10, pp. 371–380, 2012. DOI 10.1016/j.elspec.2012.03.001.

[72] U. Flechsig, F. Nolting, A. Fraile Rodríguez, J. Krempaský, C. Quitmann, T. Schmidt, S. Spielmann, and D. Zimoch, "Performance measurements at the SLS SIM beamline," *AIP Conference Proceedings*, vol. 1234, no. 1, pp. 319–322, 2010. DOI 10.1063/1.3463200.

[73] P. Willmott, *An Introduction to Synchrotron Radiation: Techniques and Applications*. John Wiley & Sons, 2011. DOI 10.1002/9781119970958.

[74] E. Beaurepaire, H. Bulou, L. Joly, and F. Scheurer, *Magnetism and Synchrotron Radiation: Towards the Fourth Generation Light Sources, Proceedings of the 6th International School "Synchrotron Radiation and Magnetism" Mittelwihr (France)*. Springer, 2012. ISBN 978-3319030319.

[75] "Swiss Light Source webpage." www.psi.ch.

[76] J. Vijayakumar, *Artificial multiferroic heterostructures: magnetoelectric coupling and dynamics*. PhD thesis, University of Basel , Faculty of Science, Basel, Switzerland, 2019. DOI 10.5451/unibas-007094476.

[77] J. Stöhr, *NEXAFS Spectroscopy*. Springer-Verlag, Heidelberg, 1996. DOI 10.1007/978-3-662-02853-7.

[78] S. J. Pennycook and P. D. Nellist, *Scanning Transmission Electron Microscopy*. Springer, New York, NY, 2011. DOI 10.1007/978-1-4419-7200-2.

[79] C. T. Chen, Y. U. Idzerda, H.-J. Lin, N. V. Smith, G. Meigs, E. Chaban, G. H. Ho, E. Pellegrin, and F. Sette, "Experimental confirmation of the x-ray magnetic circular dichroism sum rules for iron and cobalt," *Phys. Rev. Lett.*, vol. 75, pp. 152–155, Jul 1995. DOI 10.1103/PhysRevLett.75.152.

[80] R. Kohlhaas, P. Duenner, and N. Schmitz-Pranghe, "Uber die Temperaturabhangigkeit der Gitterparameter von Eisen, Kobalt und Nickel im Bereich hoeher Temperaturen," *Zeitschrift fuer Angewandte Physik*, vol. 23, pp. 245–249, 1967.

[81] S. Plimpton, "Fast parallel algorithms for short-range molecular dynamics," *J. Comp. Phys.*, vol. 117, pp. 1–19, 1995. DOI 10.1006/jcph.1995.1039.

[82] G. P. Purja Pun and Y. Mishin, "Embedded-atom potential for hcp and fcc cobalt," *Phys. Rev. B*, vol. 86, p. 134116, Oct 2012. DOI 10.1103/PhysRevB.86.134116.

[83] I. Lobato and D. V. Dyck, "MULTEM: A new multislice program to perform accurate and fast electron diffraction and imaging simulations using graphics processing units with CUDA," *Ultramicroscopy*, vol. 156, pp. 9–17, 2015. DOI 10.1016/j.ultramic.2015.04.016.

[84] I. Lobato, S. Van Aert, and J. Verbeeck, "Progress and new advances in simulating electron microscopy datasets using MULTEM," *Ultramicroscopy*, vol. 168, pp. 17–27, 2016. DOI 10.1016/j.ultramic.2016.06.003.

[85] L. N. Lewis, "Chemical catalysis by colloids and clusters," *Chemical Reviews*, vol. 93, no. 8, pp. 2693–2730, 1993. DOI 10.1021/cr00024a006.

[86] Q. A. Pankhurst, J. Connolly, S. K. Jones, and J. Dobson, "Applications of magnetic nanoparticles in biomedicine. Topical review," *Journal of Physics D: Applied Physics*, vol. 36, no. 13, pp. R167–R167, 2003. DOI 10.1088/0022-3727/36/13/201.

[87] A. N. Shipway, E. Katz, and I. Willner, "Nanoparticle arrays on surfaces for electronic, optical, and sensor applications," *ChemPhysChem*, vol. 1, no. 1, pp. 18–52, 2000. DOI 10.1002/1439-7641.

[88] Y. Yin, R. M. Rioux, C. K. Erdonmez, S. Hughes, G. A. Somorjai, and A. P. Alivisatos, "Formation of hollow nanocrystals through the nanoscale Kirkendall effect," *Science*, vol. 304, no. 5671, pp. 711–714, 2004. DOI 10.1126/science.1096566.

[89] T. J. Regan, H. Ohldag, C. Stamm, F. Nolting, J. Lüning, J. Stöhr, and R. L. White, "Chemical effects at metal/oxide interfaces studied by x-ray-absorption spectroscopy," *Physics Review B*, vol. 64, p. 214422, Dec. 2001. DOI 10.1103/PhysRevB.64.214422.

[90] A. Bergmann, E. Martinez-Moreno, D. Teschner, P. Chernev, M. Gliech, J. F. de Araújo, T. Reier, H. Dau, and P. Strasser, "Reversible amorphization and the catalytically active state of crystalline Co_3O_4 during oxygen evolution," *Nature Communications*, vol. 6, no. 1, p. 8625, 2015. DOI 10.1038/ncomms9625.

[91] R. D. Freeman, "Quantities, units, and symbols in physical chemistry (Mills, Ian; Cvitas, Tomislav; Homann, Klaus; Kallay, Nikola; Kuchitsu, Kozo)," *Journal of Chemical Education*, vol. 66, no. 7, p. A188, 1989. DOI 10.1021/ed066pA188.

[92] P. A. Chernavskii, G. V. Pankina, V. I. Zaikovskii, N. V. Peskov, and P. Afanasiev, "Formation of hollow spheres upon oxidation of supported cobalt nanoparticles," *The Journal of Physical Chemistry C*, vol. 112, no. 26, pp. 9573–9578, 2008. DOI 10.1021/jp077007o.

[93] R. John, M. Berritta, D. Hinzke, C. Müller, T. Santos, H. Ulrichs, P. Nieves, J. Walowski, R. Mondal, O. Chubykalo-Fesenko, J. McCord, P. M. Oppeneer, U. Nowak, and M. Münzenberg, "Magnetisation switching of FePt nanoparticle recording medium by femtosecond laser pulses," *Sci Rep*, vol. 7, no. 1, p. 4114, 2017. DOI 10.1038/s41598-017-04167-w.

[94] J. A. de Jong, I. Razdolski, A. M. Kalashnikova, R. V. Pisarev, A. M. Balbashov, A. Kirilyuk, T. Rasing, and A. V. Kimel, "Coherent control of the route of an ultrafast magnetic phase transition via low-amplitude spin precession," *Phys. Rev. Lett.*, vol. 108, p. 157601, Apr 2012. DOI 10.1103/PhysRevLett.108.157601.

[95] A. R. Khorsand, M. Savoini, A. Kirilyuk, A. V. Kimel, A. Tsukamoto, A. Itoh, and T. Rasing, "Role of magnetic circular dichroism in all-optical magnetic recording," *Phys. Rev. Lett.*, vol. 108, p. 127205, Mar 2012. DOI 10.1103/PhysRevLett.108.127205.

[96] A. F. Rodríguez, A. Kleibert, J. Bansmann, and F. Nolting, "Probing single magnetic nanoparticles by polarization-dependent soft x-ray absorption spectromicroscopy," *Journal of Physics D: Applied Physics*, vol. 43, p. 474006, nov 2010. DOI 10.1088/0022-3727/43/47/474006.

[97] M. G. Khadra, *Magnetic and structural properties of size-selected FeCo nanopartcile assemblies*. Thesis, Universitè Claude Bernard Lyon, 2015.

[98] E. D. Palik, *Handbook of Optical Constants of Solids. Chapter 14 - Optical Parameters for the Materials in HOC I and HOC II*, pp. 313–335. Boston: Academic Press, 1998. DOI 10.1016/B978-0-08-055630-7.50017-1.

[99] M. Dixon, F. E. Hoare, T. M. Holden, and D. E. Moody, "The low temperature specific heats of some pure metals (Cu, Ag, Pt, Al, Ni Fe Co)," *Proceedings of the*

Royal Society of London. Series A, Mathematical and Physical Sciences, vol. 285, no. 1403, pp. 561–580, 1965. ISSN 00804630.

[100] "AZO materials webpage." www.azom.com.

[101] C. Kittel, *Introduction to Solid State Physics, 8th Edition - Chapter 5. Phonons II. Thermal Properties.* John Wiley & Sons, 2004. ISBN 978-0-471-41526-8.

[102] M. Iwaki, "Estimation of the atomic density of amorphous carbon using ion implantation, SIMS and RBS," *Surface and Coatings Technology*, vol. 158-159, pp. 377–381, 2002. DOI 10.1016/S0257-8972(02)00247-5.

[103] C. Moelle, M. Werner, F. Szücs, D. Wittorf, M. Sellschopp, J. von Borany, H. J. Fecht, and C. Johnston, "Specific heat of single-, poly- and nanocrystalline diamond," *Diamond and Related Materials*, vol. 7, no. 2, pp. 499–503, 1998. DOI 10.1016/S0925-9635(97)00202-1.

[104] A. J. Bullen, K. E. O'Hara, D. G. Cahill, O. Monteiro, and A. v. Keudell, "Thermal conductivity of amorphous carbon thin films," *Journal of Applied Physics*, vol. 88, no. 11, pp. 6317–6320, 2000. DOI 10.1063/1.1314301.

[105] W. Zhu, G. Zheng, S. Cao, and H. He, "Thermal conductivity of amorphous SiO_2 thin film: A molecular dynamics study," *Scientific reports*, vol. 8, no. 1, pp. 10537–10537, 2018. DOI 10.1038/s41598-018-28925-6.

[106] L. Le Guyader, S. El Moussaoui, M. Buzzi, M. Savoini, A. Tsukamoto, A. Itoh, A. Kirilyuk, T. Rasing, F. Nolting, and A. V. Kimel, "Deterministic character of all-optical magnetization switching in GdFe-based ferrimagnetic alloys," *Phys. Rev. B*, vol. 93, p. 134402, Apr 2016. DOI 10.1103/PhysRevB.93.134402.

[107] B. Dieny, R. B. Goldfarb, and K.-J. Lee, *Introduction to Magnetic Random-Access Memory.* Wiley-IEEE Press, 2016. ISBN 978-1-119-00974-0.

[108] J. Wang, W. Wu, F. Zhao, and G.-m. Zhao, "Curie temperature reduction in SiO_2-coated ultrafine Fe_3O_4 nanoparticles: Quantitative agreement with a finite-size scaling law," *Applied Physics Letters*, vol. 98, no. 8, p. 083107, 2011. DOI 10.1063/1.3558918.

[109] C. M. Schneider, P. Bressler, P. Schuster, J. Kirschner, J. J. de Miguel, and R. Miranda, "Curie temperature of ultrathin films of fcc-cobalt epitaxially grown on

atomically flat Cu(100) surfaces," *Physical Review Letters*, vol. 64, no. 9, pp. 1059–1062, 1990. DOI 10.1103/PhysRevLett.64.1059.

[110] A. Stupakiewicz, K. Szerenos, D. Afanasiev, A. Kirilyuk, and A. V. Kimel, "Ultrafast nonthermal photo-magnetic recording in a transparent medium," *Nature*, vol. 542, p. 71, 2017. DOI 10.1038/nature20807.

[111] "EMSIS Asia website." www.emsisasia.com.

[112] "Pt100 chart." www.intech.co.nz.

Publications

[1] M. Franke, S. Leubner, A. Dubavik, A. George, T. Savchenko, C. Pini, P. Frank, D. Melnikau, Y. Rakovich, N. Gaponik, A. Eychmüller, and A. Richter, "Immobilization of pH-sensitive CdTe quantum dots in a poly(acrylate) hydrogel for microfluidic applications," *Nanoscale Research Letters*, vol. 12, no. 1, p. 314, 2017.

[2] N. Kavoosi, T. Savchenko, I. Senkovska, M. Maliuta, V. Bon, A. Eychmüller, and S. Kaskel, "Selective pore opening and gating of the pillared layer metal-organic framework DUT-8(Ni) upon liquid phase multi-component adsorption," *Microporous and Mesoporous Materials*, vol. 271, pp. 169 – 174, 2018.

[3] L. Baldrati, A. Ross, T. Niizeki, C. Schneider, R. Ramos, J. Cramer, O. Gomonay, M. Filianina, T. Savchenko, D. Heinze, A. Kleibert, E. Saitoh, J. Sinova, and M. Kläui, "Full angular dependence of the spin Hall and ordinary magnetoresistance in epitaxial antiferromagnetic NiO(001)/Pt thin films," *Phys. Rev. B*, vol. 98, p. 024422, Jul 2018.

[4] Z. Luo, T. P. Dao, A. Hrabec, J. Vijayakumar, A. Kleibert, M. Baumgartner, E. Kirk, J. Cui, T. Savchenko, G. Krishnaswamy, L. J. Heyderman, and P. Gambardella, "Chirally coupled nanomagnets," *Science*, vol. 363, no. 6434, pp. 1435–1439, 2019.

[5] J. Vijayakumar, D. Bracher, T. M. Savchenko, M. Horisberger, F. Nolting, and C. A. F. Vaz, "Electric field control of magnetism in si_3n_4 gated Pt/Co/Pt heterostructures," *Journal of Applied Physics*, vol. 125, no. 11, p. 114101, 2019.

[6] E. Jal, M. Makita, B. Rösner, C. David, F. Nolting, J. Raabe, T. Savchenko, A. Kleibert, F. Capotondi, E. Pedersoli, L. Raimondi, M. Manfredda, I. Nikolov, X. Liu, A. e. d. Merhe, N. Jaouen, J. Gorchon, G. Malinowski, M. Hehn, B. Vodungbo, and J. Lüning, "Single-shot time-resolved magnetic x-ray absorption at a free-electron laser," *Phys. Rev. B*, vol. 99, p. 144305, Apr 2019.

Curriculum Vitae

Personal information:

Name: Tatiana Savchenko

Date of birth: 27.10.1991

Nationality: Russian

Education:

02/2016 - 12/2019 **Doctoral studies**
Experimental Physics, Basel University, 4003 Basel, Switzerland
Microscopy and Magnetism Group, Swiss Light Source, Paul Scherrer Institute, 5232 Villigen, Switzerland
Thesis: "Manipulation of the magnetic and chemical properties of cobalt nanoparticles studied with XPEEM".

09/2008-01/2014 **Diploma**
Condensed Matter Physics, Faculty of Physics
Lomonosov Moscow State University, Moscow, Russia
Thesis: "Synthesis of magnetic nanoparticles based on metal ferrites and investigating of their heating in alternating magnetic field".